Università di Pisa

DIPARTIMENTO DI FISICA "ENRICO FERMI"

Corso di Laurea in Fisica

Tesi di laurea

Commissioning and first data analysis of the Mainz radius experiment.

Candidato:

Adriano Del Vincio

Matricola 562946

Relatore:

Prof. Francesco Forti

Prof.ssa Concettina Sfienti

Anno Accademico 2022-23

Contents

Commissioning and first data analysis of the Mainz Radius Experiment.

Adriano del Vincio

Abstract

The Mainz Radius Experiment (MREX) is an experimental campaign with the aim of determining fundamental properties of the equation of state (EOS) of nuclear matter. The equation of state contains all the thermodynamic quantities of a system of nucleons, as energy, pressure, temperature, density, and asymmetry between the number of neutrons protons in nuclear-matter. An important parameter, poorly-known at the state of current knowledge, is the slope of the symmetry energy at saturation density L, which quantifies the dependencies of the energy per nucleon associated with the changes in neutron-proton asymmetry. This key component controls how the energy of a system of nucleons change when there is a difference in the number of proton and neutrons. It is also an essential element for the determination of the radius of neutron stars, whose description is still determined by the EOS, despite being many order of magnitude higher than the physical dimensions of the nuclei. The slope of the symmetry energy L is strongly correlated to a characteristic shown by heavy nuclei, the neutron-skin thickness, that is the difference between the spacial distribution radius R of the neutrons and protons. Nowadays it is well-known, thanks to various nuclear physics experiments, that the neutrons of a nucleus tend to accumulate at a larger radius, forming a neutral thin layer around atomic nuclei. This peculiar characteristic is known in literature as neutron-skin thickness. The experimental measurement of this quantity is the main method to estimate the value of L, which is used as an input to many theoretical models of neutron stars. The MREX is focused on the determination of the neutron skin thickness of ^{208}Pb from parity-violating experiments (PV) performed at the future MESA electron accelerator, that is currently under construction and will be located in Mainz. The parity-violating experiments, where longitudinal polarized electrons scatter from a fixed target at a single value of momentum transfer, consist in the determination of the cross section asymmetry $A_{pv} = \frac{\sigma^+ - \sigma^-}{\sigma^+ + \sigma^-}$ related to the different longitudinal polarization state of the beam. The parity-violating electron scattering is a valid probe to determine the neutron-skin thickness, because it is highly sensitive to the neutron distribution due to the larger coupling of the Z^0 boson to the weak charge Q_W of neutrons, which is approximately -0.99 per neutron, while that of the proton is 0.07. In this context, it is necessary to determine one of the possible background sources for the PV experiments, known as beam normal single spin asymmetry A_n, or transverse asymmetry. The asymmetry A_n, that concerns transversely polarized electrons, comes from the interference between two Feynman diagrams whith one or two virtual photons are exchanged, giving a contribution of the order of $20\,ppm$. Because the values of A_n are typical higher that A_{pv}, the presence of a small transverse electron polarization component could produce an effect that is of the same order of magnitude of the A_{pv}. The work of this thesis focuses on the measurement of the transverse asymmetry A_n carried out at the Mainz microtron accelerator (MAMI) on a ^{12}C target. The ^{12}C target is particularly suited for studying and testing the electronics systems and detectors that will be employed in the next phase of the MREX experiment, the determination of A_n for ^{208}Pb. The measurement consists in the determination of A_n using two Cherenkov detectors made of fused-silica materials coupled to 3 and 8 photo-multiplier tubes. The two detectors have been tested in the laboratory, together with the new electronics for the data read-out, that consist in the NINO-asic board with which the impulse signals coming from the detectors are acquired. The beam parameters, as the transverse position of the beam, the scattering angles, and the current intensity and energy are determined with particular accuracy because their variation over time can result in effects that overlap with A_n. This required the development of a new analysis program, processing the raw data to extract the beam parameters relevant for the analysis, and separating the contributions of the false asymmetries from A_n. The work consisted in a first part dedicated to the calibration of the monitors, to measure the parameters of the beam. The second part was focused on the analysis of the data collected during the beam time, removing the outliers, identifying possible errors and isolating the contribution of false asymmetries. A_n has been measured for electron-carbon scattering at a two fixed angles ($\theta_B = -22.5°$, $\theta_A = 22.5°$) corresponding to a transfer momentum of $Q^2 = 0{,}04\,\mathrm{GeV}^2$. The measured values are: $A_B = -21 \pm 5\,(stat)\,ppm$ for detector B and $23.1 \pm 1.7\,(stat)\,ppm$ for detector A. The different sign of the two measurements is in agreement with the opposite kinematic, and the two measurements are compatible within $1\,\sigma$, and in agreement with the previous measurements performed at MAMI. The results obtained confirm the capabilities of the electronic systems and components used during the experiments and are encouraging in anticipation of the next measurement of the transverse asymmetry for lead.

Organization of Contents

This thesis can be dived in two part: the first part is dedicated to the description and motivations regarding the MREX experiment and the description of the MAMI accelerator, where much of the work was done. The second part is focused on the analysis of the data acquired during the beam time. A list of the chapters with a brief explanation of the contents follows:

- **chapter 1**: In this chapter the physics and motivation of the MREX experiment are presented. The Equation of state for nuclear matter is described, with particular attention on the symmetry energy S. Following we discuss the relevance of this parameter in many fields of physics, from Neutron stars to nuclear physics, and the experimental effort to measure this quantity from the determination of the Neutron skin thickness of ^{208}Pb
- **chapter 3** Description of MAMI experimental setup and beam characteristics. Explanation of beam measurement equipment and the interface with the electronics developed for the MREX experiment.

The result obtained are discussed and compared with the other measurements performed by different collaborations. Finally the confront with the theoretical prediction discussed in chapter 2 is done.

Chapter 1

Physics Motivation for Neutron Skin Thickness Measurement

1.1 The Mainz Radius Experiment

The Mainz Radius Experiment (MREX), at the Mainz nuclear physics institute, is an experimental campaign with the aim of investigating the complex nature of atomic nuclei. The strong force, whose presence was first speculated by Yukawa in 1935, is responsible of a broad range of phenomena: from characteristic of atomic nuclei, the compositions of baryons and meson to the exotic structure of Neutron stars. So, the field of nuclear physics provides many answers to fundamental questions in other fields of physics. In particular the neutron stars, that are one of most interesting astrophysical object in the universe, are ideal to study and test theories of dense matter, providing so many connection between particle physics, astrophysics and nuclear physics. It can be surprising to think that, despite a difference of so many order of magnitude, neutron rich nuclei and neutron stars have the same basic physics, enshrined by the the Equation Of State (EOS) of neutron rich matter. The Equation Of State represents the fundamental relation between the state variables as temperature, energy, pressure and neutron-proton asymmetry. Specifically, the final goal of the MREX experiment is to determine an important parameter of the EOS, that is the slope of the symmetry energy at saturation density L. This parameters is important for the determination of the radius of the neutron stars, but it is also responsible of a peculiar characteristic shown by heavy nuclei: the neutron skin thickness δr_{np}. The neutron skin thickness is a phenomena that affect heavy nuclei which consists in the accumulation of the excess of neutrons near the surface of a nucleus. Such skin thickness is strongly sensitive to L, so an accurate determination of the neutron skin provides significant constrains on the value of L which in turn is used as an input to many theoretical models of the structure of the neutrons stars. The determination of δr_{np} presents considerable difficulties. While r_p is known with high accuracy, thanks to the electrons elastic scattering experiment which involves electromagnetic force, the determination of r_n has traditionally relied on hadronic experiments which involves proton-nucleus scattering, π^0 photo-production, α and π nucleus scattering. Those process suffer from large and often uncontrolled theoretical uncertainties that compromises the extraction of the neutron density. The most promising method, that is the least model dependent, is the parity-violating electron scattering. In this reaction longitudinal polarized electrons are elastically scattered off unpolarized target. This method consist in the measurement of the asymmetry between right and left handed electrons:

$$A_{pv} = \frac{\sigma_R - \sigma_L}{\sigma_R + \sigma_L} \tag{1.1}$$

This process is dominated by the exchange of a virtual photon, which is sensitive to charge form factor, and a Z_0 boson, that is sensitive to the weak form factor. Because of the fact that the weak charge of the neutrons is $Q_w = 0.99$ and the weak charge of the proton is 0.04, the weak form factor contains the information on the neutron density, necessary to measure δr_{np}. In this context, the MREX experiment is an experimental campaign with the aim of measuring the neutron skin thickness via the parity violating scattering at the new MESA electron accelerator, at the Nuclear physics institute of Mainz .

1.2 Nuclear Equation of State (EOS) and Neutron Skin Thickness

During the 30s of the last century, a considerable part of the scientific community was concentrated in the study of the structure of atomic nuclei. The discovery that every atoms has a positive charged nucleus dates back to 1908, with the famous Rutherford experiment, where alpha particles scatter from a thin gold foil. In the following years, especially with the birth of quantum mechanics in the second half of the 1920s, significant progress were made in the knowledge of atomic nuclei and their properties. In 1935, a significant contribution was given by Carl Friedrich von Weizsäcker and Hans Bethe, that proposed the semi-empirical mass formula, to approximate the mass of an atomic nucleus [5]. Although some refinements have been made over the years, the general structure of the formula is the same today. The model proposed by Weizsäcker is the application of the liquid-drop model for nuclear matter, where the Nucleus is described as drop of protons and neutrons, that are assumed to be incompressible and are held together by a nuclear potential. The semi-empirical mass formula states that the mass of a nucleus is given by

$$m = Zm_p + Nm_n - \frac{E_B(N,Z)}{c^2} \tag{1.2}$$

An important terms is the binding energy E_B, that contains 5 parameters:

$$E_B = a_V A - a_s A^{\frac{2}{3}} - a_c \frac{Z^2}{A^{\frac{1}{3}}} - a_{asym} \frac{(N-Z)^2}{A} + \delta(N,Z) \tag{1.3}$$

The first two terms a_V, a_s are taken from the liquid drop model, and are the volume energy and the surface energy. The volume term represent the energy due to the interaction of each nucleon with the other nearby nucleons. This term is proportional to A, that is the number of nucleon of the nucleus, which is proportional to the volume, hence the name. The second term represent is the surface energy, and it is a correction to the volume energy. The volume energy assume that each nucleon interact with a constant number of nearby nucleons, but this is not true if we consider the external protons and neutrons, because they have less neighbors to interact with. This correction terms is then proportional to $A^{\frac{2}{3}}$, that is the also proportional to the surface area. The third term a_c denote the binding energy correction due to the repulsion between protons. The fourth term is a_{asym}, the asymmetry term, and it is proportional to the asymmetry between neutrons and protons. The theoretical justification for this terms is due to the Pauli exclusion principle. Neutrons and protons are distinct type of particles, and occupy different quantum states. Because neutrons/protons are fermions, they can't occupy a state with the same quantum numbers, therefore higher energy states are progressively filled. If there is an asymmetry between neutrons and protons, for example the number of neutrons is greater than the number of protons, some neutrons will be in higher energy states respect to the protons. The imbalance between the nucleons causes the energy to be higher respect to the situation with the same number of protons and neutrons. The last term the pairing term, and describes the effect of spin coupling, and has positive/negative values for even or odd N,Z. We want to focus on the fact that the liquid-drop model has the underlying assumption that the nucleons are incompressible. Because of this it is well defined the concept of saturation density, the fact that the density, at first order, is almost constant and independent of mass number A. In the context of neutron stars, it is more useful to take the thermodynamic limit in which the number of nucleons and Volume are taken to infinity. The binding energy per nucleons can be written as:

$$\epsilon(\rho_0, \alpha) = -\frac{E_B}{A} = -a_V + a_{asym} \frac{\rho_n - \rho_p}{\rho_n + \rho_p} \tag{1.4}$$

In reality, this simple equation is only an approximation, because the nuclear matter doesn't behave like an ideal liquid drop, and it is not incompressible. To describe the response of the nuclear matter to density variation, as well as temperature, etc... we need the equation of state (EOS) of the system, that binds these quantities thermodynamically. For neutron stars, the EOS depends on ρ, the conserved baryon density, and neutron-proton asymmetry α, in the ideal limit of $T = 0$:

$$\epsilon(\rho, \alpha) = \epsilon_{snm}(\rho, \alpha = 0) + \alpha^2 S(\rho) + O(\alpha^4) \tag{1.5}$$

The energy density is expanded in a power series of $\alpha = \dfrac{\rho_n - \rho_p}{\rho_n + \rho_p}$. No odd power of α appears in the expansion, because the strong force doesn't depend on the isospin, or in other words, neglecting electromagnetic interaction and weak interaction, the equation of state depends only on the relative asymmetry between neutrons and protons, it doesn't matter if such an asymmetry is biased towards protons or neutrons. The terms $S(\rho)$ is the symmetry energy, and it represents the cost of converting symmetry nuclear matter ($\alpha = 0$) to pure neutrons matter, as the case of neutron star. Now we can proceed considering the saturation density. A further expansion around the saturation density ρ is necessary [15]:

$$\begin{aligned} S(\rho) &= J + L \cdot \frac{\rho - \rho_0}{3\rho_0} + \frac{1}{2} K_{sym} \cdot \left(\frac{\rho - \rho_0}{3\rho_0} \right)^2 \\ \epsilon_{smn}(\rho) &= \epsilon_0 + \frac{1}{2} K_0 \left(\frac{\rho - \rho_0}{3\rho_0} \right)^2 \end{aligned} \tag{1.6}$$

Several new terms appear in this expression:

- ϵ_0 is the energy per nucleon for symmetric matter at saturation density.
- J is the symmetry energy at saturation density.
- L is the slope of the symmetry energy.
- K_0 is the incompressibility coefficient for symmetry matter.
- K_{sym} is the incompressibility coefficient for the symmetry energy.

In this expression appears for the first time L, the slope of the symmetry energy. This is a key component of the EOS, whose values is an important parameter to determine the radius of neutron star. L quantifies the difference between the symmetry energy at saturation (as in the nuclear core) and the symmetry energy at lower densities, as in the nuclear surface.L is also related to the pressure P at saturation density. Giving the EOS in term of ρ, α, the pressure is given by:

$$P = \rho^2 \frac{\partial \epsilon(\rho, \alpha)}{\partial \rho} \tag{1.7}$$

A formal demonstration of this relation is given in the appendix (). We know write ϵ_{snm} making explicit all the dependencies:

$$\epsilon(\rho, \alpha) = (\epsilon_0 + \alpha^2 J) + \alpha^2 L x + \frac{1}{2}(K_0 + \alpha^2 K_{sym}) x^2 \tag{1.8}$$

we substitute $x = \dfrac{\rho - \rho_0}{3\rho_0}$. Considering pure neutron matter $\alpha = 1$, the pressure at saturation density P_0 can be easily computed withe the formula (1.7). The result is the following:

$$P_0 \simeq \frac{1}{3} \rho_0 L \tag{1.9}$$

From this expression we learn that the slope of the symmetry energy is essential to determine the pressure for densities near saturation. The contribution of the symmetric term $\epsilon_{snm}(\rho)$ vanishes, and at first order the pressure depends only on L. Because of this, it becomes more and more clear the link between L and the neutron skin thickness. Let's consider the case of the ^{208}Pb, with ad excess of 44 neutrons. Placing the excess of neutrons in the surface of the nucleus is discouraged by surface term a_S, which tends to minimize the area. However, if the excess of neutrons is placed in the core of the nucleus, this is increase the symmetry energy $S(\rho)$. In the end the neutron skin is the result of the competitions between the surface tension and the slope of the symmetry energy. Measurement of the neutron skin have been performed by the PREX collaboration at Thomas Jefferson National Accelerator Facility in Virginia [3], however the precision attained was insufficient to distinguish between the various competing models which describe the relation between δr_{np} and L (1.1). Despite this, theoretical predictions states that there is a strong correlation between these two quantities, in the following plot we show how different theoretical models, with different values of L used as input, predict the values of δr_{np} for lead:

A strong linear correlation is evident, and so it is clear that measuring the neutron skin is a promising way to measure L.

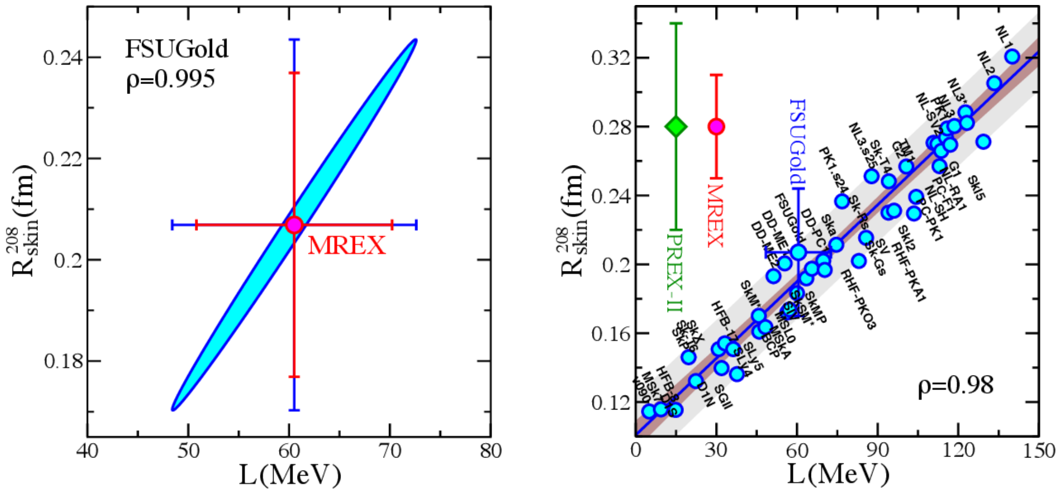

Figure 1.1: *On the right* Neutron skin thickness of ^{208}Pb as a function of the slope of the symmetry energy L. The error bars represent ±0,06 fm and ±0,03 fm for the future experiments of PREX-II and MREX. Notice the different scale for x and y axis, a small uncertainty for the neutron skin measurement correspond to an higher uncertainty for the values of L. *On the left* Covariance ellipse displaying the correlation between L and the neutron skin thickness, for FSUGold model. The covariance ρ is equal to 0.995.

1.3 Parity-violating Scattering Experiment

The parity violating electron scattering seems to be the most promising method in order to determine the neutron-skin thickness for ^{208}Pb. The choice of lead is due to the significant neutron excess and stability of lead nuclei (^{208}Pb is a double magic nucleus). The advantage of this method is that it is free from the many uncertainties associated to strong interaction. The main disadvantage is the necessity to accumulate large statistics, because the reaction are mediated by the weak interaction, that produce a smaller amplitude compared to electromagnetic and strong interaction. The parity violating scattering is high sensitive to the neutron density because, as mention above, the weak charge of the neutron is higher compared to the weak charge of the proton. In this reaction, longitudinally polarized electrons are elastically scattered off a lead target. The important quantity to determine is the parity violating asymmetry A_{PV}, the difference in cross section between the scattering of right and left handed electrons.

$$A_{PV} = \frac{\sigma_R - \sigma_L}{\sigma_R + \sigma_L} \tag{1.10}$$

The theoretical calculation of A_{PV} concern the interference between the exchange of virtual γ and Z^0. In the Born approximation A_{PV} is directly proportional to the weak form factor, and it is given by the formula below:

$$A_{PV} \simeq \frac{G_F Q^2}{4\pi\alpha} \cdot \frac{Q_W F_W(Q^2)}{Z F_{ch}(Q^2)} \tag{1.11}$$

G_F is the Fermi constant, Q^2 is the transferred momentum, Z and Q_W is the electric and weak charge of the nucleus. The Charged form factor of the lead nucleus is known with high accuracy (precision of 0.02 %), so in this limit the only quantity that is unknown is $F_W(Q^2)$. In the long wavelength approximation, the weak form factor at single value of momentum transfer is given by:

$$F_W(Q^2) = \frac{1}{Q_W} \int \rho_W(r) \frac{sin(Qr)}{Qr} d^3r = (1 - \frac{Q^2}{6} R_W^2 + \frac{Q^4}{120} R_W^4 + ...) \tag{1.12}$$

The form factor is normalized in such a way that $F_W(Q^2 = 0) = 1$. The weak charge radius correspond to $R_W^2 = -6 \frac{\partial F_W}{\partial Q^2}\Big|_{Q^2=0}$. Now it is clear that parity-violating experiment are a promising method to extract information about neutron density. The effort is represented by the small values of A_{pv} asymmetry. Typical values are on the order of 1 ppm or less, for lead target. This requires high statistic to reduce the uncertainty of the measurement. In 2012 PREX collaboration measured for the first time through parity-violating experiment the neutron skin, the values is:

$$\delta r_{np} = 0.33^{+0.16}_{-0.18}\text{fm}$$

The error associated to this first measurement is not enough small to provide significant constraints on the values of L. Because of this, the MREX experiment has the objective of measuring the neutron radius of lead with a precision of 0.5% ($\pm$0,03 fm). This high precision is needed to decrease the uncertainty associated to L. For example, the left plot in 1.1, shows the correlation between the neutron skin thickness of ^{208}Pb and the slope of the symmetry energy as predicted by FSUGold model ([9]). With a precision of $\pm$0,03 fm, L is determined with $\pm$12,1 MeV. A new recent measurement, in 2019, measure the neutron skin thickness with a precision of $\delta r_{np} = 0.283 \pm 0.071$fm. With new measurement that will be performed in MESA accelerator by MREX, the precision will be improved further by a factor 2.

1.3.1 Neutron Star Radius

We mentioned that the slope of the symmetry energy L is strongly correlated to the neutron skin thickness of ^{208}Pb and also to the neutron star radius. We can go deeper in the discussion stating that the maximum neutron-star mass and radius are uniquely constrained by the E0S. The maximum mass depends on the energy density dependence of the Pressure, that must be high enough to oppose the gravitational collapse into a black hole. Moreover, stellar radii are strongly dominated by the pressure of degenerate neutron-star matter near the nuclear saturation density which is, in large part, determined by the symmetry energy of the EOS. A formal proof is shown in [14]. Theoretical models [17] demonstrate this connection between L and R_{ns}, for this purpose we show here the covariance ellipses displaying the correlation between the slope of the symmetry energy and L and the stellar radii:

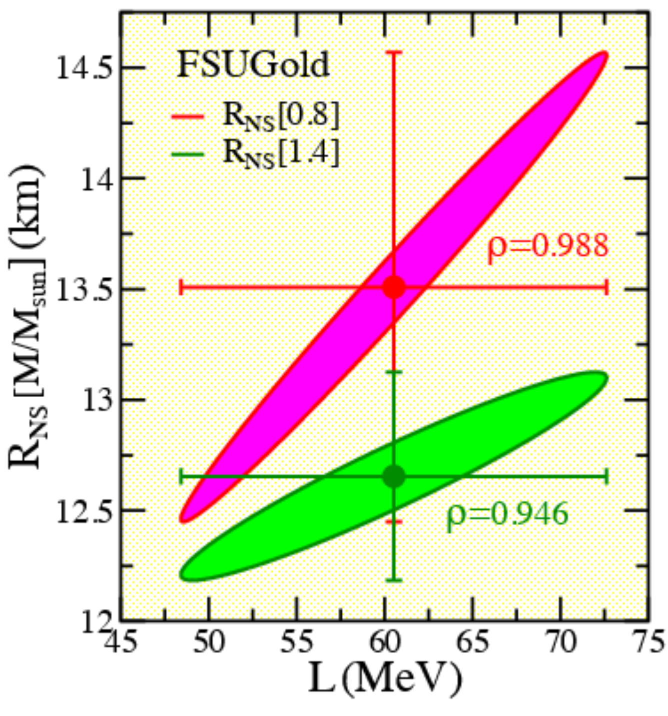

Figure 1.2: Covariance ellipses between slope of the symmetry energy and stellar radii, for 0.8 and 1.4 solar masses of neutron star. predicted by the relativistic density model FSUGold.

Because of this, astronomical observation of Mass and radii represents important constrain on the EOS parameters. Astronomical observations of the neutron star radius rely traditionally on photometric measurements, assuming that thermal emission of light from the surface follow a blackbody spectrum at uniform temperature. These measurement are affected by systematic uncertainties that are typically of a couple of kilometers. However, the situation is rapidly changed with the beginning of the gravitational wave detection. The first observation of the binary neutron star merger by the LIGO-Virgo collaboration opened a new path to measure the neutron-stars radius [2]. In fact, the gravitational wave generated by the merging of two neutron stars depends on a property called tidal deformability; this parameters described the tendency of neutron star to deform in response of the gravitational field of its companion star. This parameters Λ, is highly sensitive to the ratio of the stellar radius to the Schwarzschild radius:

$$\Lambda = \frac{2}{3} k_2 \left(\frac{c^2 R_{NS}}{GM} \right) \tag{1.13}$$

In this expression, M and R_{NS} are the neutron star mass and radius, and k_2 is the second tidal Love number [6], which is computed from the quadrupole component of the gravitational field induced by the companion. From the first detection, an upper limit of $R_{NS}^{1,4} < 13{,}76\,\mathrm{km}$ was placed on the radius of a neutron star with a 1.4 solar masses. Because of the strong correlation between R_{NS}, L and δr_{np}, this is a indirect constrain on the neutron skin thickness of ^{208}Pb. An upper limit of $\delta r_{np} < 0{,}25\,\mathrm{fm}$ was obtained. This limits is not consistent with the larger values measured by PREX collaboration; this can suggest that the symmetry energy, for slightly higher density as in neutron stars, decreases, respect the typical density found in atomic nuclei. This increment and decrement may be a proof of the presence of phase transition in the interior of neutron stars.

1.4 Transverse Asymmetry

The parity-violating scattering has numerous advantages for extracting the neutron-skin thickness of nuclei. However, the asymmetry to measure is rather small. The important effort is to reduce at most possible systematic effects that can alter the result of the measurement. One of the principal source of background for the measurement of A_{PV} is a different process that concerns transverse polarized electrons. The different polarization of the electrons produce an asymmetry that is called beam normal single spin asymmetry, or transverse asymmetry A_n. Because such asymmetries are typically one order higher that the parity-violating ones, a small normal component of the beam polarization during parity-violating experiment can produce a systematic effect that alter the final result. The subject of this thesis is the measurement of transverse asymmetry A_n for carbon target, performed at MAMI, the Mainz microton accelerator. The choice of carbon target is due to the fact that the transverse asymmetry for carbon is well known and already measured at MAMI; the expected asymmetry is roughly $20\,ppm$, thus it is particularly suited for a commissioning of the new experimental setup. In this section don't introduce physics of this process, that will be extensively treated in the next chapter. However, we mention that such measurement are challenging because they require calculation of box diagrams with intermediate excited states [11]. After the determination on A_n for ^{12}C, the next step of the MREX experiment will be the determination of the transverse asymmetryfor ^{208}Pb. As already mentioned, this is mandatory to constrain the systematic effects of PV experiment. However, it is also interesting because for last measurement performed by PREX [4] the transverse asymmetryfor ^{208}Pb target is compatible with zero, and this is in striking disagreement with the theoretical predictions.

Chapter 2

Transverse Asymmetry

This chapter is focused on describing the theory behind the transverse asymmetry. The transverse asymmetryarises from interference between two scattering amplitudes and it is deeply connected with the Time-reversal operator. These two contributions due to the electromagnetic interaction between the incident electron and the nucleus are explained by showing what are the limits of current theory and what are the most important terms in theoretical prediction. The chapter ends by presenting the problem of the anomalous observation made by PREX of zero transverse asymmetry and a study on the accuracy with which it is possible to measure the asymmetry.

2.1 Description of the Process

The Beam Normal single spin asymmetry, which we will refer for brevity as Transverse asymmetry, originates from the interference of two scattering process. The theory of the electron scattering against a spin 0 target is extensively treated in [11]. To understand why the interference of this two scattering amplitude give rise to an asymmetry, we first have to look at the kinematic of the experiment:

Where all the momenta are measured respect to the center of mass frame. In the figure we can confront the two situation before and after applying the Time-reversal operator, $\hat{\Theta}$. Looking at the picture we can understand that :

- Before applying $\hat{\Theta}$, we have the incident electron with $\vec{k}$ momenta and the nucleus with $\vec{P}$ momenta, after applying $\hat{\Theta}$ we have that the incident/outgoing electron and the incident/outgoing nucleus are exchanged.
- The $\hat{\Theta}$ operator acts also on the spin of the electron. Because we are considering process where the spin doesn't flip, the two situations are not equivalent.
- Considering that the process is elastic, the kinematic is the same, taking $\vec{p}$ and $\vec{k}$ as the initial particle momenta, or $\vec{p}'$ and $\vec{k}'$.

The time-reversal operator seems to connect the two different cases of UP and DOWN polarized electron. Our effort is to measure the asymmetry between the two cross section:

$$A = \frac{\sigma_\uparrow - \sigma_\downarrow}{\sigma_\uparrow + \sigma_\downarrow} \tag{2.1}$$

And it's particularly clear that a non-zero asymmetry depends on how the time-reversal act on the elastic amplitude of the process.
With this idea, let's see in more detail the $\hat{\Theta}$. We know that $\hat{\Theta}$ is an anti-unitary operator that can be always seen as:

$$\hat{\Theta} = U \cdot K$$

Where U is an unitary operator, while K is the complex conjugation operator that generates the complex conjugate of each coefficient in front of it. If we consider a ket describing a system we have that:

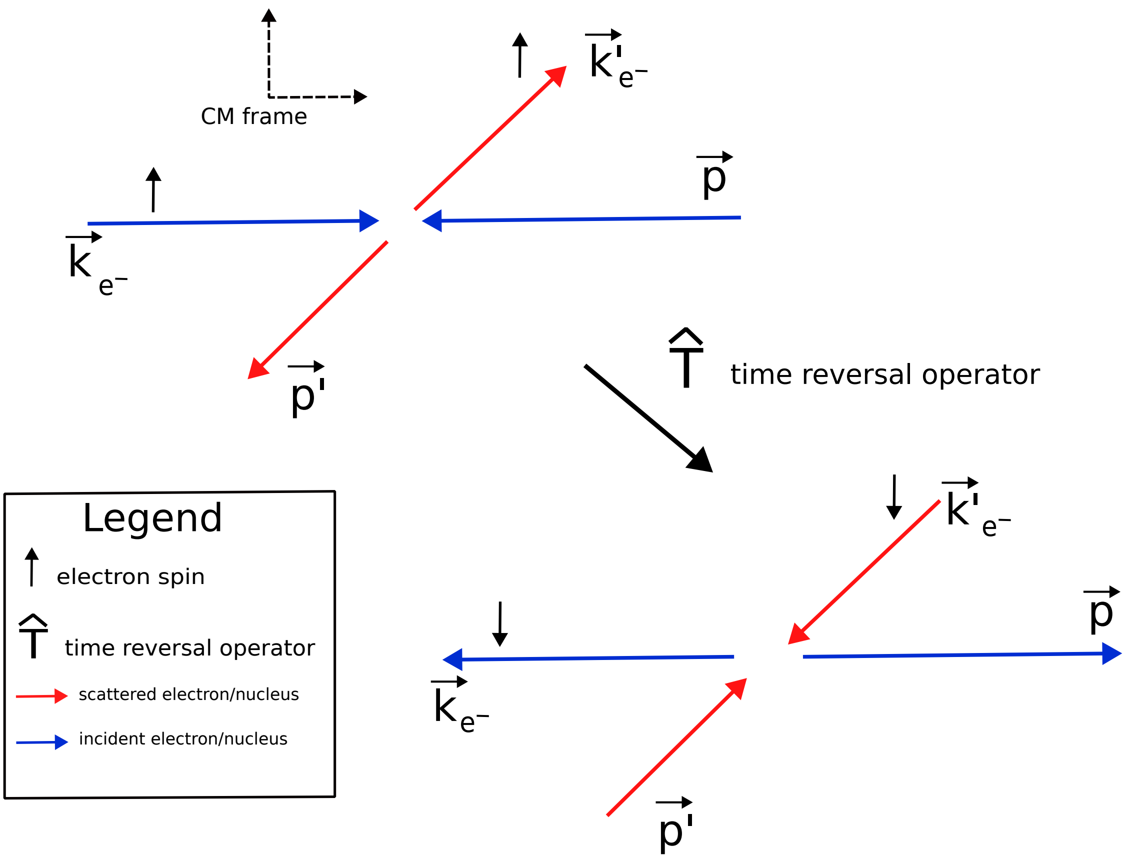

Figure 2.1: Scheme of the scattering process. In blue the incident electron and nucleus, in red the outgoing electron and nucleus. All the quantities are referred to the center of mass frame. The small arrow over the vector represent the electron spin, aligned in the normal plane.

$$Kc\,|\alpha\rangle = c^{*}K\,|\alpha\rangle \tag{2.2}$$

Now, let's consider H as the hamiltonian of our system. We want to apply the $\hat{\Theta}$ operator. We can now use the assumption that the hamiltonian consist of two term, which correspond to the two different scattering process. Because of the electromagnetic interaction conserve CP, so also T is conserved, we know in advance that each piece of the hamiltonian commute with $\hat{\Theta}$. Now let's see what happen for an hamiltonian which has an imaginary part:

$$H = H_R + iH_{Im} \quad ; \quad \hat{\Theta}H\hat{\Theta}^{-1} = \hat{\Theta}H_R\hat{\Theta}^{-1} + \hat{\Theta}iH_{Im}\hat{\Theta}^{-1} \Rightarrow H_R - iH_{Im} \neq H \tag{2.3}$$

what we understand from these simple calculation is that to give rise to an asymmetry, we expect an imaginary part of the scattering amplitude different from zero.
At the α leading order, the two process of the electron-Nucleus scattering that give rise to the asymmetry involve the exchange of one-photon-exchange (OPE) and two-photon-exchange (TPE). The Feynman diagrams that describes the processes are the following:

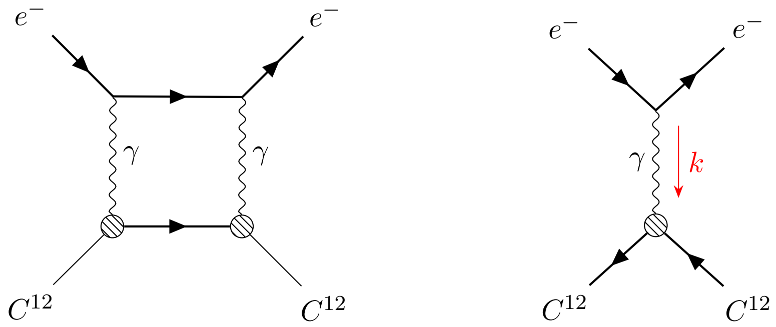

Figure 2.2: TPE and OPE diagrams in electron nucleus scattering.

The important quantity to compute the cross section is the scattering amplitude. The scattering amplitude is given by the two contributions: the exchange of a single virtual photon A_1 and the terms given by the two photon exchange A_2. In general we can write that the total scattering amplitude S:

$$S = \frac{e^2}{Q^2}\overline{u}(k')[\,m_e A_2 + A_1 \not{P}\,]\overline{u}(k) \tag{2.4}$$

Where in this expression $\vec{P} = \frac{\vec{p}+\vec{p}'}{2}$. The second term A_1 has a simple expression, given by the form factor of the nucleus:

$$A_1 = 2ZF_N(Q^2)$$

This expression is obtained if we look at the 2.2. For the one photon exchange the first vertex connects the incident and scattered electron, whose expression is given by $-ie\gamma^{\mu}$. The second vertex connect the carbon nucleus with the virtual photon. The carbon is threated like as a spin 0 particle, and the contribution due to the charge density in enshrined in the form factor. The lagrangian term for a vertex of this type is given by the formula:

$$\mathcal{L}_{interaction} = +ieA_{\mu}(\Phi\partial^{\mu}\Phi^{\dagger} - \Phi^{\dagger}\partial_{\mu}\Phi) \tag{2.5}$$

For the spin 0 field Φ. This is not the only piece of the lagrangian: there exist another term of interaction, that involves a vertex with four particles which is not of our interest. This interaction term give rise to the Feynmann rule for spin 0 particle, and we have to substitute for this vertex:

$$-ie(p+p')_{\mu}$$

And we recognize, apart from a factor 2, $\not{P}$ which multiplies A_1. The last term is the feynmann propagator for the photon, that give the $\frac{1}{Q^2}$ term. This first part of the scattering amplitude is T-even, and it is purely real, so it is the imaginary part of the two photon exchange which give rise to the asymmetry. The expression that connects the amplitude with the transverse asymmetryis given by:

$$A_n = -\frac{m_e}{\sqrt{s}} tan(\frac{\theta_{CM}}{2}) \frac{\mathrm{Im}(A_2)}{ZF_N(Q^2)} \tag{2.6}$$

Looking at this formula, the theoretical effort to compute the transverse asymmetry is given by the imaginary part of A_2. The calculation of this quantity is theoretically challenging, due to the fact that at energies of $\simeq 1\,\mathrm{GeV}$ of incident electrons, contributions from intermediate excited states become important. Because of this, the contribution of A_2 are given by the sum of elastic intermediate state and inelastic terms, which involve hadronic excitations.

2.1.1 Hadronic Tensor

The imaginary part A_2 is related to the two-photon exchange. To compute this quantity, we have to perform an integration over the internal momenta of the electron k_1 (see figure 2.2). This contribution, following [11], is given by:

$$\mathrm{Im}(A_2) = e^4 \frac{1}{(2\pi)^2} \int \frac{l_{\mu\nu} \cdot W^{\mu\nu}}{2E_1 Q_1^2 Q_2^2} d^3\vec{k_1} \tag{2.7}$$

Two new terms appear in this expression. The first term is $l_{\mu\nu}$, named leptonic tensor. This term is given computing the Amplitude for the upper part of the diagram, which involve the incident and scattered electron:

$$l_{\mu\nu} = \overline{u}(k')\gamma_\nu(\not{k}_1 + m_e)\gamma_\mu u(k) \tag{2.8}$$

In this expression is immediate to recognize the feynmann rules for fermion vertex. The term $(k_1 \not+ m_e)$ comes from the fermion propagator of the internal electron, which is:

$$\frac{i(\not{p} + m)}{p^2 + m^2}$$

The other term is $W^{\mu\nu}$, the hadronic tensor. For the elastic contribution this term is simply given by the feynmann rules for vertex with spin 0 particles, with the proper correction of the form factor, so we can write:

$$W_{\mu\nu} = \pi\delta((p + k - k_1)^2 - M^2)(2p + q_1)_\mu(2p' + q_2)_\nu \times Z^2 F_N(Q_1)F_N(Q_2) \tag{2.9}$$

At this point, one can substitute in the integral above, and compute the contribution of the transverse asymmetry due to the elastic term. This first terms scales with the nuclear charge $Z\alpha$, and this is important for electron scattering with heavy nuclei. However, this mechanism is important in the energy range of few MeV, and has a minor impact, although not negligible, for higher energy, such as the energy of interest for this thesis. For the inelastic contributions, the structure of the hadronic tensor is different. Realistic estimate are given only for nearly forward scattering angles. The hadronic tensor is given in terms of the structure functions $W_{1,2}$

$$W^{\mu\nu} = 2\pi W_1(\omega^2, Q_1^2)\Big(-g^{\mu\nu} + \frac{P^\mu q_1^\nu + P^\nu q_2^\mu}{(P\overline{K})} - \frac{q_1 q_2}{(P\overline{K})^2} P^\mu P^\nu\Big) \tag{2.10}$$

Several assumption are made to threat this new term. The structure function, for forward scattering angles, can be approximated by a function containing the Compton form factor of the nucleus, neglecting some dependence on $Q_{1,2}$ that let to simplify the integral in equation 2.6. It is beyond our scope to go into a detailed description, which can be found in the articles ([12], [11], [13]). We emphasize however that for the estimation of the inelastic intermediate state, theoretical calculation are affected by the approximation of forward angles and other assumptions due to lack of data in the dependence of some important variables, such as the Compton form factor for carbon 12, the Compton slope parameter and the use of the approximated Callavan-Gross relation. In summary, the theoretical prediction for the transverse asymmetryare reliable for small scattering angle, that correspond to lower values of the transfer momentum Q; the experimental data measure by PREX [4] for ^1H, ^4He, and ^{12}C at Q values of 0,31 GeV, 0,28 GeV and 0,1 GeV, respectively, are in agreement with the theoretical prediction. The last measurement performed at MAMI for ^{12}C [8] for higher values of transfer momentum, shows a discrete agreement with the theoretical prediction, considering also the systematic uncertainties associated to the poorly known Compton slope parameter.

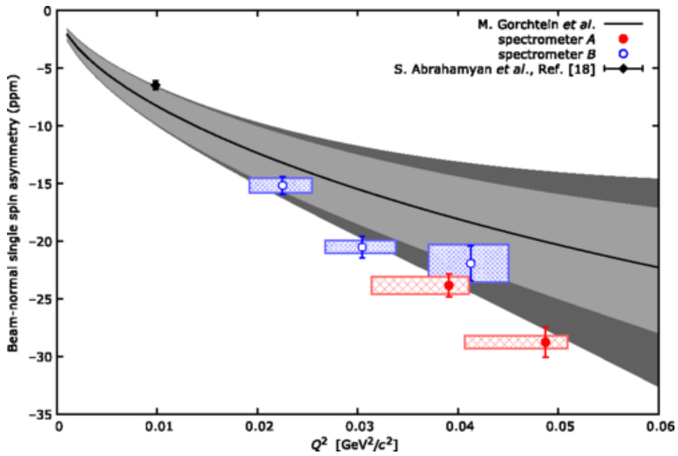

Figure 2.3: Transverse asymmetry measured at MAMI for ^{12}C target [8]. Theoretical calculation for E_{beam} = 570 MeV is shown.

2.1.2 Model Description

$$A_N = C_0 \cdot log(\frac{Q^2}{m_e^2 c^2})\frac{F_{Compton}(Q^2)}{F_{ch}(Q^2)} \tag{2.11}$$

2.2 State of the Experiment

We have seen so far how the Transverse Asymmetry is related to the interference between two scattering amplitude, and the theoretical model used to describe the process. The goal from an experimental point of view is to measure this quantity. The challenge is to obtain a valid measure of A_n, which is of the order of 20 part per million (ppm), taking into consideration all the possible effects that can interfere. To measure A_n, the straightforward method is to prepare an electron beam, with polarized electron, and send it to a fixed target. The scattered electrons are then collected by a detector placed at a certain angle, and now it's possible to obtain the transverse asymmetry applying the formula:

$$A_N(Q,p) = \frac{N_\uparrow(Q) - N_\downarrow(Q)}{N_\uparrow(Q) + N_\downarrow(Q)} \cdot (\frac{1}{p}) \tag{2.12}$$

where we have explained the dependence on the transmitted impulse, on the degree of polarization of the beam. In an experiment of this type, several requests are necessary to have an effective data acquisition:

- The accelerator must produce a polarized beam, stable over the time, with an high polarization percentage, in order to amplify the effect.
- The Beam energy needs to be quite stable, and should not depend on the Polarization state of the electrons. A change in the Beam energy associated with the polarization state, can lead to a different count rate for $N_\uparrow$ and $N_\downarrow$, would make a contribution that would be added to that of the physical process
- The beam must be correctly aligned with the target, and stable. Again if the position of the target changes according to the polarization of the electrons, it will produce another contribution to the total asymmetry.
- The beam current should not depend on the polarization state of the electrons. If the beam source depends on the polarization, we will have a difference in the event rate and then another false asymmetry.

- it's necessary to reject possible double elastic scattering events, which may contribute to the total asymmetry.

All this demands can be satisfied with an accelerator that has stabilization devices with great precision and that can sustain high beam intensities. This last request is necessary to accumulate enough statistics to measure the transverse asymmetry with an accuracy about 1 ppm, in view of the future PV experiments. We can quantify how the statistical error varies according to the amount of data available. With the quite general assumption that the measured rate $N_{\uparrow,\downarrow}$ are gaussian distributed variables, we can compute the expected variance of A_n:

$$Var[A_n] = \frac{1 - A^2}{N_\uparrow + N_\downarrow} \tag{2.13}$$

This is the variance associated to a single measurement of the transverse asymmetry. As is well known, the variance scales as $\frac{1}{n}$ as n, the number of measures, increases. Because the A_n is expected to be quite small, we can approximate the above formula:

$$V[A_n] = \frac{1}{2N \cdot n} \tag{2.14}$$

The error associated to the reconstructed asymmetry is the square root of the above quantity. If we impose that the error must be $\leq 1ppm$ we can easily obtain that the quantity $n \cdot N$:

$$n \cdot N \leq \frac{1}{2} \cdot 10^{12}$$

We will see later that achievable rates $N_{\uparrow,\downarrow}$ are in the range (20000,60000) counts per event for a carbon target. This number can not be increased at will by acting on the beam current. The first reason is oblivious: the beam source can produce only a certain amount of electrons before loosing, furthermore a beam with great intensity for an extended periods of time can damage the carbon target up to the risk of melting it. Another idea might be to increase the thickness of the target, to take advantage of the larger cross section. However this does not take into account that by doing so the number of double scattering event is increased. To avoid this the scientific community that deals with these nuclear physics measurements respect the convention that the target thickness should be less than the 10% of the radiation length of the material.

Chapter 3

Experimental setup

This chapter presents briefly the structure and the characteristics of the Mainz microtron accelerator (MAMI), where the transverse asymmetryasymmetry is measured, and the experimental setup used. Particular attention is shown in the the description of the beam monitors, that are quite specific for the standard of particle accelerators. Following an overview of MAMI and the acceleration stages, the experimental hall and the specific electronics devices to acquire and process the data are presented.

3.1 Overview of the Experiment

To measure the Beam-Normal single spin asymmetry, a polarized beam of 570 MeV will be sent against a 10 mm width of ^{12}C target. The detectors consist of two fused-silica coupled to 3 (detector B) and 8 (detector A) pmts, which collect the Cherenkov light emitted when an electron pass through the fused-silica. The detector are placed inside the two spectrometer of the A1 hall, which are not used in this experiment due to the high luminosity of the beam (20 µA) that is above their limits of operation. The asymmetry due the change of the electrons spin is the aim of the measurement. The pmts signals are collected and digitalized by the **NINO** board, after a threshold selection, and sent to the A1 control room computer, where the DAQ program collect the data together with all the data coming from the Beam monitors producing Binary files, which are later analyzed by the analysis program, which is significant part of the work done in the framework of the thesis. The data collected are divided in *Events* made by 4 *sub-events* in sequence. Each event correspond to a temporal window of $\simeq 80$ µs, where each sub-event is 20 µs long. Here it's important to clarify that unlike the majority of experiments in high energy physics, an event is made by all the electrons interacting with the detectors during the time interval of the event, and we will refer to this hereafter unless otherwise stated. The division into sub-events reflects the polarization sequence of the beam. The PMTs counts and the beam monitor values are saved for each sub-event, along with the time length of the event (measured by in clock cycle by the NINO electronic board 3.6.2), and other values which are required to process beam monitor data.

The general structure of the event is the following:

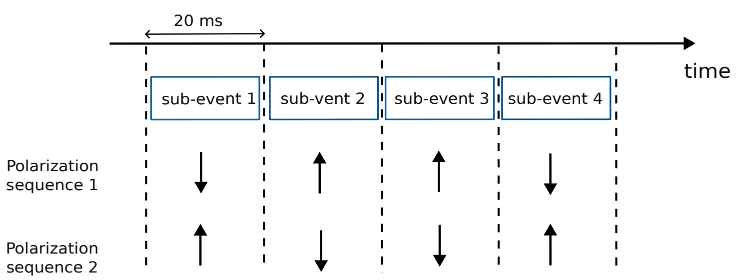

Figure 3.1: Event structure

For each event we have a single measure of A_n, defined ad the asymmetry between the ↑ and ↓ sub-events. At the beginning of an Event on of the two polarity pattern are selected randomly using a De Bruijn sequence. A De Bruijn sequence of order n is defined as a cyclic sequence where every sub-sequence of length appear only once. We have to different polarization pattern, the ones shown in the figure, that can be represented as 1 and 0. For this experiment, the De Bruijn sequence is of order $n = 6$ bits; this correspond to all the possible sequence of 1 and 0 with a length equal to 6, which are 64 different sub-sequence. It's possible to demonstrate that exist exactly N_{bruijn} sequences:

$$N_{bruijn} = \frac{(k!)^{k^{n-1}}}{k^n}$$

If we substitute in the formula above $k = 2$ and $n = 6$, we have a total of $\simeq 67 \cdot 10^6$ different sequences. The seed of the De Bruijn sequence is generated with a random number generator, and the sequence is used to select between $\uparrow,\downarrow,\downarrow,\uparrow$ and $\downarrow,\uparrow,\uparrow,\downarrow$. at this point it could be objected why so much care is taken in choosing randomly the two sequences. At a first glance is certainly easier to select one of the two polarization pattern and reproduce it for every sub-event. However, this doesn't protect from systematic effects. Let's suppose that we have a noise, whose frequency is roughly 10 Hz. This kind of noise could in principle increase the rates for one polarizations state and decrease the other. The solution to reduce the noise effect is to randomize the pattern. In the end, there is another reason why a debruijn sequence is useful. During each polarization flip, we observe a short, transient reduction of the beam current. This reduction in the beam intensity has more influence on patterns where there are more inversion of the polarity respect to the other. With a debruijn sequence we assure that we have a identical number of pairs of patterns, meaning that:

- 25% : $\uparrow,\downarrow,\downarrow,\uparrow$; $\uparrow,\downarrow,\downarrow,\uparrow$
- 25% : $\downarrow,\uparrow,\uparrow,\downarrow$; $\downarrow,\uparrow,\uparrow,\downarrow$
- 25% : $\downarrow,\uparrow,\uparrow,\downarrow$; $\uparrow,\downarrow,\downarrow,\uparrow$
- 25% : $\uparrow,\downarrow,\downarrow,\uparrow$; $\downarrow,\uparrow,\uparrow,\downarrow$

In the top rows we have 4 inversion, while in the two lower rows we have 5 inversion. Later we will describes the other details of the experiment; in the next sections we will present briefly MAMI accelerator, where the experiment is performed.

3.2 Mami

MAMI is the electron accelerator located in Mainz, which provides a continuous wave, high intensity, polarized beam for nuclear physics experiments with fixed-target. The concept of the Mainz microtron accelerator is born in the early 1970s, when the researchers of the nuclear physics institute were investigating the possibility of generalizing the concept of the racetrack microtron (RTM), that consists in a linear accelerator (linac) and two deflection magnets (180° magnet, see the figure). The particle recirculate, due to the deflection magnets, several time in the linac, and each time they gain energy. The goal of the collaboration which develop MAMI was to produce a continuous beam, with energies above 1 GeV and beam intensities up to 100 µA for high efficiency in fixed-target experiments.

A racetrack microtron, as the one shown in the figure, is characterized by the energy gain per-cycle δE given by the high-frequency electromagnetic field (HF). The energy gain is:

$$\delta E \; = \; eU_{Linac} \cdot cos(\phi)$$

U_{Linac} is the maximum voltage of the linac, and ϕ is the phase of the beam relative to the maximum of HF. Because the particle are accelerated by the linac, the beam consist in individual packets (bunches) whose rate correspond to the ω of HF. In order for the electrons to be accelerated for each recirculation step, they must arrive at the beginning of the linac with the correct phase ϕ. For this it is important that the flight-time per cycle must be an integer or a multiple of the HF period.

$$f = \frac{1}{2\pi} \cdot \frac{q}{\gamma m_0} \cdot B \tag{3.1}$$

From this overview two conclusion can be drawn:

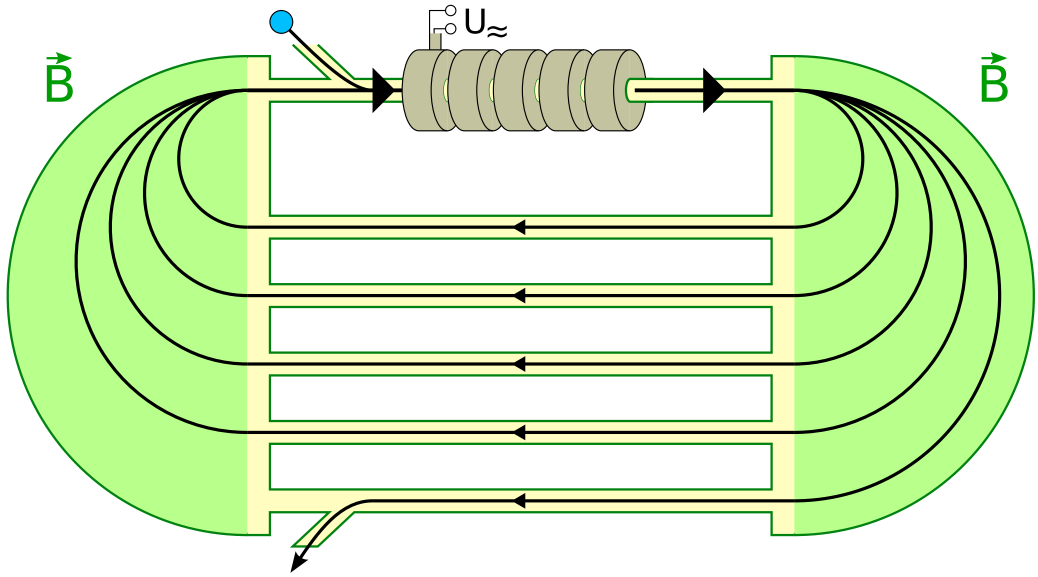

Figure 3.2: Racetrack Microtron. The particles are sent to the linac, and the two deflection magnets make the particles recirculate, until the momenta exceed the capability of the magnetic field.

- To accelerate slow electrons, with $\gamma = (1, 10)$, a magnetic field of 0,1 T is used, in order to work with frequencies of (2 GHz,2 GHz), that are easy to control. However with higher energies the bending radii is higher, with a small magnetic field.
- For high energy electrons $\gamma > 10$, to reduce the size of the deflection magnets, it is useful to increase the Magnetic field up to 1 T of more. This let to accelerate the electrons using the same technology for $f \simeq$ GHz.

These conclusions justify the structure of MAMI: a cascade of microtrons to reach each time higher energies with the same acceleration frequency at each stage. MAMI is composed by a sequence of 4 different microtrons, to achieve energies of 1,6 GeV. The first stage, shown in the picture (3.6), is composed by two small microtrons that accelerate the particle to 14 MeV in 18 revolutions. The Particle then are sent to the RTM3 (race track microtron 3), that is a large microtron that can accelerate the particle up to 855 MeV. These 3 microtrons forms MAMI-B, which started operation in 1990-91. A four stage, MAMI-C, was built and started operation in 2007. This four stage is made by 4 bending magnets, with a bending angle of 90°, and it is designed to achieve energies of 1,6 GeV. The design is different from the other race-track microtrons, and will not be explained, as it is not necessary for the experiment to reach such high energies.

The operation principles of a microtron are simple to be described. First we conside the gyro-radius for relativist electrons, that is:

$$r = \frac{E\beta}{qcB} \tag{3.2}$$

To have a coherent conditions, we must have that the flight-time $\tau = \frac{\lambda}{c}$ of the first recirculation must be an integer multiple of the HF 3.1. This means that:

$$\lambda = \tau c = \frac{2\pi cR}{\beta c} = \frac{2\pi E}{qB} = m\lambda_{HF}$$

For the other recirculation, we must have that the flight-time at energies $E_i = E_{n-1} + \delta E$ must be increased by an integer multiple of HF, too. This lead to the second equation:

$$\frac{2\pi\delta E}{qB} = n\lambda_{HF}$$

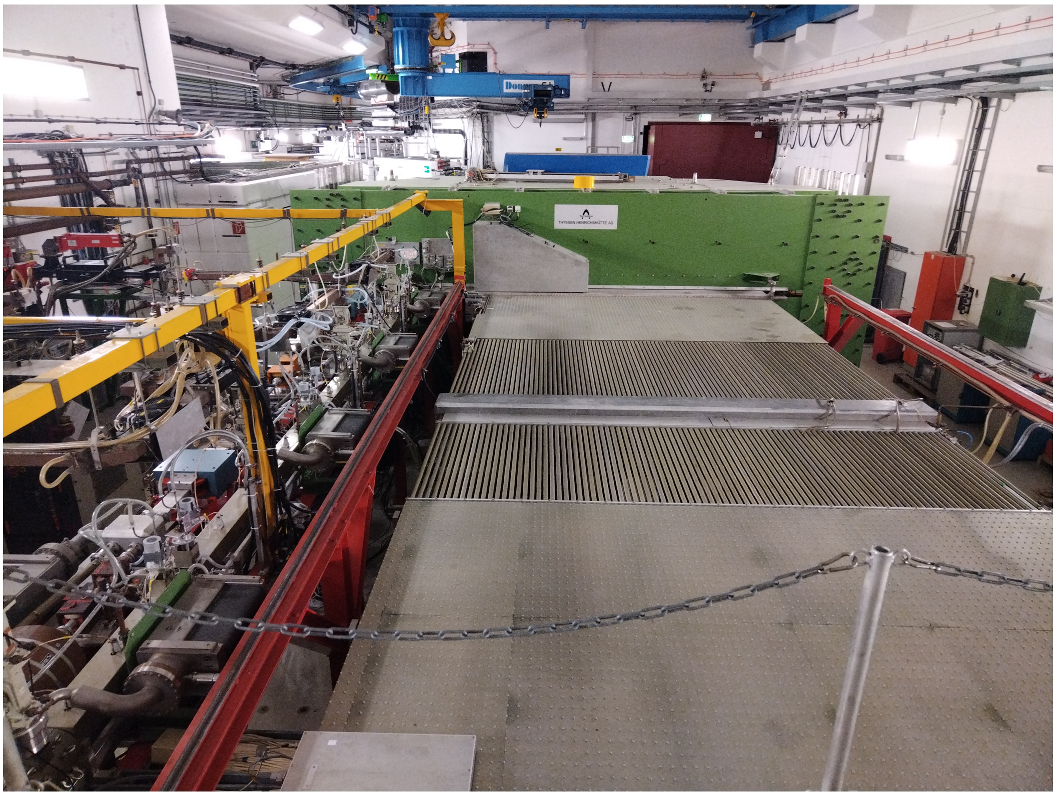

Figure 3.3: Picture of the Racetrack RTM3 in MAMI-B. The Green square at the bottom is one of the deflector magnets, the other one is below the point where the photo was taken. The linac stage is on the left. The tubes at the center of the figure are the paths that the particle cross during the recirculation. The further away from the linac the greater the energy.

The minimum gain per cycle is then determined only by the strength of the magnetic field and wavelength λ_{HF}. These two equations together controls the dinamic of the race-track microtrons,

3.2.1 Polarized Beam

For the beam-normal single spin asymmetry a vertical polarized beam is necessary. At the MAMI electron accelerator is possible to produce a vertical polarized beam with energy in the range $180\,\mathrm{MeV} - 855\,\mathrm{MeV}$ [16]. In this section the procedure to orient the beam vertically is presented, following an explanation of how the degree of polarization is measured.

The electron source used at MAMI is made by a strained GaAs/GaAsP super-lattice photo-cathode illuminated by circular polarized light. To alternate the sign of the light polarization, a fast Pockels cell ([]) is installed in the optical system of the electron source. The Pockels cell is a wave plate controlled by the electric field, that changes the helicity of the photons impinging on the electrons. A Pockels cell exploit the Pockels effect, that affect crystal with particular characteristics (lack of inversion symmetry). For this type of materials the refractive index is linear dependent on the applied electric field. By controlling the refractive index with the electric field, the polarization state of the incident light beam is altered. Once an photons imping on and electron, the extracted electron carries the same helicity of the incoming photon:

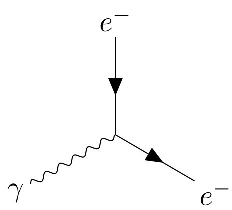

$$(Jz)_\gamma = \pm 1 \qquad (Jz)_{e^-} = \mp\frac{1}{2} \rightarrow \pm\frac{1}{2} \tag{3.3}$$

With the fast change of the Pockels cell it is possible to alternately revert the sign of the polarization. By the insertion of a $\lambda/2$ plate between the laser system and the photo-cathode the global polarization orientation of the electron beam can be reversed. This is particularly useful because this directly change the sign of the physical asymmetry measured by the detectors, and allows to identify systematic errors. This is useful done for longer beam time, where two sets of data are taken, reversing the orientation of the $\lambda/2$ wave plate. By comparing the results for the two sets of data, the influence of the optical system on the asymmetry measurement is estimated. During the beam time of interest for this thesis, the $\lambda/2$ wave plate orientation was fixed. During previous beam time ([8]). The beam polarization achieved with this source is roughly $P = 80\%$, so the measured asymmetry are:

$$A_{measured} = P \cdot A_n$$

The polarizations of the electrons just extracted from the source is still longitudinal. The Magnetic field is needed in ordet to rotate $\vec{P}$ from longitudinal polarization to transverse. For this purpose two devices are used: the **Wien filter** and a **double solenoid** located in the injection beam line, close to the the optical source:

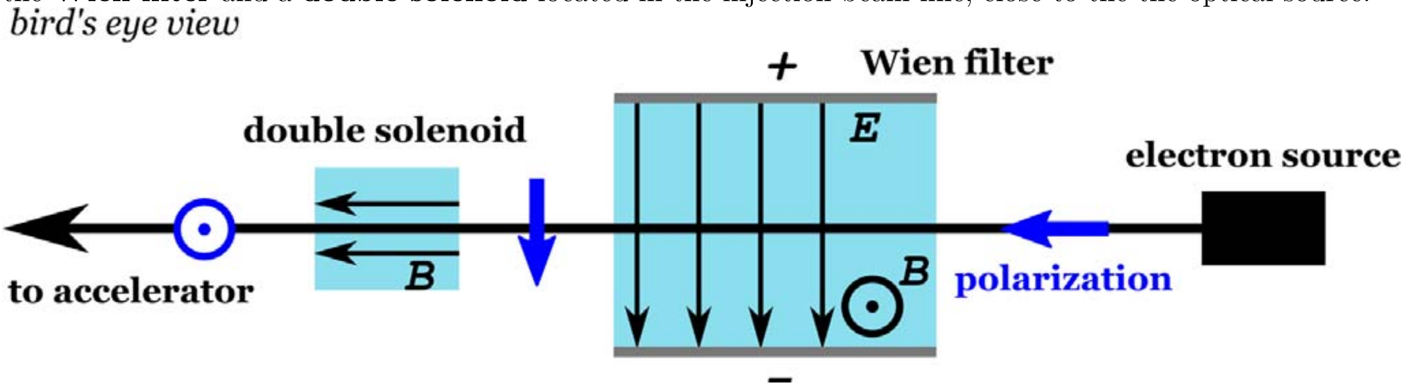

Figure 3.4: Beam line projection. This figure is taken from the paper [16]

Following the picture, the spin of the electrons from the source are rotated first in the XY plane with a 90° rotation, then the subsequent double solenoid align the spin to the vertical direction with another 90° rotation. Once the beam pass the double solenoid, the electrons go through linac, the microtron and in the end to the experimental hall, where the target of the experiments is installed. During the acceleration stage, the spin follows the precession motion due to the various magnetic fields of the accelerator, the precession, for a relativistic particle, is determined by the BMT equation. However it is not necessary, due to our particular experimental setup, the BMT equation is quite simple: the magnetic field of the various bending magnets that constitute the microtron-cascade are always parallel to the vertical direction, because of this the cross product $\vec{B} \times \vec{P} = 0$, and the polarization remain constant. Only the residual horizontal component precedes during the motion. For conventional experiment that involve longitudinal polarization, after the first spin rotation due to Wien filter and the bending magnets close to the electrons source, there is a further rotation to be considered, due to the motion of the particle during the acceleration and recirculation in the microtron. Because of this, the rotation made by the Wien is set in such a way that after the second rotation due to the motion in the accelerator, the polarization has the correct alignment in the experimental hall. The rotation angles of the polarization vector through the accelerator are known from simulations and are also directly measured for relevant energies, for a beam of 570 MeV the rotation angle is 55° with an accuracy of ±2°. In our case, this further rotation has only a small effect to the residual horizontal component, whose effect is negligible because it is accurately minimized by MAMI operators at the beginning of the beam time. Besides this, the effect of a small horizontal polarization on the asymmetry is small, knowing that typically the transverse asymmetries are one order higher that the PV. At the beginning MAMI was not developed for experiment with transverse polarization. So it's not possible to measure directly the transverse component. However combining the measurement in the XY plane, with the existing setup, it is possible to get the polarization value also in that direction. For this purpose a Moller, Comport and Mott polarimeters are used.

3.2.2 Polarization Measurement

To Measure the polarization of an electron beam different polarimeters can be used. Here we explain briefly the physics underlying the *Mott* polarimeter, used in the experiment. Consider an electron beam that is sent towards a nucleus of charge Ze. We know from theory [10] that the spin of the incident electron is affected by the electromagnetic field produced by the nucleus. This can be described calculation the magnetic field seen by a particle with speed $\vec{v}$ near a nucleus:

$$\vec{B}_{nucleus} = \frac{-\vec{v} \times \vec{E}_{nucleus}}{c} = \frac{Ze}{mcr^3}\vec{L}$$
$$V = -\mu \cdot B_{nucleus} = \frac{Ze}{mcr^3}\vec{L} \cdot \vec{S}_{e^-}$$

The second equation represent the spin-orbit interaction potential. This term yields the polarization dependence of the cross section, and it is exploited to obtain the polarization of the incident particles. Indeed the cross section can be model highlighting the dependencies on the spin $\vec{S}$:

$$\sigma(\theta) = I(\theta)[1 + S(\theta)\vec{P} \cdot \vec{n}]$$

Let's consider an incident particle that scatter from a nucleus at an angle θ, as shown in the figure:

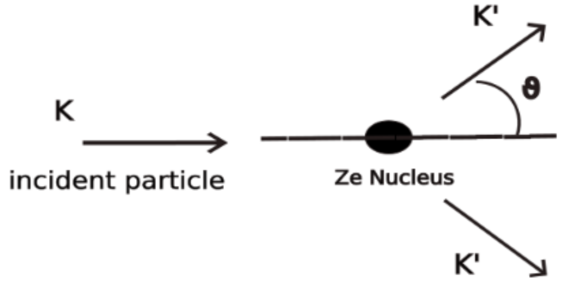

Figure 3.5: Scheme of the Mott scattering, the polarization is ortogonal to the plane, $\vec{n} = \frac{\vec{k} \times \vec{k'}}{|\vec{k} \times \vec{k'}|}$

The direction of $\vec{n}$ depends on whether scattering to the left or right is being considered. Let's suppose our initial beam has a polarization P, and so we compute the asymmetry $A(\theta)$ of the scattered electrons between left (N_L) and right (N_R). N_L and right N_R will be proportional respectively:

$$N_L = N_\downarrow[1 + S(\theta)] + N_\uparrow[1 - S(\theta)]$$
$$N_R = N_\uparrow[1 + S(\theta)] + N_\downarrow[1 - S(\theta)]$$
$$A(\theta) = \frac{N_L - N_R}{N_L + N_R} = \frac{N_\downarrow(1 + S(\theta)) + N_\uparrow(1 - S(\theta)) - N_\uparrow(1 + S(\theta)) + N_\downarrow(1 - S(\theta))}{N_L + N_R} = ... = P \cdot S(\theta)$$

From the last equation we have a relation which give the beam polarization in terms of $A(\theta)$ (which is what is measured) and the asymmetry function $S(\theta)$ (known also as Sherman function). There are several calculation of the Sherman function, which is well-known for high energy electron scattering.

The total beam polarization is measured by a Moller polarimeter, in the experimental hall, with the beam polarization oriented longitudinally in the experimental hall. The Moller polarimeter can measure the longitudinal polarization of the beam.The other two polarimeters, Compton and Mott, located behind the injector linear accelerator (ILAC), are sensitive to the longitudinal and the trasverse horizontal components of the beam (with an energy around 3,5 MeV at this stage). The procedure for the allignment is the following: at the beginning of the beam time the Mott polarimeter is used for different settings of the solenoidal field, with the Wien filter angle equal (nominal) to 90°. The aim is to minimize the horizonal polarization component after the rotation performed by the double solenoid, changing the solenoidal magnetic field. Then a second optimization follows, using the Moller polarimeter for different Wien filter angles is performed. With the new Wien filter settings, another measurement is performed with the Mott polarimeter.

3.2.3 Moller and Compton polarimeters

3.3 Experimental Hall Setup

Until now we have described how MAMI produce and accelerate the electrons, however we do not presented the structure where the beam is delivered and various experiments are carried out.
MAMI has 3 different hall, named with the capital letter A followed with a number, which indicate also the different collaboration that work with the experiments. In A2, as an example, photo-nuclear reactions are studied to investigate the fundamental physics at the scale of nuclear dimensions. The experimental hall where the experiment treated described in this thesis is conducted is the A1 hall. We will describe briefly the main operating detectors that are installed and the details that are interesting for the transverse asymmetrymeasurement.

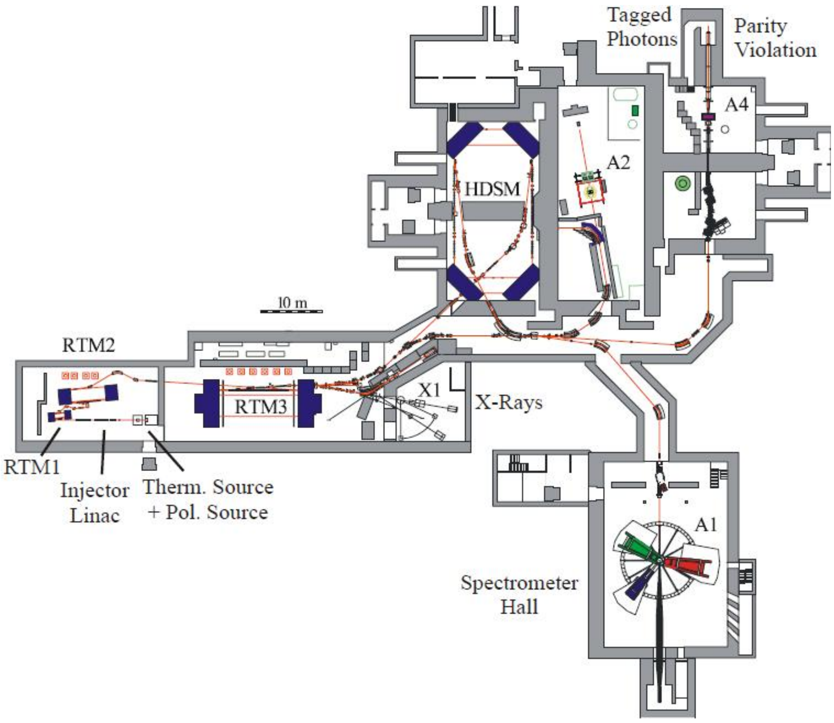

Figure 3.6: Scheme of the accelerator, with the different experimental hall. Actually the A4 hall is restructured, in fact it will host the future Mesa accelerator.

In A1, experiment with fixed target are conducted. The electrons can be delivered with an energy up to 1,6 GeV, after passing the last acceleration stage (HDSM, in the figure). Because the electron energy of our experiment is 570 MeV, the beam will pass through the first acceleration steps, the linac (linear accelerator) and Race-track system and when the desired energy is achieved the electrons will be sent to the A1 experimental hall.

Inside A1 hall three large magnetic spectrometers are placed on a circular rail-track the target chamber. These spectrometers where designed and built in 1993 to perform high precision measurement of electron scattering in coincidence with other hadron detection, with an high resolution in the determination of the particle momenta $\frac{\delta p}{p} < 10^{-4}$. The spectrometers develop vertically with an height of 15 m, for this reason the scattered electrons and the other particles are deflected with the use of the magnetic field respect to the scattering plane. The following figure shows the path the particle scattered from the target:

The spectrometers used for the transverse asymmetryare the ones shown in the picture. The are multiple reasons why the particle are deflected on the vertical direction, we summarized them in two points:

- reason of space, due to the fact the an horizontal setup would not fit with the dimension of the building in addiction to the fact that this would not allow to rotate the spectrometers by a variety of angles that the vertical orientation does

- reduce background and noise, in fact the high beam intensity that is possible to reach at MAMI is a

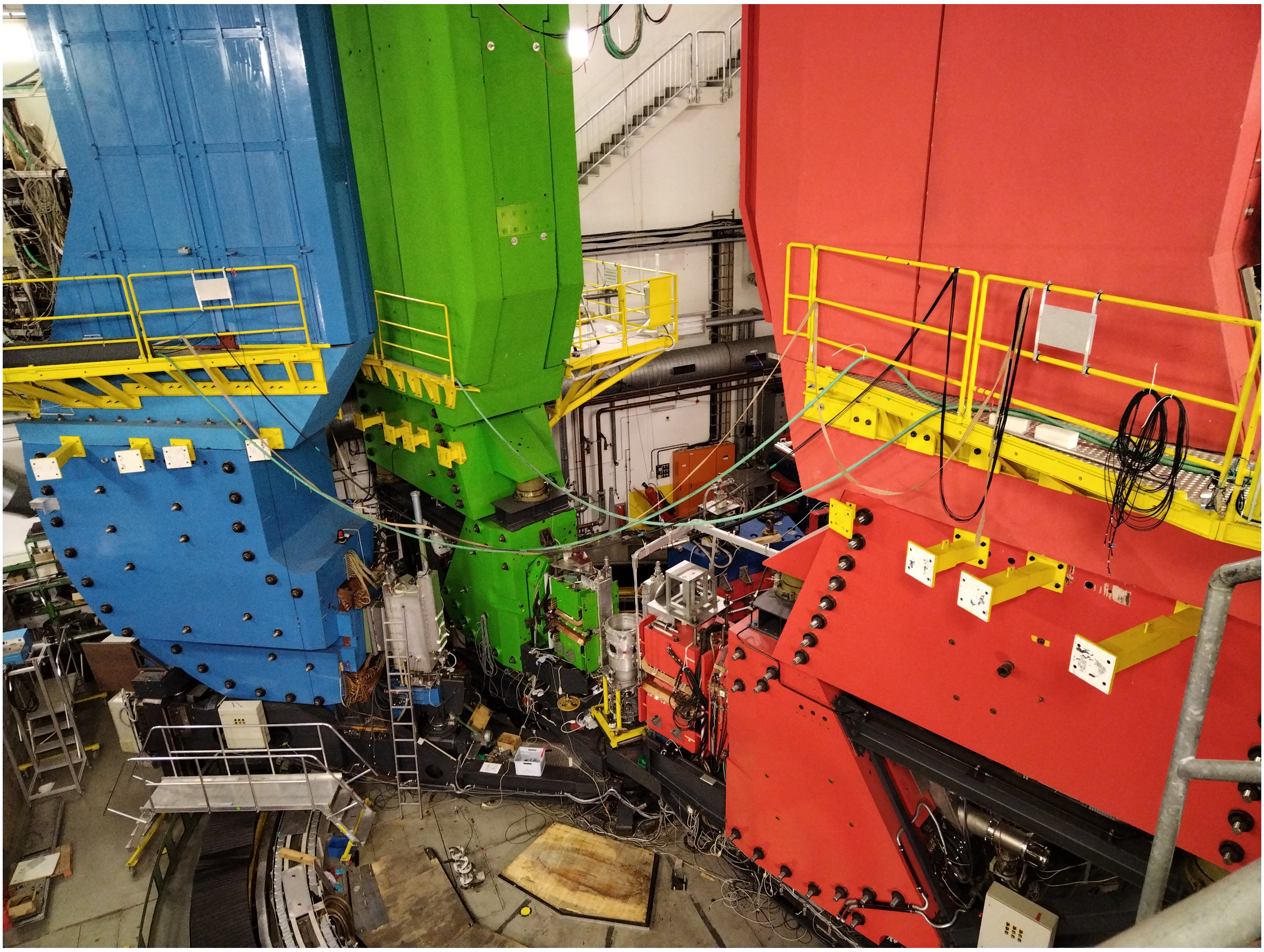

Figure 3.7: Picture of the A1 spectrometers hall, the spectrometers red and blue are used during this experiment. At the center of the picture is possible to observe the scattering chamber.

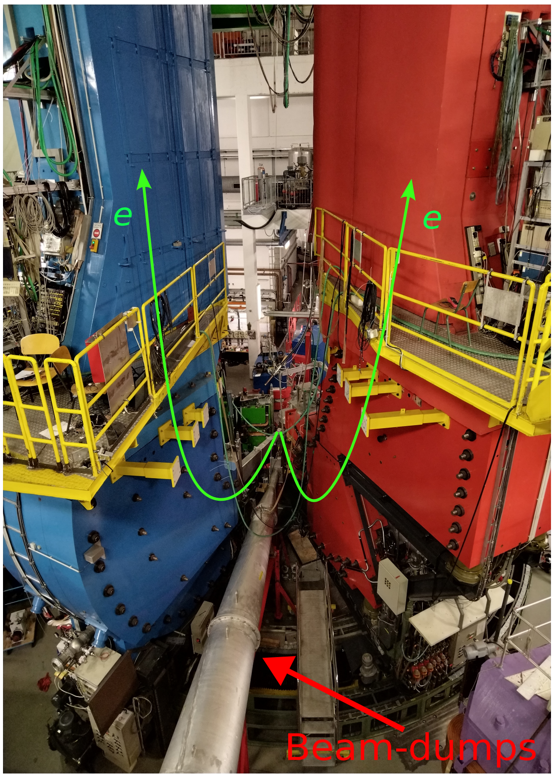

Figure 3.8: Image of the spectrometers of A1 hall. The spectrometers can be rotated using a system of rail-tracks that are visible at the bottom of image. The electrons are scattered and then deflected in the vertical direction by the magnetic field (green lines). This picture is taken from behind the target, so we see the beam-dumps. The target is roughly at the center of the image where the two green lines join. The electron are coming on the opposite direction, respect to the spectrometers.

source of noise and background event wich can be cut off detecting the particle far from the interaction point.

Once a particle is scattered in the acceptance region of the detectors, the magnetic field deflect the particle that passes through a drift chamber, which occupies the first third in height of the spectrometers.

When the particle is at the height of the platform in the figure, it impinge on a layer of plastic scintillator, and after that a Cherenkov detector which measures the particle speed $\vec{v}$.We have a picture of the spectrometers internal, taken during the installation of the two detectors (that will be presented in the next section) 3.9.The determination of both the particle speed $\vec{v}$ and momenta (drift chamber) allows to identify the particles. Despite the possibilities offered by the already existing setup, for the beam time of interest none of these components was used directly in the estimation of A_n. The reason is due to the high intensity of the beam that is used in the experiment, which is far from the optimal operating conditions of the components, that are suited for rates lower than the ones expected for beam normal single spin measurements. The spectrometers are used indirectly for the alignment of scattered electrons to the focal plane of our detectors.

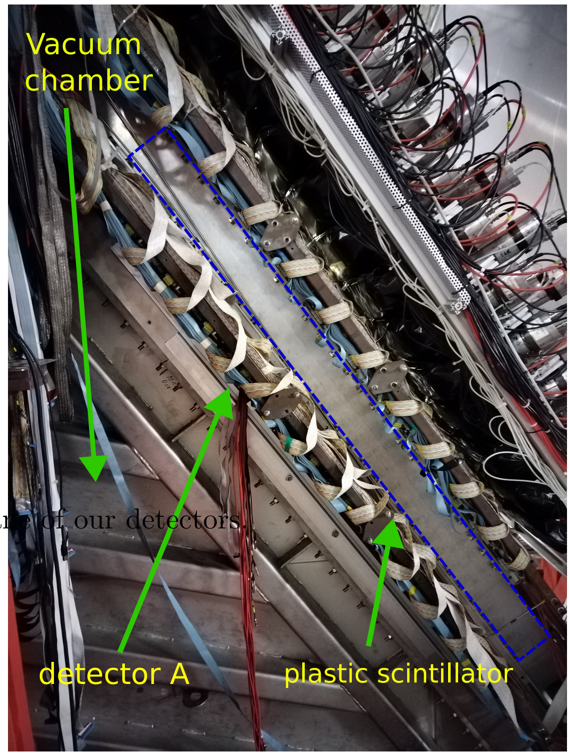

Figure 3.9: Internal of the spectrometer. This image was taken during the installation of the detector A inside the red spectrometer, that is accessible from the platforms visible in the picture : 3.8

3.4 Detector Description

In this section we will describe the electronics and the detectors used to measure the transverse asymmetry. For this experiment we are going to measure the transverse asymmetryat to different angles. The electrons detection is made via two thin blocks of fused-silica that are coupled to PMTs. When a scattered electron hit the fused-silica (refractive index $n = 1.45$) Cherenkov light is emitted. The emitted Cherenkov light can interact with the electrons of the material, which, in turn, can hits the PMT dynode. This sequence of event triggers the PMT and produce an output signal.

In the experiment, we will measure the transverse asymmetryat two angles of scattering, so two detectors are installed and read-out independently. The two detector are made by 3 PMTs and 8 PMTs coupled with two blocks of fused-silica, a scheme of the detector is shown below:

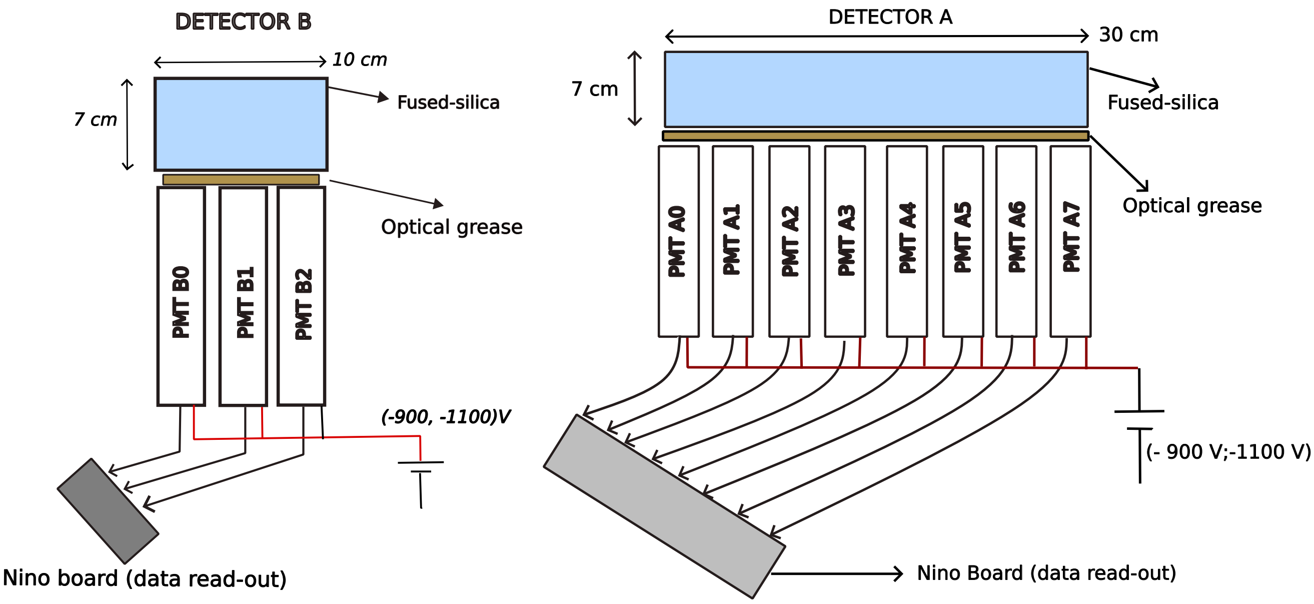

(a) *Detector B scheme.* (b) *Detector A scheme.*

These two detectors are placed inside the spectrometers presented in , between the top of the drift-chamber, which occupies the first third in height of the spectrometer, and just below a panel of scintillator. During the beam time the drift chamber of the spectrometers is turn off, and also the PMTs coupled to the spectrometer scintillators are not powered.
As we mention above, the scattered electron are deflected in the vertical direction by the magnetic field of the spectrometer. At this moment, it is important to mention the differencies between the new and the old electronic setup. In the old electronic setup the output signal of the PMTs was integrated during the time interval of each sub-event, and therefore the single scattered electron could not be counted. The advantage of this method is that the electronics is more simple, in fact there in no need to develop a fast counter, unlike the new setup, where the new electronic take into account of every pulses. However, this old method is effected by a baseline noise and it is not good for the future experiments with lead target, where the expected rates are lower than the rates on carbon. With the new electronics, all the single electron are counted, and this will allow the future measurements with lead, improving the accuracy.

Here we report the characteristic of the two detector that are relevant for the data analysis:

- detector B size (lenght, hight, depht): $7\,\text{cm} \times 10\,\text{cm} \times 1\,\text{cm}$
- detector A size (lenght, hight, depht): $7\,\text{cm} \times 30\,\text{cm} \times 1\,\text{cm}$
- Number of dynodes: .
- The Power voltage for the PMT in negative, in the range of $(-900\,\text{V}, -1100\,\text{V})$
- refraction index n of the fused-silica is 1.45.

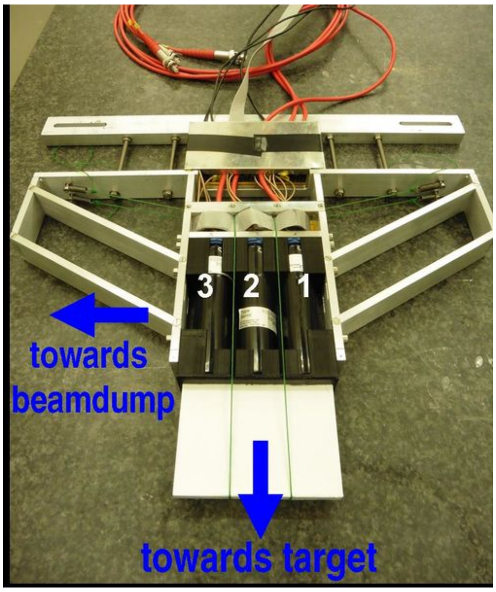

(a) *Detector B*

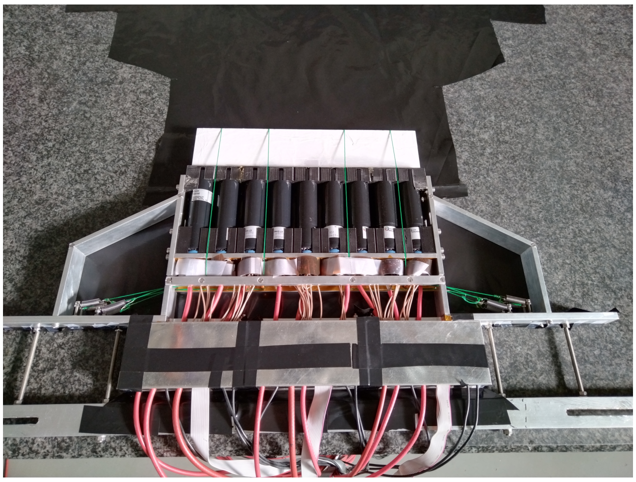

(b) *Detector A*

Figure 3.10: Picture of the two detector taken in the clean room. The white blocks are the fused silica that produces the Cherenkov light, the cylinders below are the PMTs.

3.5 Beam Monitors

In MAMI, several monitors are placed along the beam line in order to to check beam quality and measure parameters such as current intensity, energy and relative position of the beam. This section summarize an explanation of the operating principles of the monitors installed at MAMI. The explanation will be partial, some details will be given in the appendix, however for a complete discussion please refer to the following paper ([7]).

The monitors avaible at MAMI are quite specific for the standard of the particle accelerators. Resonant cavities are used to measure the various quantities, with the underlying physical principle that the passage of charged particles through these cavities can excitate some electromagnetic resonant modes[1] which can be detected and analyzed by an analogic circuit to measure the beam parameters. Before going into the details, is necessary to define some quantities that will be used later in the explanation. We define r_s, the Shunt-impendence as :

$$r_s = \frac{|V_{\|}|^2}{P} \tag{3.4}$$

P is the power absorbed by the cavity when a particle excites one of the resonant mode, instead $V_{\|}$ in defined as the effective voltage surpassed by a charged particle along a straight line, which can be computed as:

$$V_{\|} = \frac{1}{q}\int_{s_0}^{s^1} \vec{E}_s \vec{e_s}\, ds$$

The Shunt impedence is a measure of the interaction strenght between a cavity and a charged particle, and can be espressed also in another way, introducing the Q value of the cavity, W the maximum energy stored and f_r the frequency of resonance:

$$r_s = \frac{|V_{\|}|^2 Q}{2\pi f_r W}$$

[1]TM mode, where the magnetic field is completely trasverse respect to particle momenta

When the beam travel through the cavity, the particles release enery that excites the oscillascion mode. The power P_{HF} extracted from the beam is related to the beam current:

$$P = \iota^2 r_s$$

An antenna is used to decouple part of the energy from the cavity and send it to a circuit which produces an analog output signal. Indicating with κ the coupling costant of the antenna, the previous relation need to be modified introducing a new factor $\frac{\kappa}{(1+\kappa)^2}$. In a Cylindrical resonator, the same type installed at MAMI, the resonance frequency of the different oscillascion modes is expressed by the formula

$$f_{m,n,p} = \frac{c}{2\pi\sqrt{\epsilon_r \mu_r}} \sqrt{(\frac{x_{m,n}}{R})^2 + (\frac{p\pi}{L})^2}$$

The constant in the formula are:

- c is the light speed.
- ϵ_r, μ_r are the magnetic and dielectric costant of the material.
- $x_{m,n}$ it the n-th zero of the m-th Bessel function.
- R and L are the radius of the cylindrical cavity and his lenght.
-

This formula can be obtained solving the Maxwell equations with cylindrical boundary condition, the eigenvalues are the given by the formula above.
If the frequency of the Beam bunch is equal to the resonant frequency $f_{m,n,p}$ of the cavity, a TM mode is excited. At MAMI high quality monitors are installed, quantitatively all the monitors have a $Q \simeq 10000$, that means that $\frac{\nu}{\delta\nu} \simeq 10000$. This means that the frequency of the beam buch must be very close to the frequency of the resonant cavity. At MAMI the frequency used for all the resonators is 2,449 532 GHz or a multiple of it. The beam bunch frequency is the same, and it is controlled by the MAMI-master oscillation signal, that is the reference signal for all the MAMI monitors.

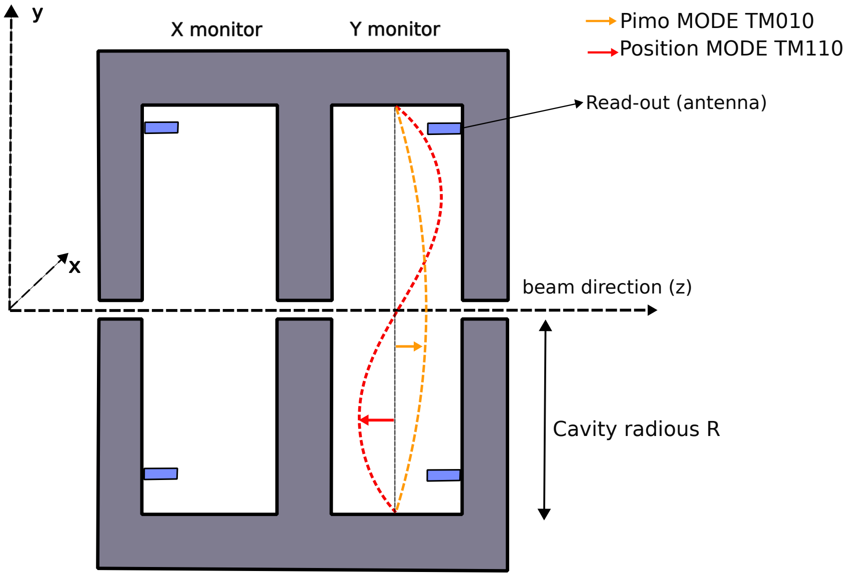

Figure 3.11: Scheme of the Cylindrical cavities installed at MAMI. In red we have the TM_{110} mode, used to measure the position of the beam, in yellow the TM_{010} mode, to measure the intensity of the beam.

Depending on the TM mode excited, we have a different signal in the cavity, so a different signal collected by the antenna. The relevant quantity that is detected is the power P_{HF} absorbed by the antenna. For the TM_{010} mode, the power is

$$P_{HF} = i^2 r_{010} \frac{\kappa}{(1+\kappa)^2} \tag{3.5}$$

The power absorbed by the antenna is directly dependent on the beam current. Because the rage values are typically in the range of pW to mW, the signal is processed in close proximity of the installed monitors. In the signal process, the input signal of the antenna in coupled to the master-oscillascion signal, so the output signal is given by the formula:

$$U = \sqrt{P_{HF}} \cos(\phi - \phi_{LO}) \tag{3.6}$$

the phase ϕ is the phase of the resonant mode or the phase of the beam bunch, while the phase ϕ_{LO} is the phase respect to the master-oscillation signal, and can be adjusted by a phase shifter of the circuit. The output voltage signal can be read out with the oscilloscope or digitalized and saved with other devices. To measure the beam intensity is important to minimize $\phi - \phi_{LO}$, to maximize the signal amplitude, and then the output signal is ready to be analyzed.

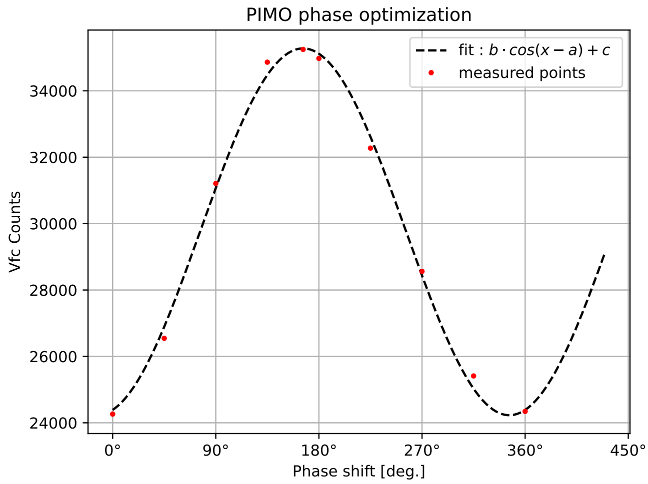

Figure 3.12: Plot of the phase ϕ versus the output signal. The phase optimization was done selecting the working point in correspondence of the peak.

The measurement of the x, y position follows in principle the same procedure. In this case the TM_{110} is acquired. The reason is clear, because it is possible to calculate that for this mode the r_{shunt} is proportional to the beam position on the x, y plane. So The power absorbed by the antenna can be written:

$$P_{HF} = i^2 r_{110} \frac{\kappa}{(1+\kappa)^2} K x^2 \tag{3.7}$$

The output signal, that is read by our setup, is proportional to the square root of the absorbed power:

$$\sqrt{(}P_{HF}) = costant \cdot U \cdot i \cdot x \tag{3.8}$$

The beam parameter are then given inverting the above formula

$$x \simeq \frac{\sqrt{(}P_{HF})}{i} \tag{3.9}$$

Where the exact conversion coefficients are not known, and are determined during the calibration phase, at the beginning of the beam time.

3.5.1 Beam stabilization

The beam stabilization is an essential component of the experiment. The values of A_n that we want to measure are in the order of ten ppm, so it is important to reduce other contributions that can be related to variations in the beam parameters.

3.6 Electronics

3.6.1 VFCs

Some parameters which describe the beam are needed in order to take into account possible effect in the measure of the Trasverse asymmetry. The relevant data are the position in the (x, y) plane, the incident angles on the target, the current and energy of the beam. All this values are collected using the already existing monitors.
To collect the data from the monitors, single and multichannel, synchronous voltage-to-frequency converters (AD7742) are used. This devices contain an analog modulator that is able to convert the input voltage into an output pulse train, whose frequency is proportional to the input voltage.

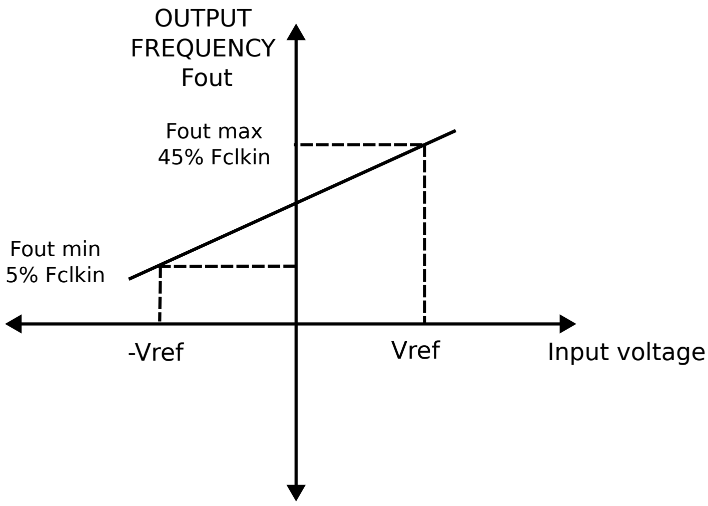

Figure 3.13: Frequency versus Voltage

The VFCs are powerd with an external tension of 5 V, and a differential voltage input in the range $(-V_{ref}, V_{ref})$ is also applied. An external clock signal, that is indicated with "CLKIN" is provided as a reference signal for the oscillator frequency. The analog input signal is sampled with by a switched capacitor, with a rate that is controlled by clock that can be supplied externally, in our case we used a 6 MHz. A scheme of the electronic circuit is drawn here (*aggiungere figura*), the output of the Comparator is a fixed width pulse (the pulse is initiated by the edge of the clock signal) with a frequency that goes from $0.5\% \cdot f_{CLKIN}$ to $0.45\% \cdot f_{CLKIN}$ [1], where the first correspond to 0,0 V in input and the second to V_{ref}. Neglecting possible systematic errors, the relation the output frequency and the input voltage is the following:

$$V_{in} = \frac{V_{ref}}{40\% \cdot f_{CLKIN}}(f_{out} - 5\% f_{CLKIN}) \tag{3.10}$$

We control the f_{CLKIN} with the period of the clock. The data are acquired counting the number of pulses that come from the comparator, so we can substitute to f the number of pulses (the two quantities are proportional), and we end with:

$$V_{in} = V_{ref}[2 \cdot \frac{N_{pulses} - 5\% N_{CLKN}}{40\% N_{CLKN}} - 1] \tag{3.11}$$

3.6.2 Nino Board

The NINO board is our data acquisition system for the PMT counts. It is made by 32 analog input channels and it is powered with ± 5 V. Each channel has an attenuator, and the signal pass through that before going to the Comparator, which compare the signal to the threshold. The Output signal is a Low-voltage differential signaling (LVDS). Each comparator can handle eight channel and for each of them it is possible to define a global threshold. With the current settings of NINO board, it is possible to change the threshold of each channel acting on another value, the attenuation, which decreases the value of the global threshold. All the value that can be modified are 12 bit numbers, so a setting interval of $(0.; 4095)$. The NINO board is designed in such a way that collects the Input charge of the signal, operating with a 30 pF. The output signal amplitude is proportional to the input charge, and it is sent to the discriminator. Our interest is only to count the number of scattered electron, so we do not intend to measure the input charge, but only a signal is produced or not.

Two Nino board are used in the experiment, one for detector A and one for detector B. For the experiment discussed in this thesis, we will use only 8 channel for detector A and 3 channel for detector B, since this is the number of the input signals coming from the two detectors. For the future experiments more channel will be used, splitting the analog input signal in 4 different signal, sending it to 4 different input channel of the board. This is useful because changing individually the attenuation value, we can define 4 different thresholds for the

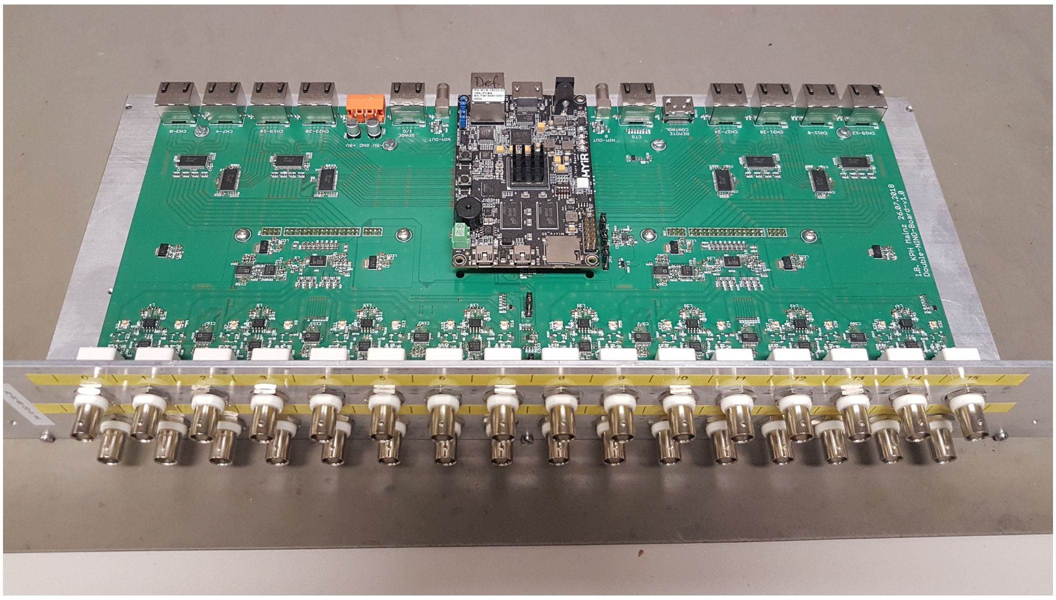

Figure 3.14: Nino Board

same signal coming from a single PMT. This is something useful to compare different values of threshold, for example to study how the noise affect the measurement, and see what is the right compromise between signal and noise . The way we selected the threshold is explained in the following chapter (Analysis).

3.6.3 Master Board

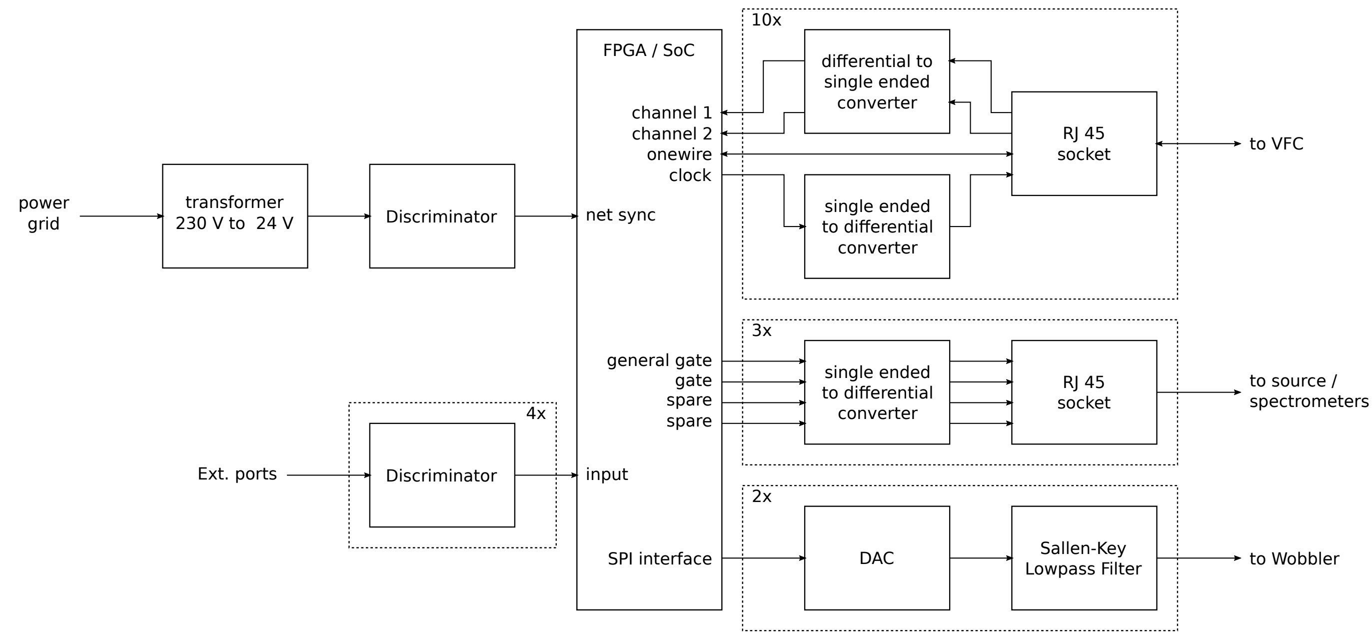

Figure 3.15: Scheme of the master-board, the device that coordinates all the electronics for the experiments, and send the data to the computer in the control room.

Chapter 4

Detectors Test, Alignment and Calibration.

In this chapter we discuss the electronic test that have been carried out in the laboratory, and the calibrations that need to be done in order to calculate, from the raw data, the final data ready for the analysis. The test in the lab consist in checking that the photo-multipliers are working and that the electronics that take care of acquiring the data do not have any errors. For the calibrations, since several beam parameters are needed for the analysis, it's important to obtain the correct scaling factor to convert the Raw Data collected by the *VFC*s to data with the right physical units. The important quantities are the X, Y impact point coordinates of the beam,the energy E, the beam current I and the scattering angles θ_x and θ_y.

4.1 Nino Board

In this section we explain briefly simple test that we performed to control that the two detectors are working properly.Before going into detail it is important to describe again the operation of the NINO board, which interfaces directly with detectors. The Nino board, which digitizes the signal from the PMTS, has two parameters which can be used to select the internal threshold of the discriminator, to cut out the low amplitude signals, that are indicated as threshold and attenuation. The threshold and attenuation values can be adjusted changing the settings of the DAQ program. For our purpose, we fix the threshold values equal to 600 for all the detectors. We remind the reader that the values should be in the range $(0, 4000)$. It is desirable to work with the "physical" values, i.e switch from these arbitrary units to the correct value in mV. The relation between attenuation and threshold it is not linear, the reason is that the NINO board is designed in such a way that collects the input charge coming from the signal. In principle it is even not possible to define a unique value for the threshold in mV, because signals that produce the same charge can have shape and amplitude different from each other. In simple word, from the definition of the current:

$$Q = I \cdot time \tag{4.1}$$

Signal with a large time width and a small amplitude can generate the same accumulation of charge respect to narrow signal with high voltage amplitude. Despite this, some data have been acquired by the A1 collaboration, with which it's possible to define a raw conversion function from attenuation units to threshold. The basic idea is to fix th time-length and the shape of signal and vary the amplitude, then we can observe the minimum value of attenuation for which the NINO board collects the input signal. We are aware that for electrons that hit the detectors, the shape of the signal cold different, and are not fixed, however this procedure let us to have at least a first rough estimate of the threshold value.

The data show represent the values of the amplitude of the input signals (in mV) versus attenuation, the function used for the conversion is obtained from the fit of the data, the function used is the following:

$$Threshold = \frac{a}{(att - b)^3} + c \tag{4.2}$$

The values obtained from the fit are:

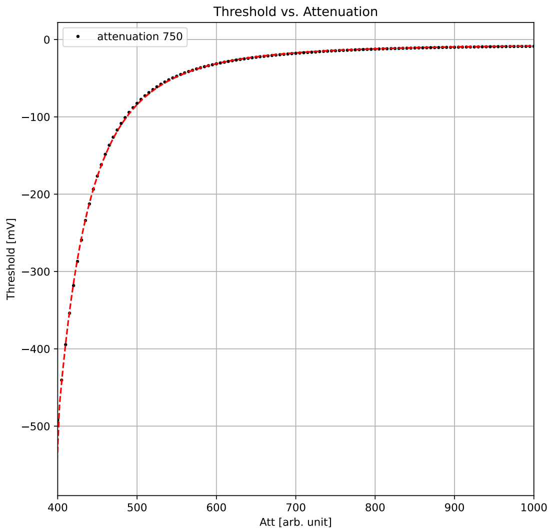

(a) *Threshold dependence against attenuation*

- $a = -802111053\,\frac{\mathrm{mV}}{[arb.unit]}$
- $b = 382\,[arb.unit]$
- $c = -6{,}1\,\mathrm{mV}$

4.2 Detector Test

Before the Beam time, some test with the two detectors were performed, to check that the pmts were still working after some years of inactivity, and that the new electronic was able to count properly the pulses and store the data. For this studies, we didn't have a radioactive sources to employ, so we moved the two detectors in the workshop of the accelerator, and we use the cosmic rays rate as a probe.

Knowing that the expected number of event for cosmic rays is about $1\frac{event}{\mathrm{cm}^2\mathrm{s}}$ we can compute the expected values for the number of events. We decided to take 1 minute long acquisition for both the two detectors, this leads to 70 expected events for detector B and 100 events for detector A.

The first step is to select a good point of work for the threshold. So, fixing the value of the threshold parameter for the NINO board, we took several acquisitions, each of them one minute long, increasing each time the attenuation. We powered the pmts with a negative voltage around $-1000\,\mathrm{V}$, as suggested in the data-sheets, and covered the cherenkov detector with a shielding blanket, to avoid ambient light simulating a signal.

We observed a small knee in the plot, around the zone of $580 - 600$ of attenuation, where the number of counts was almost constant, roughly equal to the number of expected events from muons hitting the detector. Then we observe a big edge for attenuation $= 1000$. Looking at the plot 4.1a, we assume that the attenuation values are so high that electronic noise is no longer rejected, in fact the counts grow enormously. The attenuation was set at 600.

The next step was to study the statistical fluctuation of the counts, so we collected 10 acquisitions, each of them 1 min long. The measured values are reported in the table below:

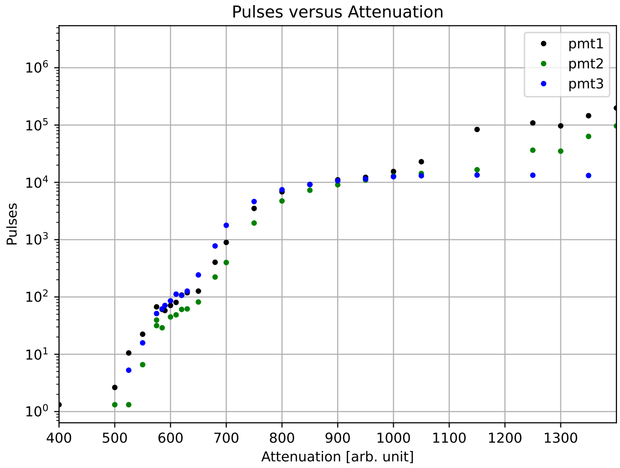

(a) *Attenuation scan for Detector B*

Pmt:	1	2	3
1	58	60	62
2	62	55	59
3	61	59	70
4	73	66	70
5	68	66	56
6	59	52	64
7	69	74	77
8	48	49	57
9	70	54	58
10	60	61	66

This data are interesting to check if the counts are following the theoretical distribution of the events expected for cosmic rays at sea level. If the pmt are working in a good mode, we know that the number of counts should be Poisson-distributed:

$$Pdf(\mu, k) = \frac{\mu^k}{k!} e^{-\mu} \tag{4.3}$$

The variance of the Poisson distribution is equal to the mean of the counts, and we expect the same behaviour also for the sample mean and the sample variance:

$$\begin{array}{lll} \mu_1 = 62.8 & \sigma_1^2 = 54.40 & r_{12} = 0.66 \\ \mu_2 = 59.6 & \sigma_2^2 = 57.15 & r_{23} = 0.65 \\ \mu_3 = 63.9 & \sigma_3^2 = 46.98 & r_{13} = 0.35 \end{array}$$

We report also the correlation r_{xy} between the pmt. The result are fine: we are able to see a positive correlation between adjacent pmt, and as expected the correlation is lower in the case of the more distant. This is explained by the lower probability that the photons of Cherenkov radiation light up at the same time pmts that are far away from each other. We can test that the data follow a Poisson distribution using the well-known Gosset test, defined as:

$$\chi^2_{n-1} = \sum_{i=1}^{n} \frac{(Oss_i - Att_i)}{Att_i} \tag{4.4}$$

We report the result obtained with the data for detector B, the test shows that there is good agreement with the hypothesis that the count are Poisson-distributed.

Pmt:	1	2	3
χ^2_9	8.52	8.45	6.37

To convince oneself that the pmt are actually measuring signals given by the passage of cosmic rays, and not only noise, we placed one pmt in coincidence with the others. If we are able to observe positive correlation between the counts, we conclude that the signal comes from the same event.

pmt	0	1	2	4 (in coincidence)
1	63	57	72	28
2	55	51	64	18
3	62	53	75	27
4	71	62	75	33
5	68	59	49	23
6	57	55	63	18
7	70	64	64	24
8	50	69	69	25
9	65	62	62	19
10	74	71	77	28

As above, we report the sample mean, the variance and the correlation between the pmt in coincidence and the detector B:

$$\mu_0 = 63.5 \qquad \sigma^2 = 58.9 \qquad r_{04} = 0.49$$
$$\mu_1 = 60.3 \qquad \sigma^2 = 43.3 \qquad r_{14} = 0.38$$
$$\mu_2 = 67.0 \qquad \sigma^2 = 71.1 \qquad r_{24} = 0.65$$

The pmt number 4, that is the pmt in coincidence with the detector, was placed geometrically over the pmt number 2. We observe a positive correlation for the values r_{04}, r_{14}, r_{24}, the correlation is higher for the pmt number 2, and less for 0 and 1, for a geometrical reason.

Pmt:	1	2	3	pmt in coincidence
χ^2_9	8.95	6.44	10.96	9.52

The same procedure was followed also for detector A. We analyzed 4 signal at a time, because during these lab test we had only one NINO board, with only 4 channels available.

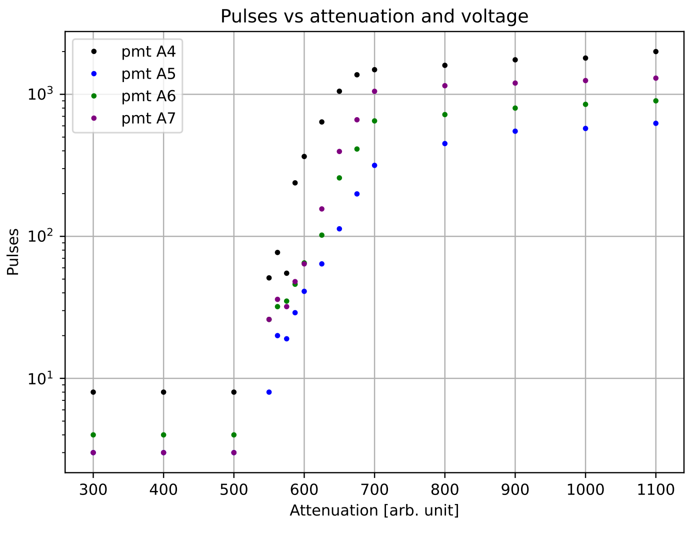

Figure 4.1: Attenuation scan for Detector A, for the pmt 4-5-6-7

We repeat the same test of detector B also for this 4 pmts, without finding any problem or strange behavior. The same procedure was repeated also for the last 3 Pmts of detector A, we took as above 10 acquisitions 1 minute long to study the count distribution, with one pmt in coincidence:

pmt	2	1	0	(in coincidence)
1	91	51	50	27
2	86	61	50	7
3	58	48	45	18
4	95	62	41	29
5	69	60	50	21
6	85	57	45	19
7	66	51	46	28
8	74	51	48	22
9	77	43	45	17
10	62	44	50	29

$$\mu_2 = 76.3 \qquad \sigma^2 = 160$$
$$\mu_1 = 52.8 \qquad \sigma^2 = 47.5$$
$$\mu_0 = 47.0 \qquad \sigma^2 = 9.6$$
$$\mu_4 = 21.7 \qquad \sigma^2 = 48.2$$

For these 4 pmts, σ^2 is different from the expected mean, this doesn't agree with the hypothesis that the count are Poisson distributed, we can quantify this with a statistical test: in this table the correlation matrix:

Pmt:	2	1	0	pmt in coincidence
χ^2_9	19.6	8.30	1.90	39.5

The expected error for the result of this test is $\sigma = \sqrt{2 * (n-1)} \simeq 4$. In this case we are observing 3 values that are more than $3 \cdot \sigma$ far from the expected value. If we look at the correlation matrix :

pmt:	c	0	1	2
c	1	-0.18	-0.21	-0.06
0	-0.18	1	-0.10	-0.22
1	-0.21	-0.10	1	0.56
2	-0.06	-0.22	0.56	1

We observe negative correlation between the pmts, something not expected. After some investigations, we find out that the program which controls the NINO board had a bug: the program partially overwrote some detector B settings for detector A as well. Since detector B has only three pmt's, the problem affected the PMT's with the same numbering as detector A. After fixing this issue we repeated the same test, without finding any problem.

4.3 Calibration

For the transverse asymmetryon ^{12}C represent an ideal test for the new electronic system. Previous measurements of the A_n have been performed at MAMI for carbon target ([]). For this beam-time, the red spectrometer is placed at the angle of $+22.5°$, and the blue one at $-22.5°$, respect to the longitudinal direction. For these two angle, we have the same kinematics and Q^2 values of the previous measurement. The exact values are reported here:

$$det.A: \qquad Q^2 = 0{,}041\,337\,\mathrm{GeV}^2 \qquad \text{without Cut}$$
$$det.A: \qquad Q^2 = 0{,}039\,451\,3\,\mathrm{GeV}^2 \qquad \text{with Cut}$$
$$det.B: \qquad Q^2 = 0{,}040\,477\,1\,\mathrm{GeV}^2 \qquad \text{without Cut}$$
$$det.B: \qquad Q^2 = 0{,}040\,584\,3\,\mathrm{GeV}^2 \qquad \text{with Cut}$$

The Q^2 values is the same of the last measurement performed at MAMI, and is measured with and without rejecting the inelastic electrons.

4.3.1 Alignment of the Scattering Plane.

4.3.2 Beam Monitor Calibration, XY Monitor

For the calibration of the X Y monitors, special target are used. In the target frame (4.2) there are two targets made by three carbon wires that are at a fixed distance each other, horizontally and vertically aligned. The distance between the center of the two external wires is measured, and it is equal to $d_{horizontal} = 2{,}38\,\mathrm{mm}$ for the horizontal wires and $d_{vertical} = 2{,}33\,\mathrm{mm}$ for the other one. The procedure to retrieve the correct scaling factor, to convert from the raw-data in V to µm, is the following: we ask MAMI operators to slowly change the beam position, in the horizontal and vertical direction for the horizontal and vertical target. The beam position can be changed by varying the Magnetic field produced by the *Wobbler 16* magnets (4.3). During this slow variation, our detectors are measuring the rates of scattered electrons, that increase when the beam hit one of the three wires and and decrease when the beam is centered between two wires. We plot the detector counts versus the XY monitors values, in voltage, and we estimate the position given in voltage of the two external peaks. This values can be used, together with the distance $d_{horizontal}; d_{vertical}$ already measured, to compute the scaling factors. This procedure is repeated for $X21/Y21$ and $X25/Y25$ monitors.

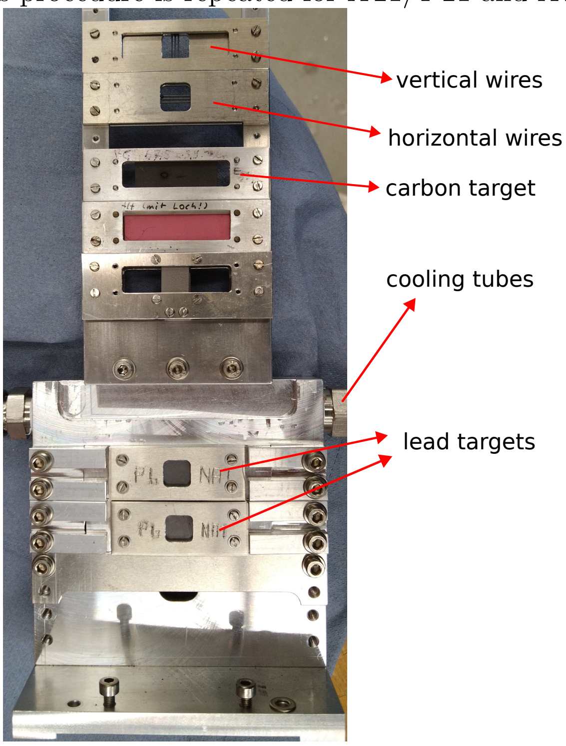

Figure 4.2: Target frame installed during the experiment, on the top we have the two targets made by three carbon wires that are used to calibrate the positions monitors. Then the carbon target and the two lead targets.

Looking at the PMT counts, we observe that the counts increase to a maximum, that is reached when the beam spot is centered on the carbon wire, and then decrease until the next carbon wire is hit by the beam. We plot the pmt data *versus* the $X25, X21, Y25, Y21$, given in V. Given that we know the real distance between the two external wires, we can obtain the correct scaling factors to calculate the X and Y position from the voltage values. To identify the three peaks in of the carbon target, we fit the data using a gaussian model (see 4.4). The mean μ represents the center of the wire, given in V.

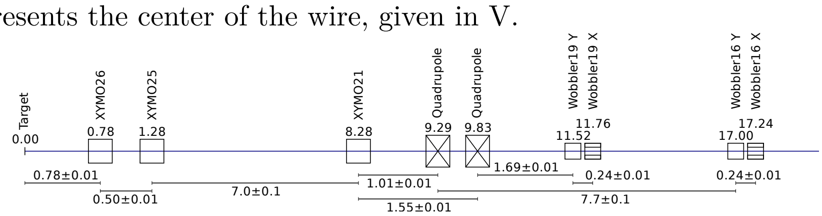

Figure 4.3: Beam line scheme.

Looking at the Beam line, we assume that the beam travels in a straight line. Let's consider the *Wobbler 16* magnet the "0" of a coordinate system, with the z axis pointing to the target (left direction in the beam scheme). The Beam parameters are measured by the Monitors $X/Y_{21}, X/Y_{25}$, which are located at some distance respect to the target. Suppose we are working only with the Y_{25} monitor (the procedure is the same for the others). The Beam y position is described by:

$$y_{beam} = m \cdot (z - z_{wobbler16})$$

In the scheme 4.3 we easily compute the distance between the Y_{25} monitor and the *wobbler 16* magnet, so we have the slope m. The Position on the target is given by $Y_{target} = m \cdot Z_{target}$. With these simple equations then:

$$c_{Y25} = \frac{d_{vertical}[\text{mm}]}{Y_{target}} \tag{4.5}$$

c_{Y25} indicates the scaling factor of the monitor. With these values the Analysis program compute the correct beam position, and from that the incident angles in the x, y directions, which are needed later for the analysis.

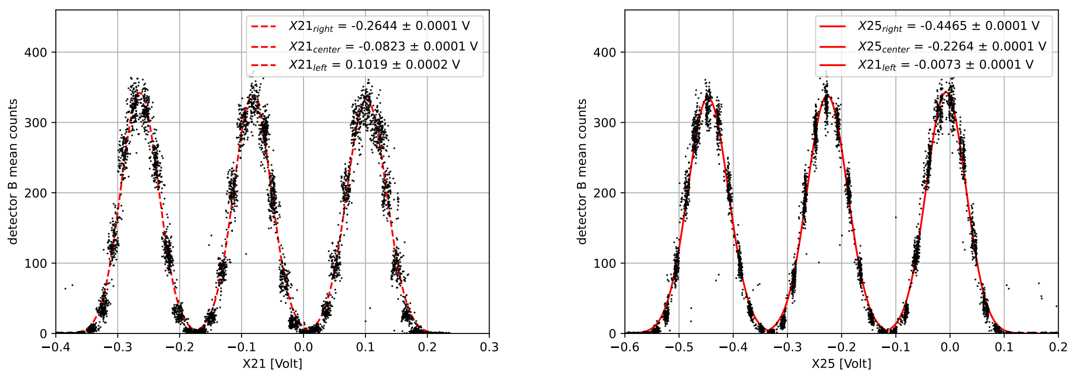

(a) (b)

Figure 4.4: Plot of the averaged count of detector B, with the slow variations of the beam position in the horizontal direction. The three peaks occur when the beam is aligned with the center of the wire. The values on the X axis are in V

All this procedure can be checked if we plot now the X and Y position for the same two runs of data acquired with the wires. After placing the scaling factors obtained in the standard configuration file, we run the analysis another time and the physical values were computed 4.5

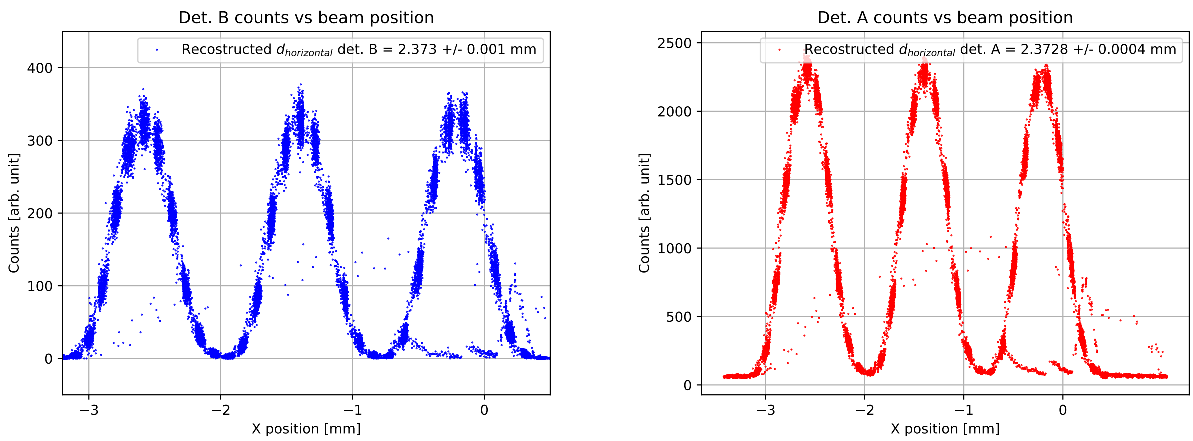

Figure 4.5: plot of the PMT Count against the physical values computed by the analysis program. Now the position of the three peaks correspond to the expected values measured for the target.

4.3.3 Current (PIMO) and Energy Monitor (ENMO) calibration.

The last two calibration needed for the analysis are about the energy and the current intensity of the beam, which are indicated with PIMO (current monitor) and ENMO (energy monitor). The values that we measure are given by VFCs counts. We remind the reader how the VFCs monitors operate: the input signal from the beam is transformed in a pulse wave whose frequency is proportional to the input voltage. The signal is so proportional to various quantities that we want to measure, however we need to determine the correct scaling factor and possible offsets to conver these quantities in physical units ready for the analysis. For this beam time the current is measured in µA and the beam energy is given in eV.

For the current monitors I13 and I21, the raw counts are converted in digitalized voltage values with the formula shown in (3.11). The relation between these values given in V and the real values in µA and eV is linear:

$$I(\mu\text{A}) = mI(\text{V}) + q$$

To determine the two coefficients, the beam current was raised from 10 µA to 22 µA in several step. For each step we confront the nominal values of the current with the values in V measured. The following plot show the procedure described:

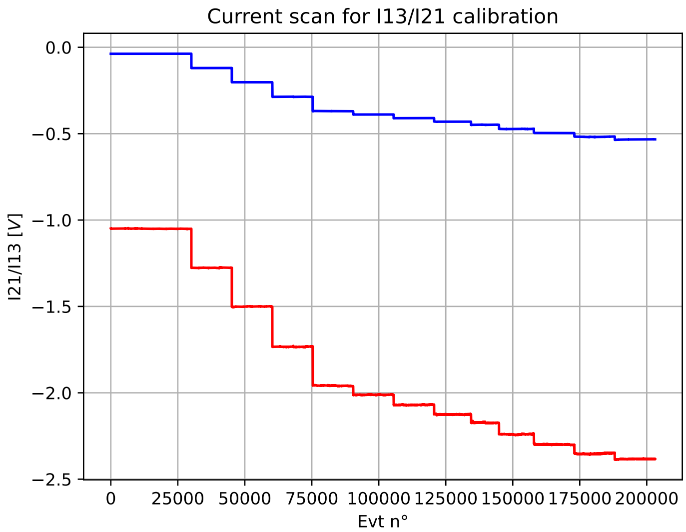

Figure 4.6: Current scan for the calibration, each step correspond to a run with a different beam current.

The calibrations consist in retrieving m and q with a linear fit. Then the parameters are added in the standard configuration file, together with the other calibration parameters, and can be loaded by the analysis program to process the data.

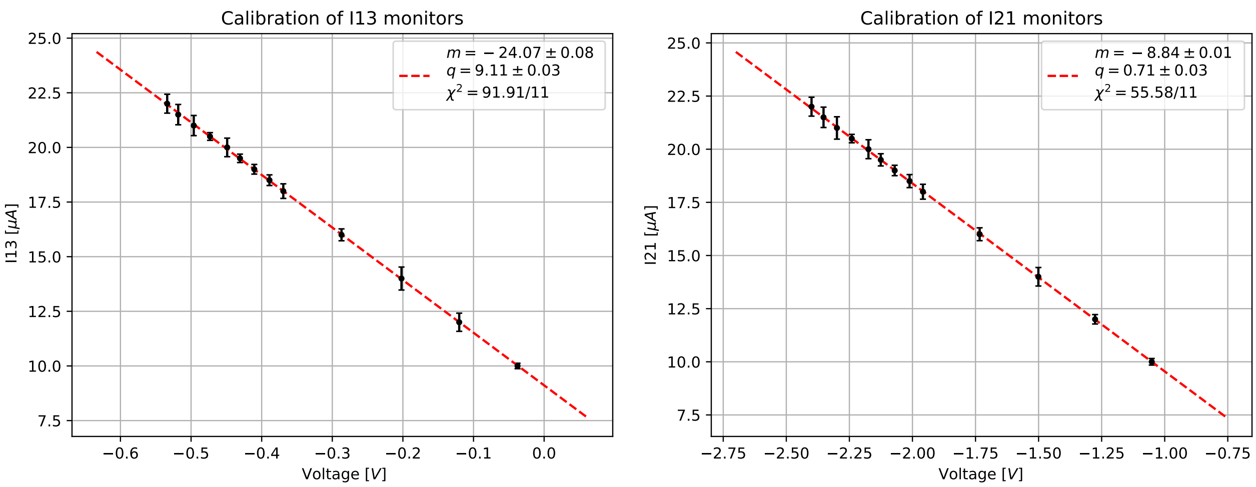

Figure 4.7: Calibrations plots for PIMO I21 and PIMO I13, the errors are multiplied by 25.

The values obtained from the fit of nominal beam current vs. voltage values are shown in the figure 4.7. The χ^2 values are higher than the expected. This is not unexpected, the errors in both the plots are computed with the sampling standard deviation formula applied to the sequence of voltage values $I21I13$ (σ_{vfc}, the standard deviation computed for each step in 4.6), and it is related to precision of the analog to digital converter VFCs. The errors are then propagated to the y axis showed in the plot. Yet, we are underestimating the error associated with nominal current I, in fact the accuracy associated with the beam current, set by the accelerator operators, was not disclosed, and we suspect that is not negligible compared to σ_{vfc}.

The ENMO calibration is performed in a different way from the other monitors. The energy calibrations is made with a particular procedure that is automatically made by MAMI operators, and exploit the polarity signal which controls the beam polarization at the source of the acceleration. Mami operators use the signal to create artificially a difference in the beam energy that is correlated to the beam polarity. This difference is equal (nominal) to 22,6 keV, and consist in the last two sub-events with higher energy respect to the first two. Because we know the nominal difference, the calibration consist in computing the correct scaling factor which convert from V to keV. The quantity that is relevant for the calibration is δE (with E_{18} being the energy monitor):

$$\delta E = \frac{E_{18}[3] + E_{18}[3]}{2} - \frac{E_{18}[0] + E_{18}[1]}{2}$$

An histogram of δE should show a single peak whose values correspond to 22,6 keV. For this calibration, we took 3 different acquisition, which differ for the different values of the beam current. We remind that the output voltage signal from the XY monitor is proportional to the current, as mentioned in 3.9, so we have that:

$$U[\mathrm{V}] = \frac{1}{C_{E18}} \cdot i \cdot E \tag{4.6}$$

So, if we invert the relation we have that:

$$\frac{E}{U} = C_{E18} \cdot \frac{1}{i} \qquad C_{18} = \frac{E}{U} \cdot i \tag{4.7}$$

And we have the scaling factor.

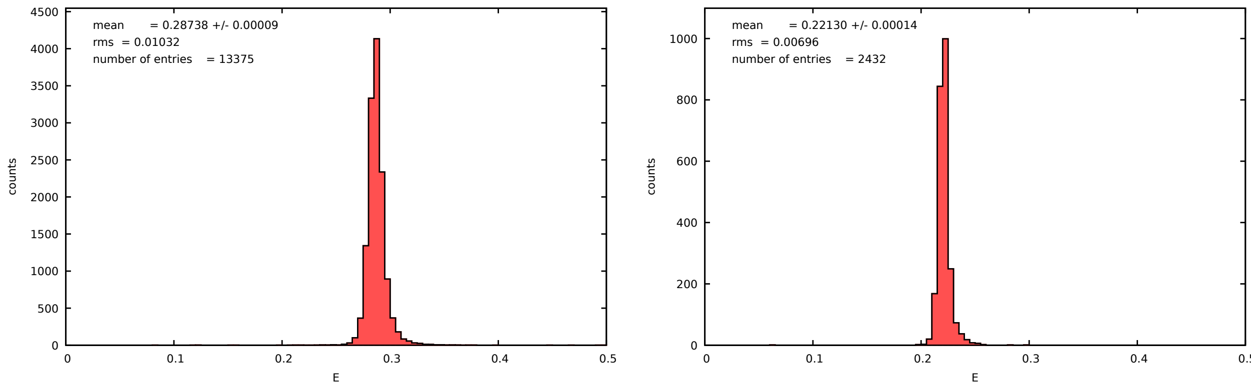

Figure 4.8: Histograms or δE with the beam current 20 µA on the left and 15 µA on the right.

C_{E18} is obtained taking the coefficient parameter m from the fit and substituting in:

$$C_{E18} = \frac{22{,}6\,\mathrm{keV}}{m}$$

From this we obtain the value $C_{E18} = +1595.2$ necessary to convert from Voltage units to keV. Using the value, we can show an histogram of δE in physical units, as a check of our procedure:

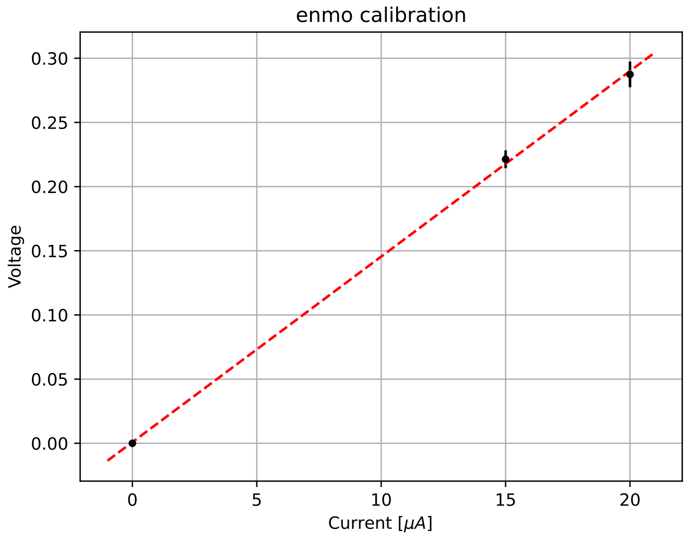

Figure 4.9: Calibration of ENMO monitor, plot of the ENMO voltage values versus the current.

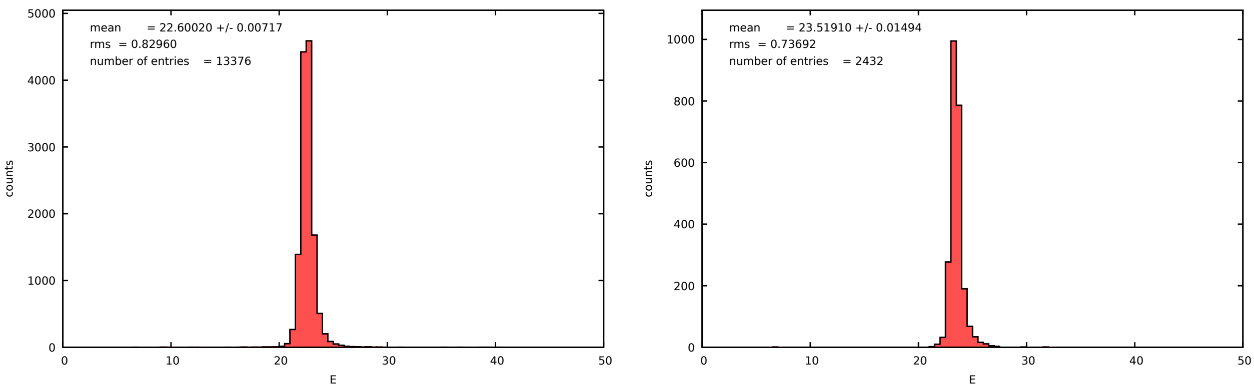

Figure 4.10: Plot for the physical quantities computed in the data tree, for two different current of the beam (on the left 20 µA, 15 µA on the right)

4.3.4 Calibration of the PMTs

During the beam time, several scans in attenuation were performed, before switching MAMI to produce the polarized beam, to choose the best working point for the PMTS of the detectors. The same procedure used in the laboratory was followed, so with a beam intensity of 10 µA we acquire data run one minute long, increasing each time the attenuation.

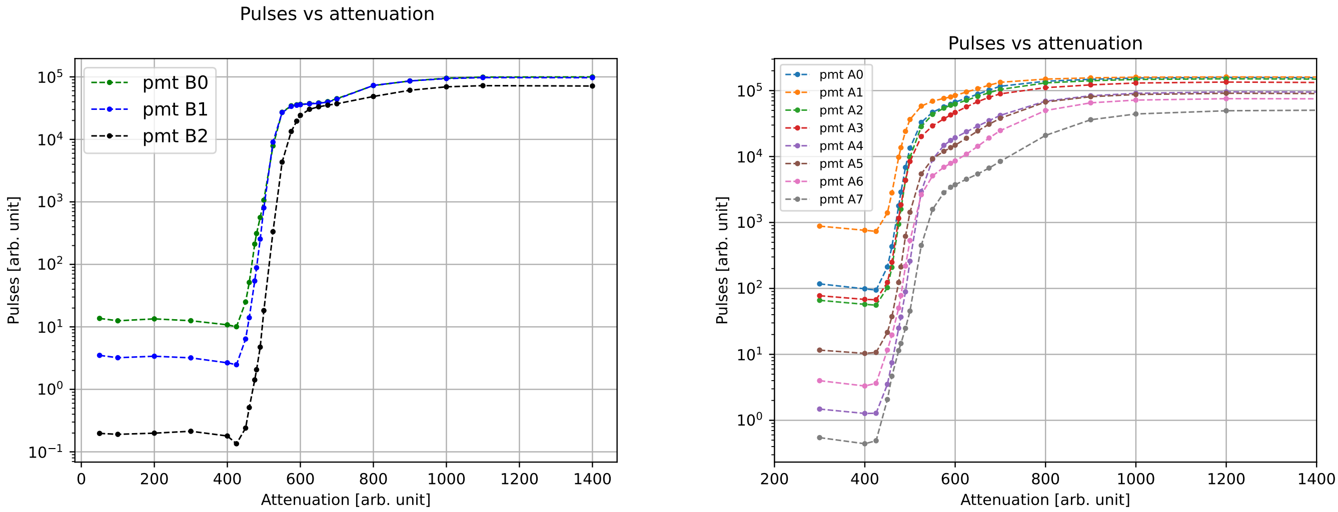

(a) *Attenuation scan for the PMTs of detector B* (b) *Attenuation scan for the PMTs of detector B*

From the fit we obtain three valus for the signal Peak, given in attenuaton units. We can check the idea behind this, visualizing the PMT count in a different way. Because we would like to visualize the number of electrons that generate a certain signal in the detector, we can think of differentiating the data showed in the plot 4.11a. The differentiation consist in the difference between the Counts at a certain point and the previous one, and dividing by the increment in attenuation:

$$Spectra = \frac{N(att_i) - N(att_{i-1})}{att_i - att_{i-1}}$$

In this way we compute a discrete derivative of the plot showed in 4.11a, which represent $\frac{\partial N}{\partial att}$. This is, in fact, the spectra of the signal, still given in attenuation units 4.11a. This plot are used to identify a good point to select the attenuation values. If we look at the plots 4.1a, we can see that the physical threshold does not scale linearly with changing the attenuation value, and for high values of attenuation, the threshold falls quickly at zero. Looking at the signal spectra, we identify the first peak as the electron signal. The other peak, for higher attenuation values (on the right), correspond to very low threshold values, and it is identified as the background noise. We selected the values of the attenuation between the peaks of the two distributions, maximizing the signal acceptance and trying to reject the background as much as possible. Our discussion so far is sufficient to carry out the calibration of the PMTs and take data to measure the asymmetry. However, we would like to identify the physical threshold in mV instead of attenuation unit. We can use the conversion function that we discussed in 4.1a:

$$f(att) = \frac{a}{(x-b)^3 + d}$$

We point out that the parameters of this function have been obtained from data that have not been acquired during this thesis work, moreover the threshold value in the program that controls the NINO board is slightly different (we always used 600, the data are taken with 750), therefore the values in volts need probably to be rescaled by some factor, but for our discussion we are interested in a raw estimation of the signal peak: With this conversion, we show the same plots in 4.11a, with the values in the x-axis in V now.

We know see clearly two peaks, the signal and the background, that are reversed respect to 4.11a.

We discuss now a simple model that we used to describe how the PMT Counts vary when we raise the attenuation. From 4.11a, we assume that the two peaks are described by two gaussian distributions. Now if

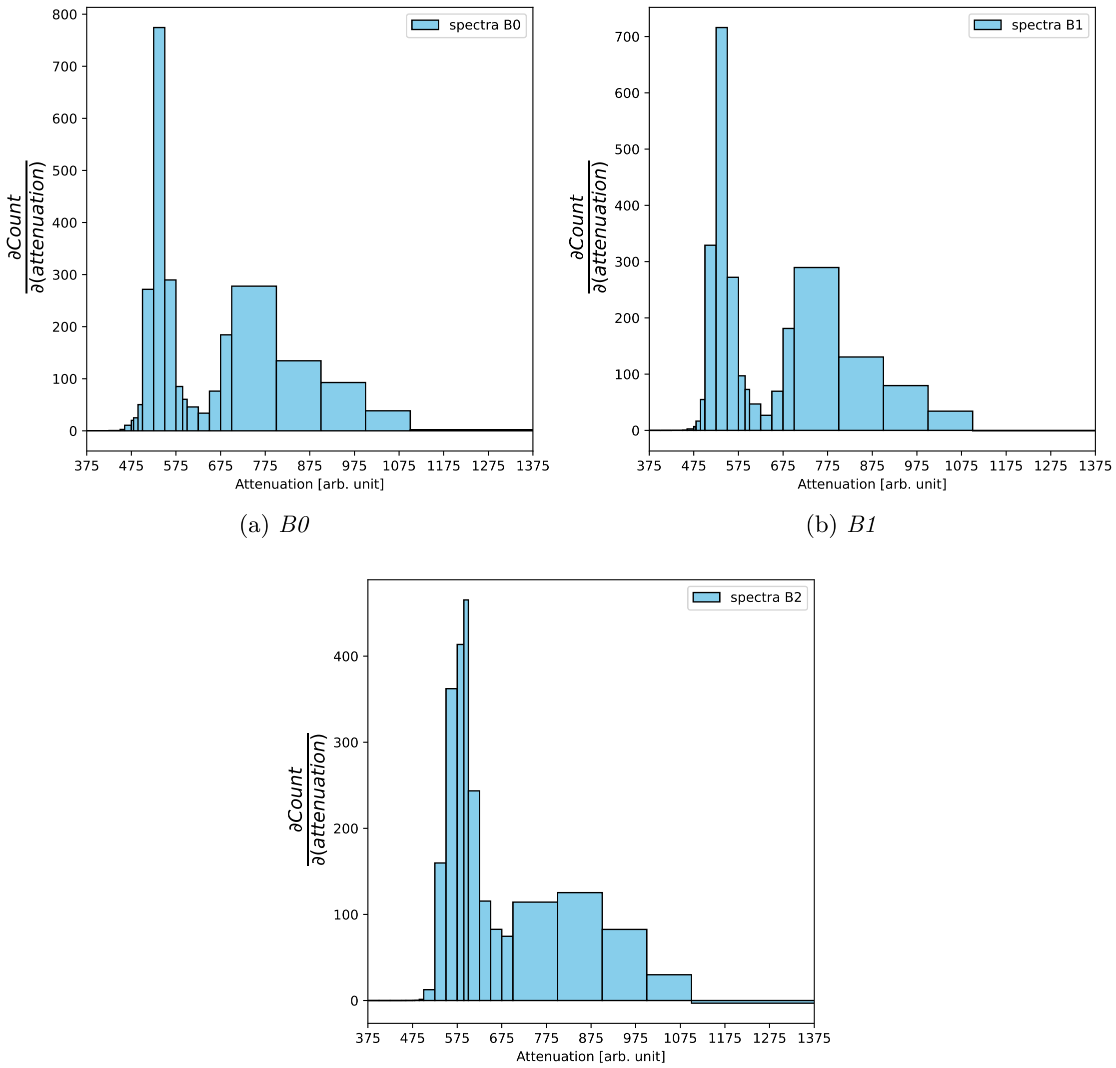

(a) *B0* (b) *B1* (c) *B2*

Figure 4.11: Reconstructed spectra for Detector B

we think about the the probability for a signal to pass the selection, this quantity is equal to the probability of being in below the attenuation value. Using now the fact that the probability are given by the cumulative of the gaussian distribution (probability of being in the right tail) it is straightforward to deduce:

$$P(signal > thr) = \Phi(x) = \frac{1 + Erf(\frac{x-\mu}{\sqrt{2}\sigma})}{2}$$

Considering that we have the sum of two gaussian distribution, we end with:

$$N(att) = \frac{n_1 + n_2}{2} + (\frac{n_1}{2})Erf(\frac{x-\mu_1}{\sqrt{2}\sigma_1}) + (\frac{n_2}{2})Erf(\frac{x-\mu_2}{\sqrt{2}\sigma_2}) \tag{4.8}$$

This model is used to fit the data. The result is shown in the following picture, the parameters obtained from the fit are reported below:

From these result we measure the mean μ_1 and μ_2 for the signal and the background given in attenuation units. The correct value of attenuation is set between the two observed peaks, in order to rejects the background and take only the signal coming from the scattered electrons. The same procedure was followed also for the detector A, the plots are not reported here, for brevity, but in the appendix.

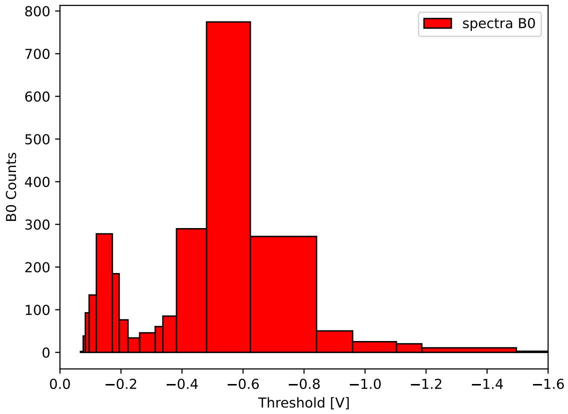

(a)

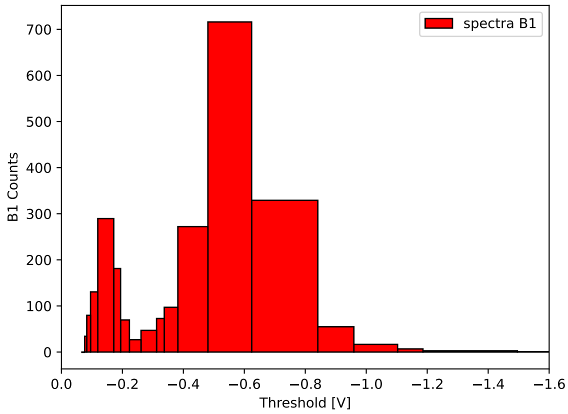

(b)

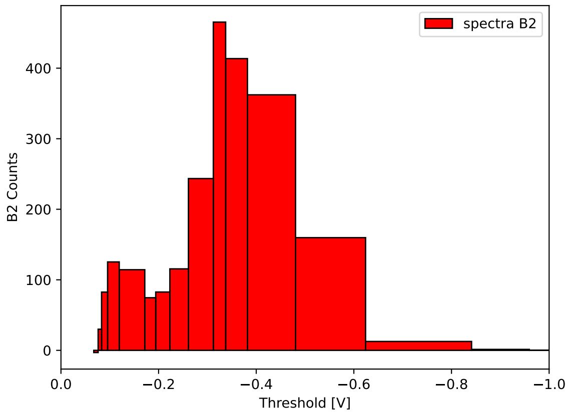

(c)

PMT	μ_1	σ_1	μ_2	σ_2	n1	n2
B0	538.0 +/- 1.3	19.4 +/- 1.1	798 +/- 8	103 +/- 4	34277 +/- 662	64244 +/- 1538
B1	536.4 +/- 0.9	18.2 +/- 0.7	783 +/- 5	89 +/- 2	34053 +/- 475	61636 +/- 1109
B2	582.8 +/- 1.2	25.9 +/- 1.0	824 +/- 8	88 +/- 6	32880 +/- 758	37930 +/- 1245

Table 4.1: Best fit result for the model defined in equation 4.8

4.3.5 Auto-calibration Procedure

In this section we present the last calibration tecniques needed in the data-process. The autocalibration is a special operation mode of the MAMI accelerator, during which the beam current is made to vary in a controlled way. Through these special runs is possible to obtain again the current scaling factor that we discussed in 4.3.3. Because the current in varying, it is possible to study the linearity of the PMTs. From a linear fit of the PMTs counts vs. current intensity the angular coefficient and the offset are measured. The offset is particual important because give rise of a possible systematic error that influence the final asymmetry result. It is quite simple to demostrate this, if a relation of the type $N = mI + N_0$ holds. Consider the following quantity:

$$\overline{N} = \frac{N_\uparrow + N_\downarrow}{2}$$

we can express $N_\uparrow$ and $N_\downarrow$ in this way:

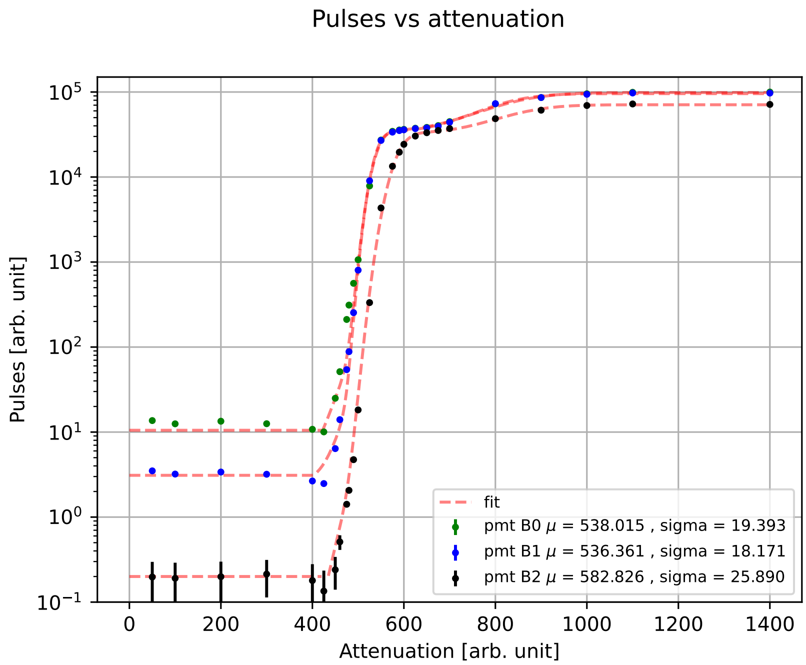

$$N_\uparrow = \overline{N} + A_n\overline{N}$$
$$N_\downarrow = \overline{N} - A_n\overline{N}$$

Now we suppose that $\overline{N}$ is linear dependent on the current in the way we defined above, so:

$$N_\uparrow = \overline{N} + A_n(mI) + N_0$$
$$N_\downarrow = \overline{N} - A_n(mI) + N_0$$

We are supposing that the offset N_0, we assume that the present offset does not contribute to the asymmetry, i.e. it is not correlated to the signal of the scattered electrons, but is due to processes of another type, therefore in the previous formulas only the mI counts must be multiplied by the asymmetry A_n. Therefore if we substitute everything in the definition of the transverse asymmetry:

$$A' = \frac{N_\uparrow - N\downarrow}{N_\uparrow + N\downarrow} = \frac{A_n(2mI)}{(2mI) + 2N_0} = A_n\frac{1}{1 + \frac{N_0}{mI}} \tag{4.9}$$

In the last passage we learn that the presence of an offset can decrease the recostructed asymmetry. So it's important to determine quantitatively N_0 and m in order to be able to take care of this effect. The strategy used is quite simple: every three hours of production data, we asked MAMI to start the auto-calibration program. With all the auto-calibration runs, we estimate N_0 for each PMT, separately. Then All this quantities are saved in a file so that the analysis program can retrieve the parameters and subtract them from the PMT counts. In this way every three hours the PMT are corrected, this take care also of the possibility that the the linearity of the PMTs can change after hours of use of the PMTs (for example it can decrease the efficiency).

During the autocalibration, the beam current is raised from 9 µA to 11,125 µA in step of 0,125 µA:

With a linear fit we can estimate the scale and the offset to convert from I21 voltage values to physical values of the current. The procedure in repeated for the 8 auto-calibration acquisition we had during the beam time, so we can also take care of possible variations during the time.

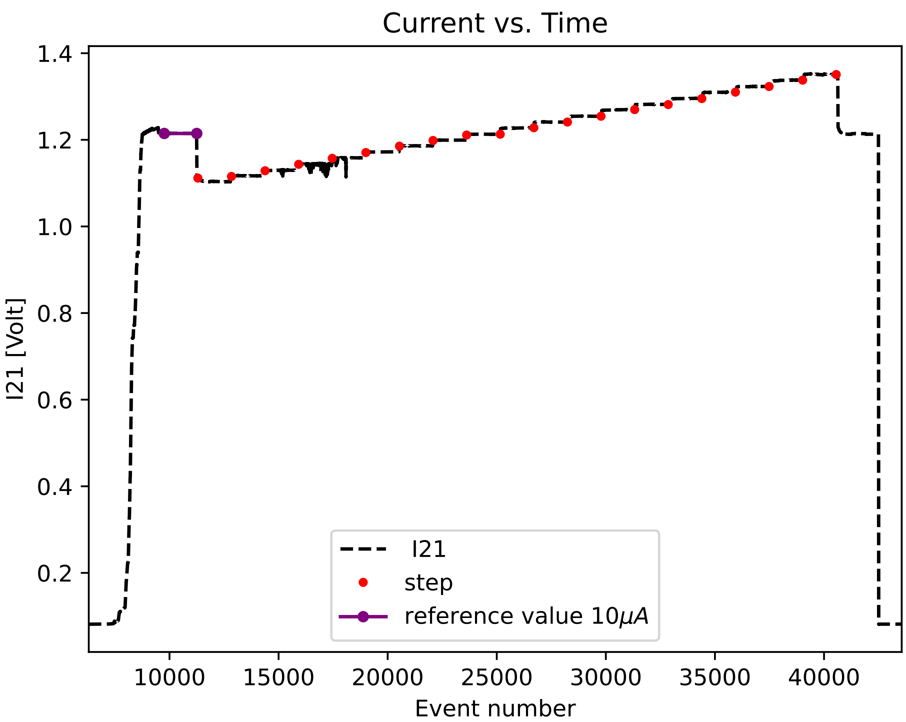

(a) *Autocalibration: in this plot we have the voltage value of I21 monitor. The current is first stabilized around* 10 µA*, then it is raised from* 9 µA *(the step lower down) to* 11,125 µA *in step of* 0,125 µA*.*

The figures are referred to the data acquired for the first auto-calibration. It's interesting to calculate, from the result of the fit, the factor that appears in 4.9:

PMT	m [μA^{-1}]	Offset	c
B0	1750	1301	0.93
B1	1742	1283	0.93
B2	1406	717	0.95
A0	6423	20385	0.75
A1	6756	29187	0.70
A2	6032	20513	0.75
A3	5218	12995	0.80
A4	3945	6666	0.86
A5	3967	6547	0.86
A6	3258	4655	0.87
A7	2325	2233	0.91

Table 4.2: Angular coefficient and offset obtained for the auto-calibration. The third column is contains the estimation of c, as defined in equation 4.9

Ignoring the presence of the offset lead two consequences: the recostructed asymmetry is lower, on average $\simeq 10\%$ less than expected, and the Counts are overstimated. Because the error depend on the PMT counts, as seen in 2.14, this two effect combined add up and worsen the precision and accuracy of the measurement.
The result reported in the table can be confronted with the final result that are reported in 6.

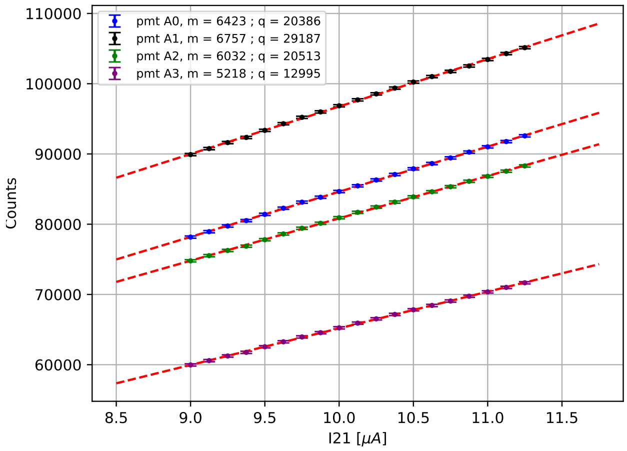

(a) *Current scan for detector A, the error are multiplied by a factor of* 20.

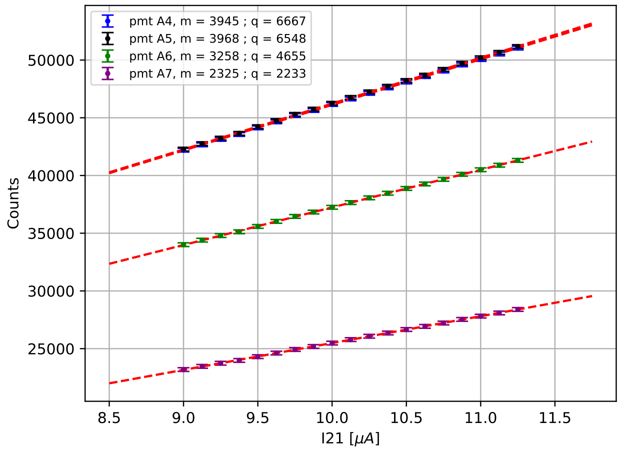

(b) *Current scan for detector A, the error are multiplied by a factor of* 20.

Figure 4.12: PMT Rates vs current (from I21 monitor), the model used for the fit: $y = mx + q$.

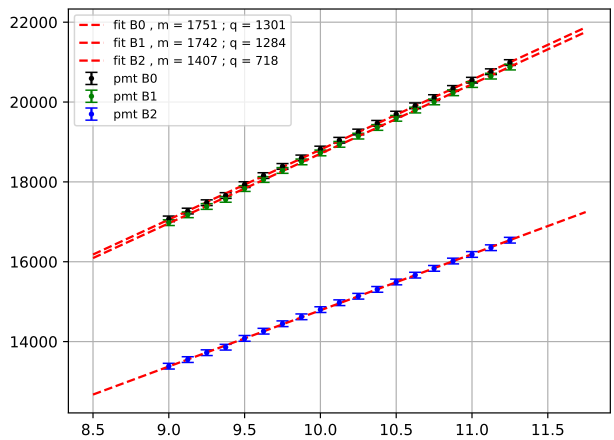

(a) *Current scan for detector B, the error are multiplied by a factor of* 20.

4.4 Data Tree Implementation

Referring to the next picture, we now discuss briefly the structure of the data that is implemented in the analysis program, this is important to clarify how data analysis will be developed:

The base class that is implemented in the analysis program is the *Event* class. As we mention above in 3.1, we do not intend to keep track of the single scattered electron, instead we analyze time series of 80 ms, in which we simply count all the electrons detected in this time interval. The work-flow of the analysis program is load the binary file collected during the beam time, parsing one event at a time and processing the raw-data from the beam monitors and the detectors. During the execution of the program data files in *.txt* are generated and filled with the processed data ready. The output data-file can be analyzed with any software package, such as root or python, to get the value of the asymmetry A_n. The picture shows that every event is divided into 4 sub-events. For each different sub-event a precise state of the polarization is defined, $+1$ for $S = \uparrow$ and -1 for $S = \downarrow$. Every sub-event is 20 ms long; during this time interval master-board receives all the data coming from the monitors and the detectors and sent them to the data-acquisition program (DAQ) that produces the binary-files, which are the input of the main analy sis program.

It is important to note that for each sub-event, a single measurement is acquired from the beam monitors,

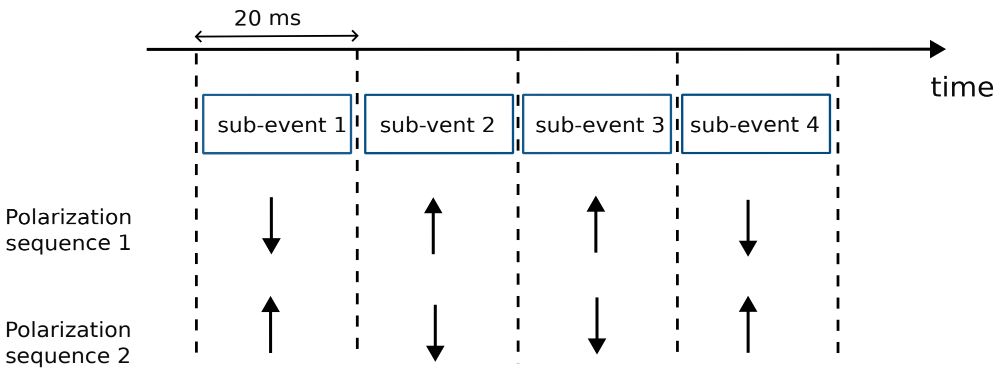

Figure 4.13

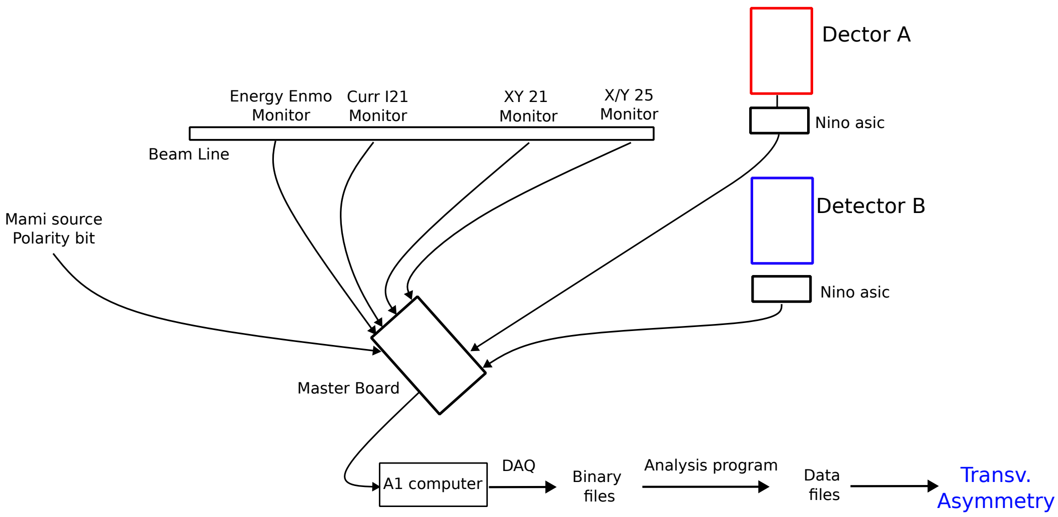

Figure 4.14: Scheme of the data flow.

which is intended as a time average of the various signals on the 20 milliseconds of sub-event duration. The sampling rate is then equal to 50 Hz. This structure of the data is quite specific. The main reason for this setup is connected with the need to avoid as much as possible that the variations of intensity, position and energy of the beams induce an effect that add to A_n. Considering only small time series, it is assumed that the beam is quite stable, in order to reduce undesired effects. Nevertheless, the contribution of these effects, which are indicated for brevity as false asymmetries, is considered in the final model. Several values are saved with the number of scattered electrons, for each event. The general structure of the data tree, with the important quantities, is reported here:

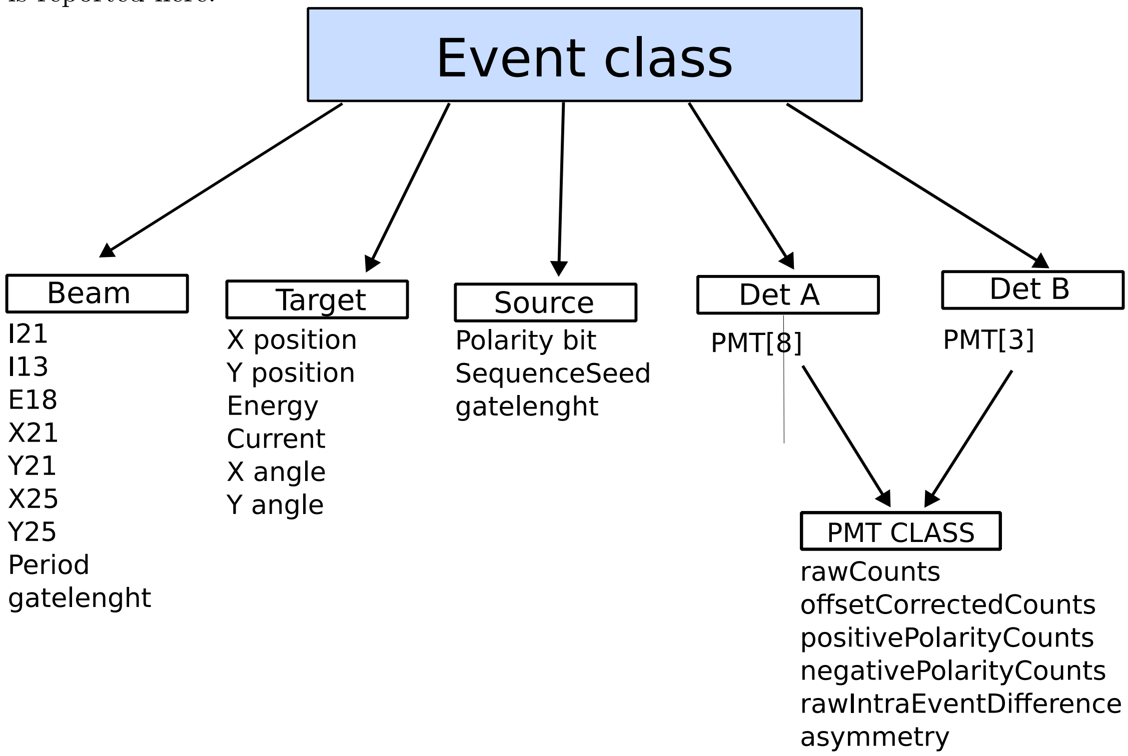

Figure 4.15: Scheme of the Event class, the structure of the data treen is shown here in a simplified version, for the complete reference see appendix.

The analysis program read the binaries files, convert from binary to decimal values and compute the beam parameters from the raw data of the monitors, filling the data tree shown in the figure. The Scheme above contains only the more relevant variables, and complete list is given in the appendix. We have 5 different classes, that are contained in the main *Event* class. The asymmetry values are stored in the two separated classes, *Det A* and *Det B*. The Analysis program read and analyze one event at a time, can produce also histograms for a fast visualization of the data, and generates the final output files in *txt* format for the data analysis.

Chapter 5

Asymmetry on Carbon and Rates on Lead target.

After having described all the calibrations needed, we are ready to analyze the data and measure the transverse asymmetryfrom the data collected in second part of the beam time. In this chapter we explain the procedure for the pre-selection of the data (for example the removal of the events with large variation of the beam parameters) and the procedure used to analyze the asymmetry of the two detectors in order to obtain, in the end, a point estimation of A_n. A section is dedicate to the measurement performed with lead target; through the knowledge of the expected counts per sub-event, we compute the amount of statistics needed to measure the transverse asymmetryon Pb with an accuracy of $1ppm$. In the end we discuss the problem of the false asymmetries that can affect the final result, using different method to calculate their contribution. The amount of data that are available corresponds to 23 hours of acquisitions, that are roughly 1 million of events.

5.1 Rates on Lead

After all the calibrations are done, we proceeded with the measurement of the rates on lead target, one of the objectives of the experiment. The lead target installed is a made by a thin layer with a thickness of 0,5 mm, and it's not isotopically pure. We took 14 acquisitions lasting $\simeq 2,5$ minutes, which corresponds to 6950 events. For each of these acquisitions we set the beam current at different values, ranging from 10 µA to 22 µA of intensity. The Rates are then reported as a function of the current, a linear model is used to fit the data.

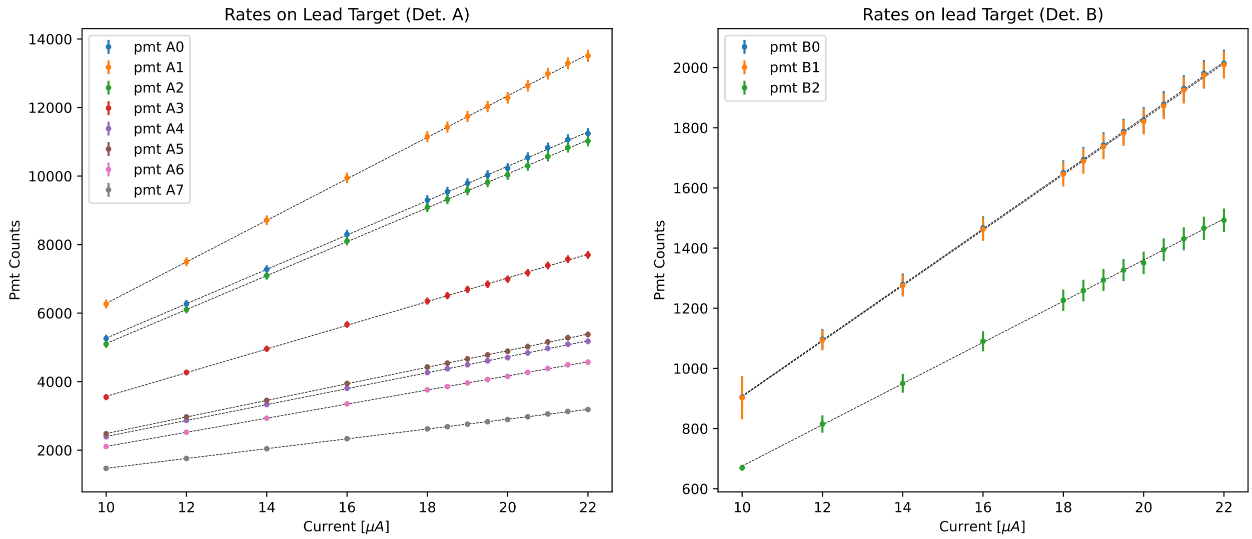

Figure 5.1: Rates on lead Target in function of the beam current. The Rates for each PMT of detector A (on the left), and detector B (on the right) are reported.

We fit using a linear model the data. The angular coefficient m and the offset q are reported in the table below for each PMTs of the two detectors.

The PMT Counts with this target, increase from 100 counts for detector B to 500 counts every 1 µA. It

PMT	m [µA]	q	χ^2 (dof = 9)
A0	501.42 +/- 2.17	256.55 +/- 39.57	13.7521
A1	605.77 +/- 2.31	226.11 +/- 42.04	13.3783
A2	495.01 +/- 1.47	163.04 +/- 26.83	6.95713
A3	345.68 +/- 1.6	113.4 +/- 29.16	12.1727
A4	232.58 +/- 0.9	74.38 +/- 16.44	5.36892
A5	241.95 +/- 0.74	65.79 +/- 13.51	3.48398
A6	205.79 +/- 0.65	52.38 +/- 11.87	3.0892
A7	143.42 +/- 0.47	36.49 +/- 8.55	2.26341
B0	92.55 +/- 0.34	-16.88 +/- 6.16	2.05286
B1	92.29 +/- 0.33	-16.9 +/- 5.97	1.92163
B2	68.48 +/- 0.32	-9.34 +/- 5.91	2.81988

Table 5.1: Lead rates, the values are measured for a target width of 0,5 mm.

is interesting to recover the formula of the experimental standard deviation σ associated to the asymmetry distribution:

$$\sigma = \sqrt{\frac{1}{2N \cdot n}} \tag{5.1}$$

We remind to the reader that N are the Counts per sub-event, while n is the number of event analyzed. Let's suppose that we want to obtain, for each PMTs, a statistical error not greater than $4,8ppm$. With this accuracy, the overall result A will have an error given by $\frac{4ppm}{\sqrt{8}} \simeq 1.7\,ppm$, while for detector B an overall result of $2.8\,ppm$. We computed the time needed to achieve this accuracy for both the two detectors, given in total hours of beam-time. This values are not casual: as we will see in the next part of this chapter, we managed to obtain this accuracy for the same measurement on carbon

current I	T [h] Det A	T [h] Det B
10	344	1487
12.5	277	1185
15	232	985
17.5	199	843
20	175	737

Table 5.2: Prevision of the time needed for the upcoming experiments to measure the transverse asymmetryfor Lead with an aimed precision of $1.7\,ppm$ for detector A and $2.8\,ppm$ for detector B.

The amount of time needed to obtain this accuracy with carbon is roughly $15h$ with 10 µA. The same measurement with lead will need 23 times the statistic accumulated for Carbon. This is due to the reason that the target thickness for lead target must be smaller than the target thickness for carbon. Because the atomic number of lead is greater than carbon, the amount of radiation during the experiment is exponentially higher. During the experiment, the A1 experimental hall is constantly monitored, the radiation level can not exceed a certain threshold. This imposes an important constrain to the maximum target thickness. As a consequence, despite the Mott cross section increases as Z^2 and favor heavy nuclei, the radiation levels dictates to work with lower beam currents and and smaller thicknesses for the target. But this is not the only experimental effort: we did not mention yet the problem of the low melting point of Pb. To avoid the target from melting, the beam current intensity must be controlled in order to reduce the amount of heat produced by the beam. For lead target a cooling system with a mixture of alcohol and water at $0°C$ degree is installed. In addiction to this, the beam position is continuously varied, following a Lissajous curve, in order to spread the beam hitting points. This is done using fast bending magnets, with a frequency much higher than the frequency of the polarization sequence, in order to avoid possible false asymmetry induced by the change in the positions. The combinations of all these factors makes the measurement with lead more challenging. However the A_n is valuable, in order to cancel possible systematics effect for the parity violating scattering, besides the fact that measurements made by PREX collaboration [4] do not agree with the theoretical prediction, suggesting the need to repeat the measurement independently.

5.2 Model for Fitting the Data

One of the problems of the measurement is to take into consideration the various contributions that can change the value of the asymmetry measured by the experimental apparatus. The raw values of the asymmetry can be affected by the variation of the beam parameters during the time. Let's summarize quickly all these effects:

- the PMTs counts can depend on the (x, y) impact position of the beam on the target
- the variations of the incident angles $\theta_x$and θ_y on the target.
- the uncertain associated with the energy of the Beam, a change in the energy associated with the polarization of the beam leads to different rates for the cross section
- the uncertain associated with the current of the Beam, in particular a change due to the efficiency of the source in producing electrons polarized in the two opposite directions

All this quantity, which we will indicate in general with δq can influence the asymmetry measured by the PMTs, considering also that the expected asymmetry is in the order of ten part per million, and small asymmetry introduced by fluctuations on the beam parameters are not negligible. Correcting directly the false asymmetries that rise from those uncertainties is a tough task, and it is more easy to adopt a different strategy respect to proceed to the analytical/numerical calculation of each of them . Knowing that the beam parameters produced by Mami are quite stable over the time, we can assume that the measured asymmetry are well described by a linear model as the following:

$$A_{tot} = A_{physical} \cdot P + \delta_I + A_x \delta x + A_y \delta y + A_{\theta_x} \delta\theta_x + A_{\theta_y} \delta\theta_y + A_E \delta E \tag{5.2}$$

$A_{physical}$ is the aim of the experiment, A_x and A_y are the asymmetries induced by the variation of the position of the beam, A_{θ_x} and A_{θ_y} are the asymmetry associated to angles, A_E is the asymmetry associated to the beam energy. The relevant assumption is that, for small variation of the beam, the false asymmetry are linearly dependent on the Beam uncertainties (that are $\delta x, \delta y, \delta\theta_x, \delta\theta_y, delta_E$), so a first order approximation seems valid.
We must clarify now what we mean with $\delta x, \delta y, \delta\theta_x, \delta\theta_y, delta_E$. Resuming the event structure, that we discussed in 3.1, we have a sequence of 4 different sub-events, with a polarization pattern that is randomly selected between $\uparrow,\downarrow,\downarrow,\uparrow$ and $\downarrow,\uparrow,\uparrow,\downarrow$. During the 20 ms of time length of each sub-event, the vfcs make a single measurement of the beam, and the data are saved in the data tree. The task of the analysis program is to use this raw data to calculate the relevant parameters for the analysis. Because we are working with asymmetries, the absolute values of the parameters listed above is not relevant, instead what is relevant are the differences correlated with polarization state of the beam. Assuming this, $\delta x, \delta y, \delta\theta_x, \delta\theta_y, delta_E$ are replaced with :

$$\begin{aligned}
\delta x &= \Big(\frac{X_\uparrow(1) + X_\uparrow(2)}{2}\Big) - \Big(\frac{X_\downarrow(1) + X_\downarrow(2)}{2}\Big) \\
\delta y &= \Big(\frac{Y_\uparrow(1) + Y_\uparrow(2)}{2}\Big) - \Big(\frac{Y_\downarrow(1) + Y_\downarrow(2)}{2}\Big) \\
\delta E &= \Big(\frac{E_\uparrow(1) + E_\uparrow(2)}{2}\Big) - \Big(\frac{E_\downarrow(1) + E_\downarrow(2)}{2}\Big) \\
\delta \theta_x &= \Big(\frac{\theta_{x,\uparrow}(1) + \theta_{x,\uparrow}(2)}{2}\Big) - \Big(\frac{\theta_{x,\downarrow}(1) + \theta_{x,\downarrow}(2)}{2}\Big) \\
\delta \theta_y &= \Big(\frac{\theta_{y,\uparrow}(1) + \theta_{y,\uparrow}(2)}{2}\Big) - \Big(\frac{\theta_{y,\downarrow}(1) + \theta_{y,\downarrow}(2)}{2}\Big)
\end{aligned} \tag{5.3}$$

Each δq represents the variation of one of the parameters of the beam within an event, so. One may wonder why the model doesn't contain a parameter A_I to describe the false asymmetry due to the current. We can show theoretically that the values of A_I is equal to 1. Starting from the definition of rate Γ:

$$\Gamma = \frac{dN}{dt} = I_0\, \sigma\, \frac{n_t}{S} \tag{5.4}$$

where I_0 is the beam current, n_t is the density of the target, and S is the surface of the beam. If we substitute everything in the definition of A:

$$A_I = \frac{\frac{dN_\uparrow}{dt} - \frac{dN_\downarrow}{dt}}{\frac{dN_\uparrow}{dt} + \frac{dN_\downarrow}{dt}} = \frac{\sigma_\uparrow I_{0\uparrow} - \sigma_\downarrow I_{0\downarrow}}{\sigma_\uparrow I_{0\uparrow} + \sigma_\downarrow I_{0\downarrow}} \tag{5.5}$$

It should be clear now that the current asymmetry A_I is equal to 1, and to take care of the contributions of the current we only need to compute δ_I:

$$A_{tot} = A_n + \frac{I_{0\uparrow} - I_{0\downarrow}}{I_{0\uparrow} + I_{0\downarrow}} = A_n + \delta_I$$

This is a direct consequence of the fact that the luminosity is proportional to the beam current, so we don't need to add a new parameter to the model.

5.3 Data Pre-selection and Fit

After all the calibration are performed, the analysis program is ready to produce the data-files suitable to analyze the asymmetry data for Carbon.
The Data file that are produced from the binary files are simply files in txt format, where the data are stored in columns. Before proceeding with the linear fit, however, it is necessary to visualize the data to check that there are no anomalous behaviors. In fact the data can contain moments of loss of the beam current and sudden interruptions, loss of polarization of the beam and even setting errors by MAMI operators can affect the experiment. Carbon data were taken from November 2nd to 4th, and consist of 28 runs, each 1 hour long.
The first step is to observe the PMT counts and the current trend, in order to be able to identify sudden interruptions of the beam, outliers and to check the behaviour. Here we show the trend over time for the series runs:

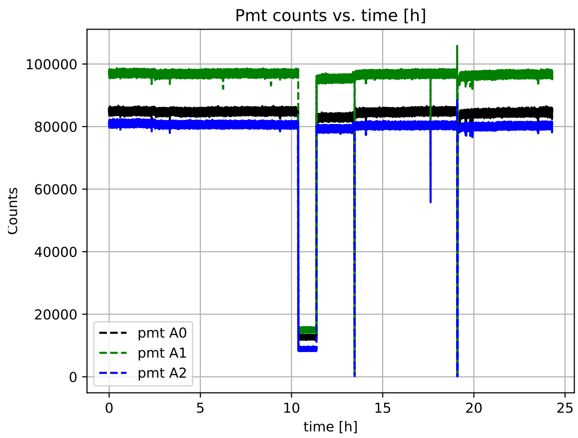

(a) *Counts vs. time, the plot represent the Count trend versus time, made for all the runs acquired during the beam time. The conversion from event number to time is made knowing that each event correspond to* 80 ms. *A total of 22 hours of beam was collected.*

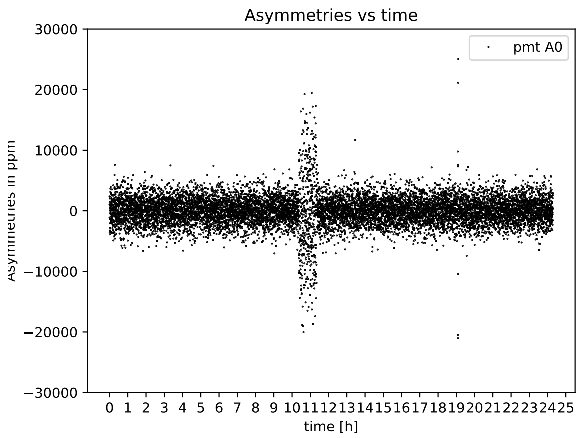

(b) *Asymmetry trend for PMT A0*

This plot show that after 10 h of data acquisition the PMT counts (5.2a) dropped rapidly. If we show the current trend over the time (5.2a) we do not see a corresponding decrease in beam intensity. Also the x, y position (5.2b) and the energy monitor of the beam do not show a strange behavior, so we reject the possibility that the beam was not properly aligned to the target.
We have the strong suspect that this issue come from a failure to be attributed to the NINO board. In fact for all the PMTs, during that time interval, the counts are equal to the offsets measured with the auto-calibration run. Our suspect is that the threshold and attenuation settings that are loaded during the initialization of the DAQ program were not set correctly. For the analysis, those data are rejected completely.

Apart from this, we observe in (4) sudden variations of the asymmetry around $13.5h$ and $19h$, that correspond to decreases in the plot on the left. We reject these data because we observe the same variation also for the current monitor, which means that the beam intensity fall quickly to 0 for a short period of time.

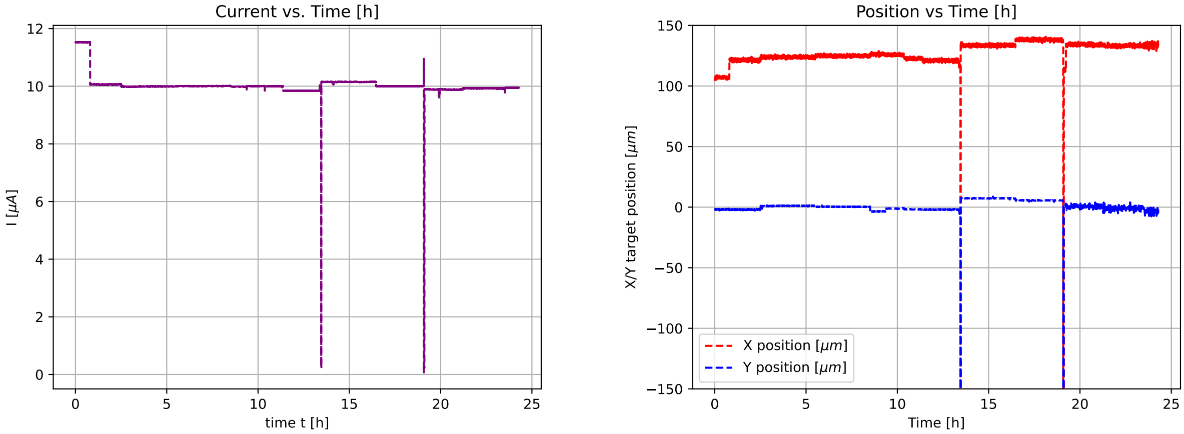

(a) *Current trend over time.* (b) X, Y *beam position over time*

Now we focus our attention on the correlated-difference values. We remind the reader that these quantities, that are used as independent variables for the fit, as explained before, are defined as

$$\delta x = \frac{(x_{up,1} + x_{up,2})}{2} - \frac{(x_{down,1} + x_{down,2})}{2}$$

and are calculated within each single event, to identify the differences with respect to the various quantities such as position, energy... which correspond to different states of polarization. Several histograms are produced (5.2a). These plots are useful to quantify the stabilization of the beam: we expect that all the correlated differences are distributed around zero, which implies that there is no systematic difference when the beam has one polarization state respect to the other. The mean μ and the standard deviation σ of the data are reported in the table (5.3)

Every histogram is generated with 100 bins. For the current correlated-difference, we find out that the values of the VFCs resistance, which controls V_{ref} value, was set to high. Because of this the precision of the monitor is low, compared to the other, and we observe isolated peaks in the plot. This indicated that for the incoming experiment we have to increase V_{ref} in order to to have a precision comparable to that of other monitors.

Table 5.3: Beam parameters:

	Beam Parameters: $X[\mu m]$	$Y[\mu m]$	$Xp[\mu rad]$	$Yp[\mu rad]$	$E[eV]$	$I[ppm]$
μ	$1.31 \cdot 10^{-3}$	$2.4 \cdot 10^{-4}$	$3.2 \cdot 10^{-8}$	$3.6 \cdot 10^{-9}$	0.0013	-1.23
sigma	$3.7 \cdot 10^{-1}$	$2.9 \cdot 10^{-2}$	$1.9 \cdot 10^{-5}$	$6.5 \cdot 10^{-6}$	0.38	50.4

Looking at the values of the mean and the corresponding error σ reported in the plots legend, we observe that mean of $X, Y, \theta_x, \theta_y, E$ are compatible with 0, except for the current correlated-difference, whose values reported already in *ppm* is significantly different from zero. These results are encouraging: we are not able to identify a systematic difference between polarization $+1$ and -1. A systematic difference would have produced a value μ shifted from zero, and a corresponding effect on A_n. With our assumption that the false asymmetries are well described by a linear model, observing that μ is small and compatible with zero for all the parameters, together with the evidence that δq are distributed symmetrical around zero, it could be stated that by averaging the asymmetries:

$$\overline{A} = A_n \cdot P + \overline{\delta_I} + \overline{\delta_x} A_x + \overline{\delta_y} A_y + \overline{\delta_{\theta_x}} A_{\theta_x} + \overline{\delta_{\theta_y}} A_{\theta_y} + \overline{\delta_E} A_E =$$
$$= A_n \cdot P + \overline{\delta_I} + A_x \cdot 0 + A_y \cdot 0 + A_{\theta_x} \cdot 0 + A_{\theta_y} \cdot 0 + A_E \cdot 0 = A_n \cdot P + \overline{\delta_I}$$

The contributions related to the false asymmetry should in principle cancel out. We will discuss later,

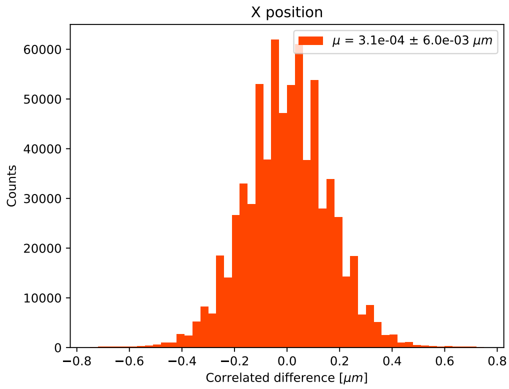

(a) *X position correlated difference*

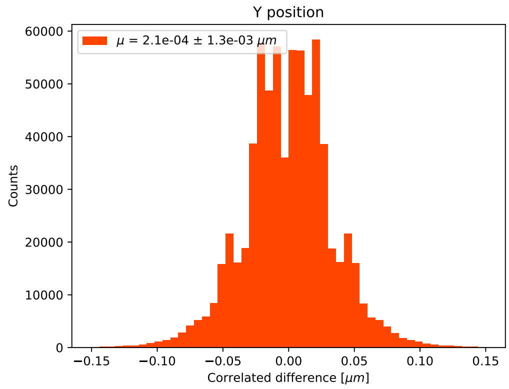

(b) *Y position correlated difference*

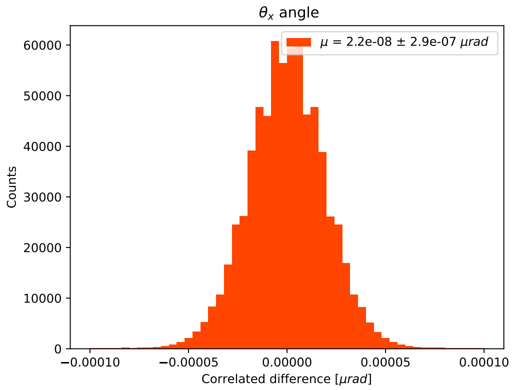

(c) θ_x *correlated difference*

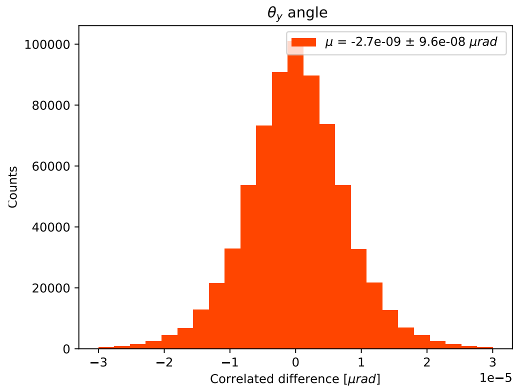

(d) θ_y *correlated difference*

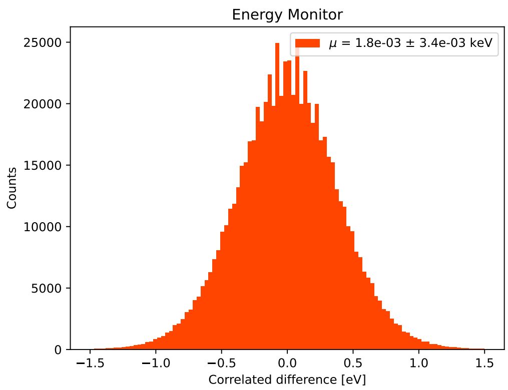

(e) *Energy correlated difference*

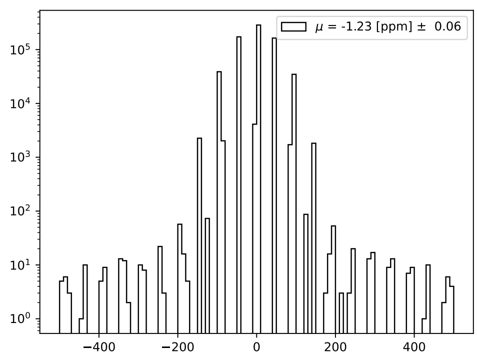

(f) *Current asymmetry*

when we will introduce the fit results, whether our assumption reflects the reality. We assume that the false asymmetry that has an effect is δI: $\overline{\delta I}$ is equal $-1.23\,ppm$, and we will subtract that to the final result:

$$A_n = \overline{A_{tot}} - \overline{\delta I}$$

After discussing the removal of the outliers, now will discuss in details the issue regarding the polarization of the Beam. To observe a transverse asymmetry, it is essential to have a correctly polarized beam. Unfortunately, we found out that part of the data where acquired with a Beam made by non-polarized electrons. The reason is that during the second night of the beam-time, MAMI operators that controls the quality of the beam switched from polarized beam to non-polarized, unintentionally. These wrong data were acquired during the night of 2nd December and we discovered this problem only the next day. We had no evidence of how many hours of beam were lost. Because this happened during the night, nobody could save the polarization measurement of the beam and identify the runs affected by this problem. This issue introduces a big systematic error that is potentially decreases the reconstructed A_n. It is important to identify the runs that share this problem, otherwise the measurements are affected by a bias that is not possible to disentangle from any other systematic effects related to the electronics system of the experiment, therefore also the electronic testing is not possible. All the stabilization monitors were active, so the data show apparently the same behaviour of the data with the correct polarization. We can't proceed with an arbitrary cut of the data, because there is the risk to cut off also good data or perform an incomplete removal. The next phase of the analysis is focused on describing a clear method used to identify the data and remove them from the analysis.

The procedure to identify the runs with 0% polarization rely to the estimation of the correlation coefficient of the PMTs counts. For every event we have two type of polarization sequence. The polarization $\vec{P}$ of each sub-event is identified with $+1$ and -1, that correspond to up and down $\overline{P}$. This values are part of the data tree, and form a sequence p_i of the type: $+1-1-1+1$, where i is the index to the i-th sub-events analyzed. If the $\overline{P}$ is different from zero, we expect, due to the transverse asymmetry, a difference in the number of scattered electrons between sub-events with different p_i.

sub-event	1	2	3	4	5	6	7	8
Polarity	+1	-1	-1	+1	+1	-1	-1	+1
PMT B0	101	99	98	102	100	99	97	103
PMT B..	...	...	...	...	...	...	...	...

Table 5.4: Example of the Polarity sequence and PMT counts that are saved in the analysis program. The values of the PMT counts given are for example.

This lead to a positive/negative correlation between the sequence p_i and the PMT data. In case of $\vec{P} = \vec{0}$, the expected values for the correlation should be zero.

We applied this strategy with the hope to identify and remove the block of data with $A_n \simeq 0$. The correlation c between the p_i and the PMT sequence N_i of counts is computed every $t = 1h$, that correspond to 45000 events. We plot the averaged correlation for detector A and B, and the correlation of the two detectors together (with the reverse sign for detector B).

The correlations coefficient c is clearly dependent on the $\vec{P}$. is we observe that c is compatible with zero, we have an evidence of the block of runs to be removed from the analysis. The values are reported in figure 5.2. The errors for each point are computed with the formula:

$$\sigma_c = \sqrt{\frac{1-c^2}{N-2}}$$

The plots show also the expected values for the c computed with a simple simulation, using the values of $A_n = 22.5ppm$ and $P = 0.79$ as an input. The simulation results are obtained following these steps:

- A sequence of the type $+1, -1, -1, +1$ is generated, long 45000 events.
- For each sub-event of the previous sequence, the PMT counts are generated: the counts are sampled from a gaussian distribution with μ and σ^2 equal to the values measured for both the detectors. To reproduce the correlation with the polarity sequence, the values are shifted accordingly by a factor $\mu \cdot A_n \cdot P$

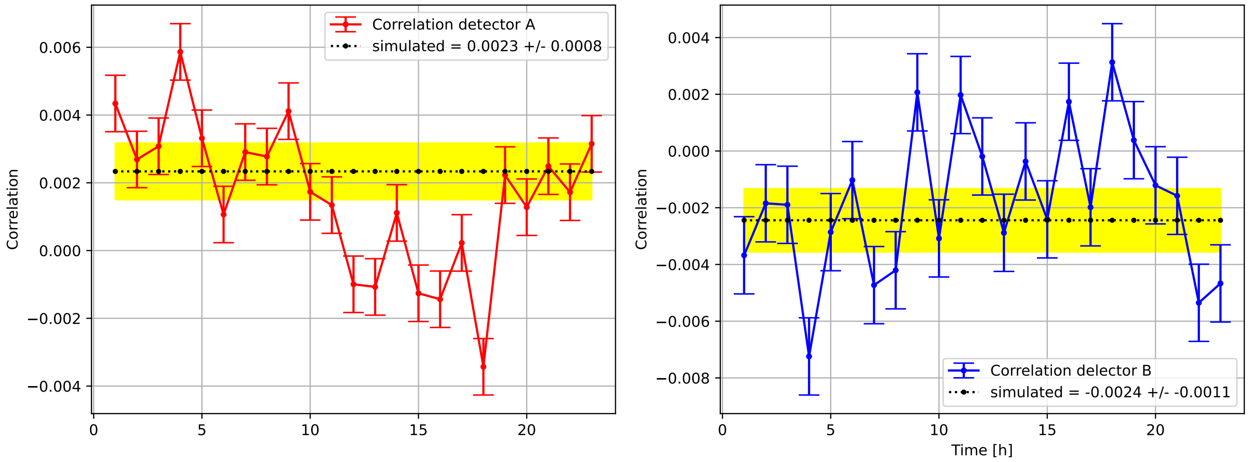

(a)

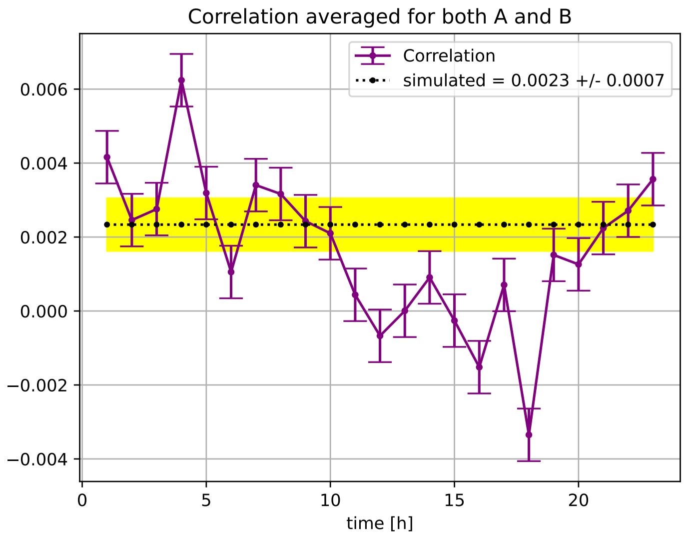

(b)

Figure 5.2: Plot of the correlation for detector A and on the left, and combining the two detectors results on the right. it is possible to identify a block of run starting at time $t = 12h$ until $t = 19h$ where the correlation is small and compatible with 0. The values can be confronted with the montecarlo, whose error band is in yellow.

- The previous step is repeated 25 times, and for each iteration we compute and save the correlation between the polarity sequences and the counts.
- From the values saved, we compute the mean c (the dotted line in plot 5.2) and σ_c.

Looking at the plots, we observe for detector A a block of runs where c is compatible with 0, in contrast with the values expected from the simulation. Due to the higher error, the corresponding plot for detector B is not clear to interpret, however the plot on the right with the overall results for A and B confirms the evidence for A. This let us to identify the block of runs that show a behaviour compatible with $\vec{P} = \vec{0}$. it is important to check that validity of this method seeing if the corresponding asymmetry is compatible with 0 5.3.

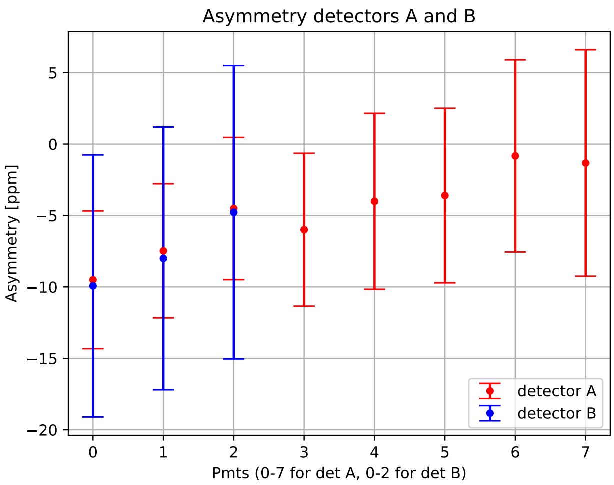

Figure 5.3: Raw-asymmetry computed for the block of runs with $P = 0$. Except for one PMT of detector A, all the values are compatible with 0 in 1σ.

The asymmetry values for this block of runs shows an unexpected behaviour. For both the two detectors we observe negative values. The weighted mean for the two detector is :

- $A_B = -7 \pm 5$ ppm
- $A_A = -5 \pm 2$ ppm

The values are not compatible with zero, but are compatible with each other. It is therefore reasonably certain that such data should not be included in the main analysis, because we observe a negative asymmetry for both the two detector is not compatible with the presence of a polarized beam.
At this point, it is interesting to study the distribution of the asymmetries measured by the two detectors. Our main assumption is that the asymmetries values are distributed following a normal distribution, around the physical value A_n. We have produced several histograms to show the PMTs asymmetries. For every histogram we use a gaussian function to fit the data, the reduced χ^2 is reported in the table below:

From the values obtained, we don't see a strong evidence to reject our hypothesis. The histograms are reported below:

We see a good agreement with the hypothesis of normal distributed data . The histograms for detector A are reported below:

Pmt	reduced χ^2
B0	1.2 ± 0.2
B1	0.9 ± 0.2
B2	1.23 ± 0.2
A0	1.2 ± 0.2
A1	0.7 ± 0.2
A2	0.7 ± 0.2
A3	0.9 ± 0.2
A4	1.4 ± 0.2
A5	0.7 ± 0.2
A6	1.1 ± 0.2
A7	1.7 ± 0.2

Table 5.5: Reduced χ^2 for the gaussian fit of the asymmetry data. The expected value is 1, the result are generally in agreement with the expected value.

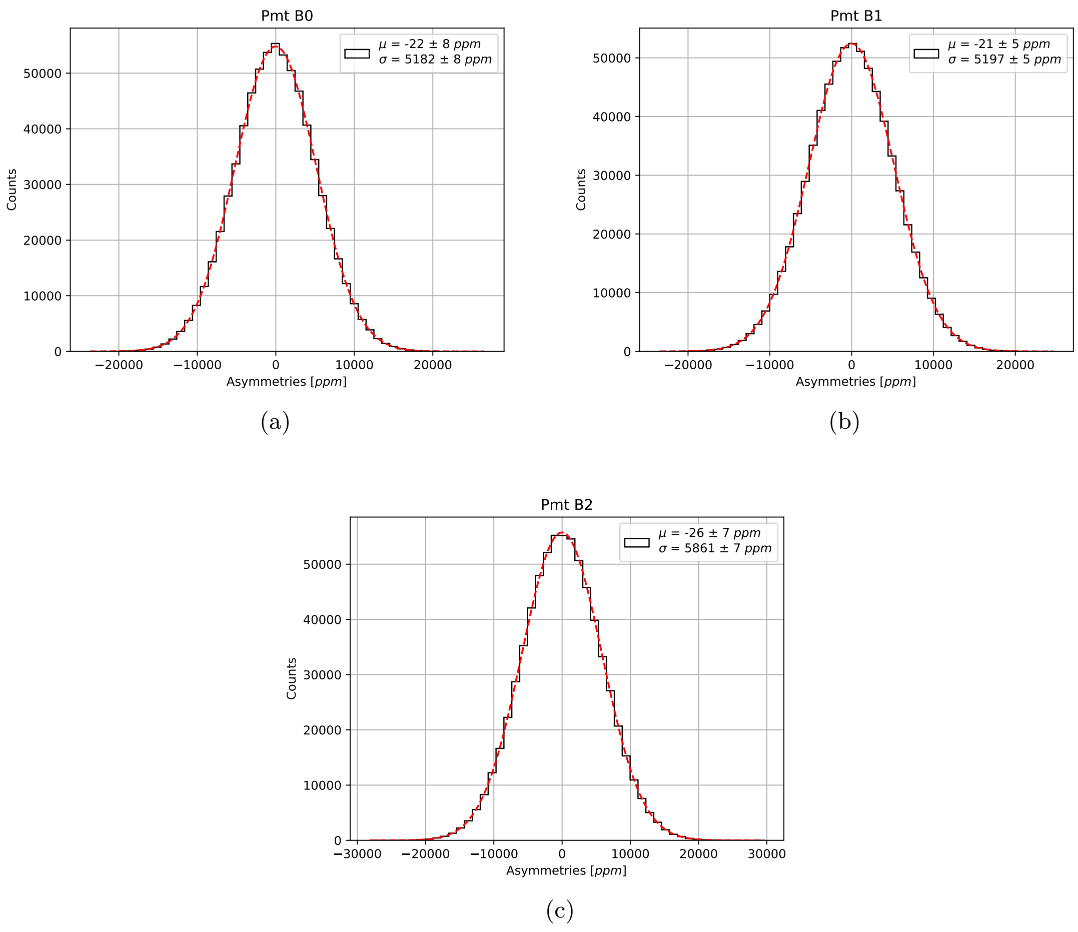

Figure 5.4: Histogram of the Asymmetry for Detector B.

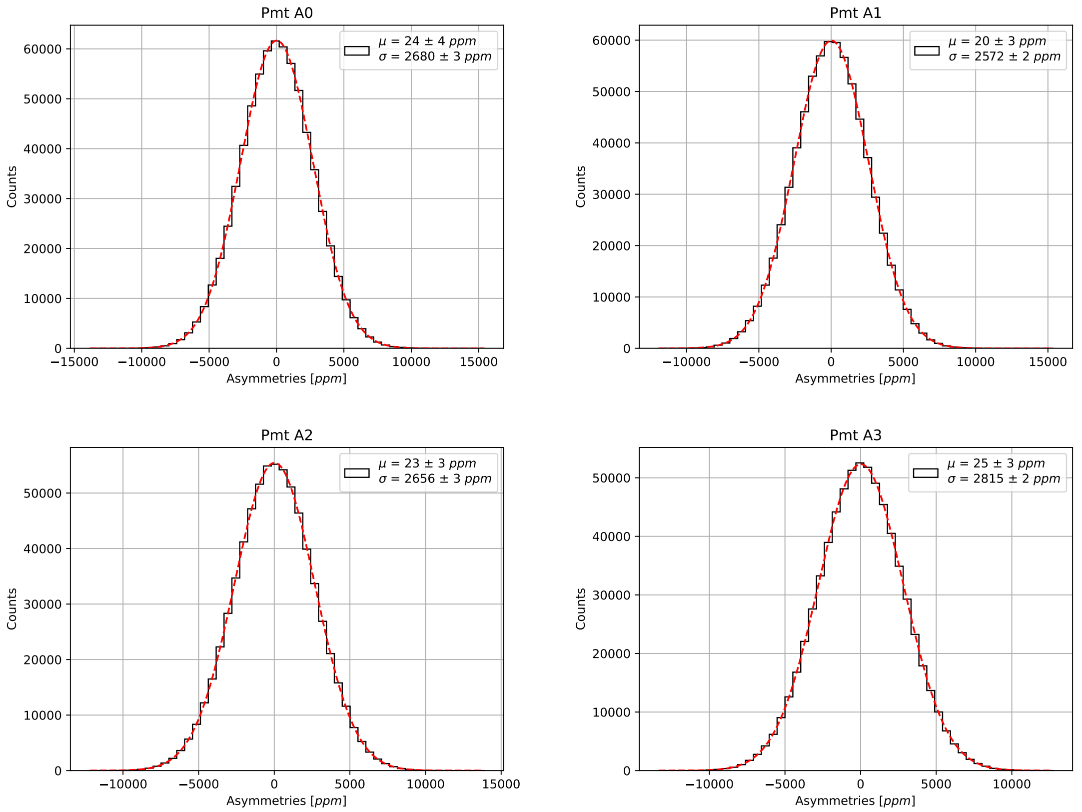

Figure 5.5: Histogram of the Asymmetry for Detector A.

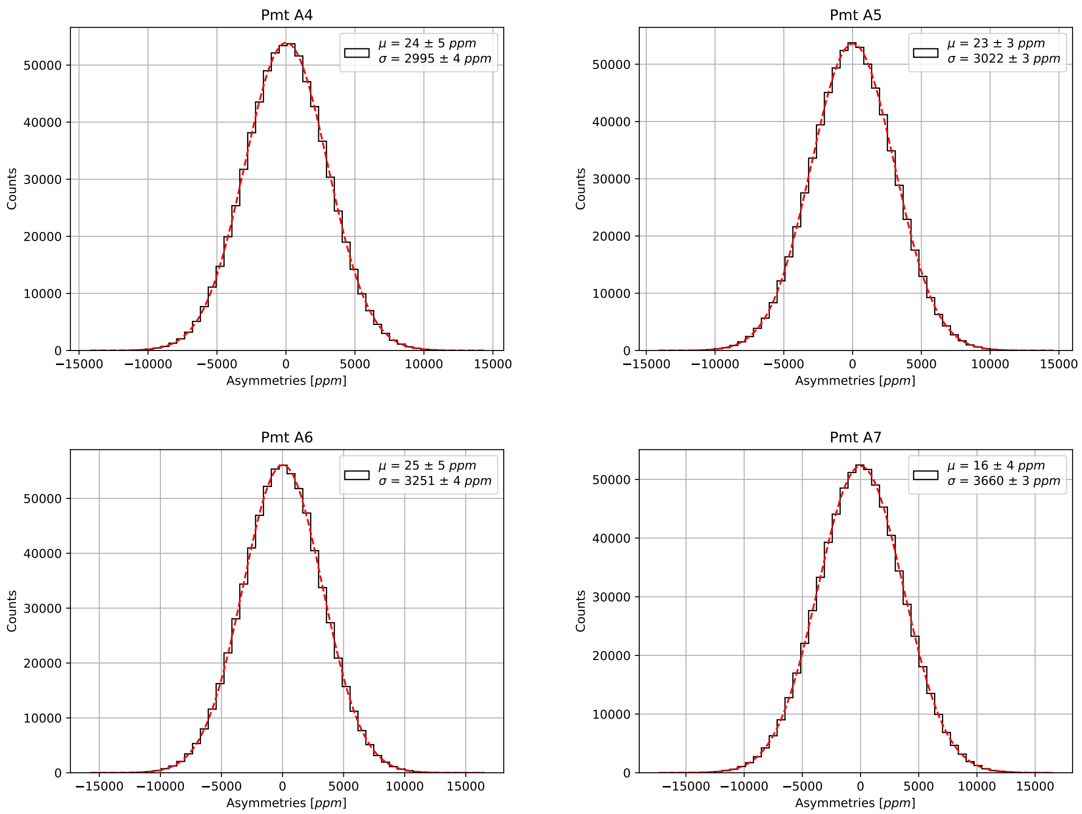

Figure 5.6: Histogram of the Asymmetry for Detector A.

5.3.1 Fit with a Linear Model

To retrieve the asymmetry A_n from the data, we assume a linear model where the asymmetries depend on the beam parameters, in the way we discussed before (5.2). The contributions due to variations of the beam within an events are described with 5 parameters, that are $A_x, A_y, A_{\theta_x}, A_{\theta_y}, A_E$. The data are analyzed both using python libraries, and with a fit program implemented in the framework of this thesis. To analyze the data with python, it is used the *curvefit* function implemented in the python library *scipy.* The fit program implements a well know algorithm used in linear regression: the ordinary least square algorithm (OLS). The OLS algorithm is basic algorithm, the easiest to implement and robust. It relies on few important hypothesis about the characteristics of the data. In principle we could handle all the analysis relying entirely on python. The decision to implements a fit program by ourself is due to the fact that in this way we interface directly to the analysis program, that is written in *c++* code. the assumption underlying linear regression is that there is a relation between the data of this type:

$$y = \vec{x} \cdot \vec{\beta} + \epsilon \tag{5.6}$$

$\vec{x}$ are the independent variables, $\vec{\beta}$ are the parameters and ϵ is a noise, that is supposed to be gaussian distributed (however, the robustness of the OLS algorithm let to relax this request). Another important assumption is that the linear variables are not correlated. This last request is particularly important, as related data cannot be processed with either of the two algorithms used. Before proceeding with the fit, it is necessary to verify this assumption. The first step so is to compute the correlation matrix for the beam parameters, we report in a table the values obtained:

	X	Y	θ_x	θ_y	E	I
X	1	-0.02	-0.99	0.06	0.04	-0.03
Y	-0.02	1	0.01	-0.65	0.01	-0.02
θ_x	-0.99	0.006	1	-0.005	-0.05	0.03
θ_y	0.06	-0.65	-0.05	1	-0.003	0.03
E	0.04	0.005	-0.05	-0.003	1	0.26
I	-0.03	-0.02	0.03	0.03	0.26	1

it is immediate to observe that for $(\theta_x, X); (\theta_y, Y)$ the values for the correlation are high compared to the other parameters.

The plots confirm the linear dependence between those parameters. With this evidence, it is clear that the have to modify the model to fit the data. We decided to include as linear independent variables only : I, X, Y, E.

Before proceeding with the fit, it is interesting to study how A_n evolves with the increase of the data. What we intend is to plot the averaged values $\overline{A_n}$ as the number of data increases, where the average is made on all data collected from time $t = 0$ up to time $t = t_1$ (5.7).

These plots are useful to check that the asymmetries converge to a certain value, and that there are no steepy variations that could be related to the presence of remaining outliers. Besides this we observe that the sign of the asymmetries for the two detectors are opposite, in agreement with what we expect from the different kinematic. In fact the sign of the asymmetry is given by the sign of the cross product $\vec{k} \times \vec{k'}$. For detector A the cross product has a positive module, while for the detector B it is negative. For a better visualization of the data, especially to observe the dependence of the asymmetry on the Beam parameters measured, it is useful to plot A versus each of the beam parameters. Unfortunately, the statistical error associated to the asymmetry is too high to appreciate whether there is a linear dependence in the data. For example here we plot the asymmetries A versus X.

The statistical error associated to A is too high to identify a trend in the values. A different approach is to divide the X axis in small interval, like the procedure of binning, and average all the asymmetries that fall in the same interval. This reduce the amount of data, but decrease the statistical fluctuations. For a plot of this type each point represents the overall asymmetry for a particular interval of X ,Y and E.

We report for brevity only the values for pmt A0 of detector A. In this case is is more simple to identify the presence of a linear dependence in the data. The errors are computed with the formula defined in equation 2.14, considering each interval separately. Another approach that we can use to further reduce the fluctuations due to the high statistical error of A_n is to do an additional average for all the PMTs of each detector. This

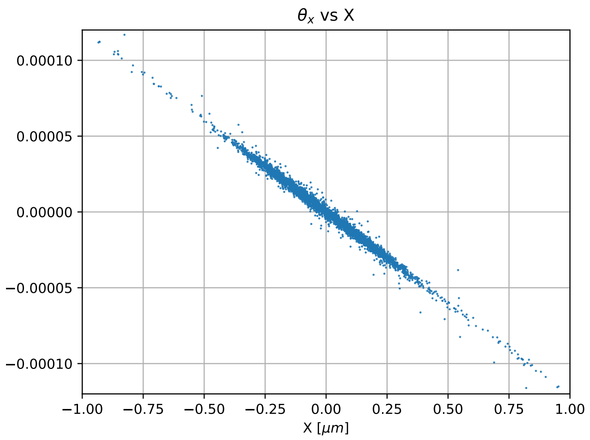

(a)

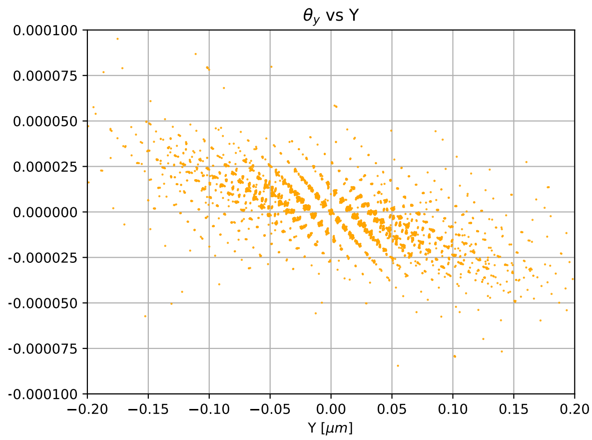

(b)

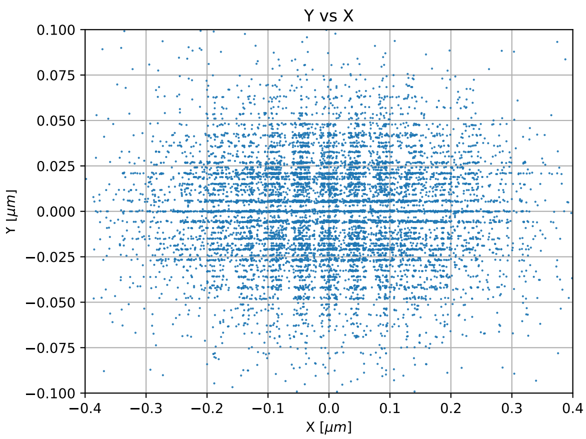

(c)

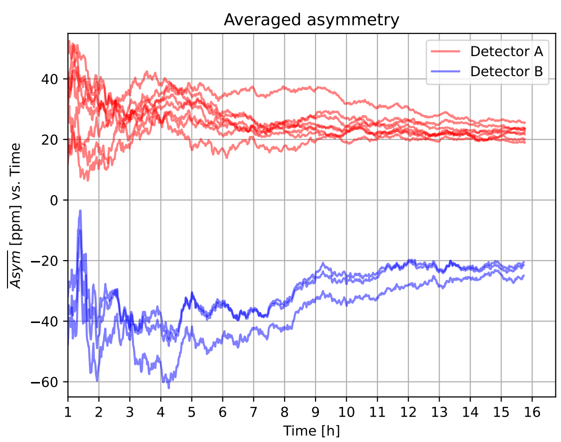

(a) *Averaged asymmetries for each PMT.*

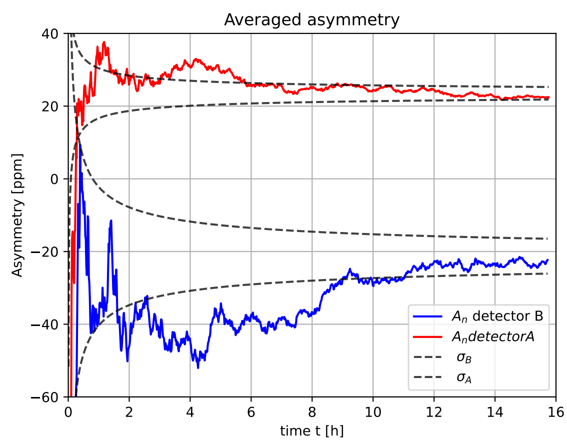

(b) *Averaged asymmetry for detector A and B. The dotted line correspond to* 1σ *error.*

Figure 5.7: Plot of the Asymmetry versus time. The plot show the average over all the events collected from $t = 0$ to $t = t_1$. Each line represents A_n measured for PMT (in blue detector B and in red detector A). The values are corrected for the beam polarization, multiplying by $\frac{1}{p}$. No further correction is applied.

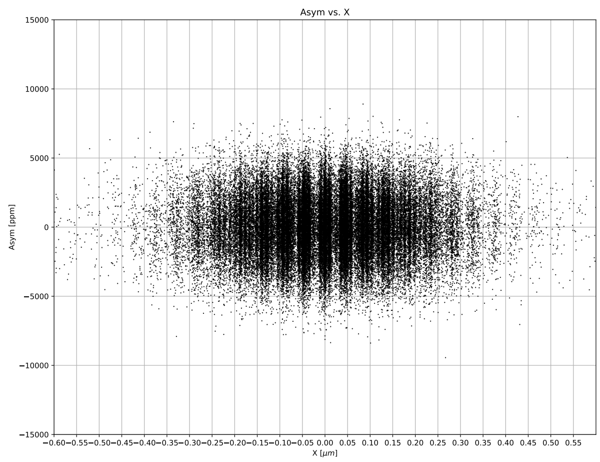

Figure 5.8: PMT A0 asymmetries versus X beam position. Because of the statistical uncertainties, it is not possible to visualize a linear dependence in the data.

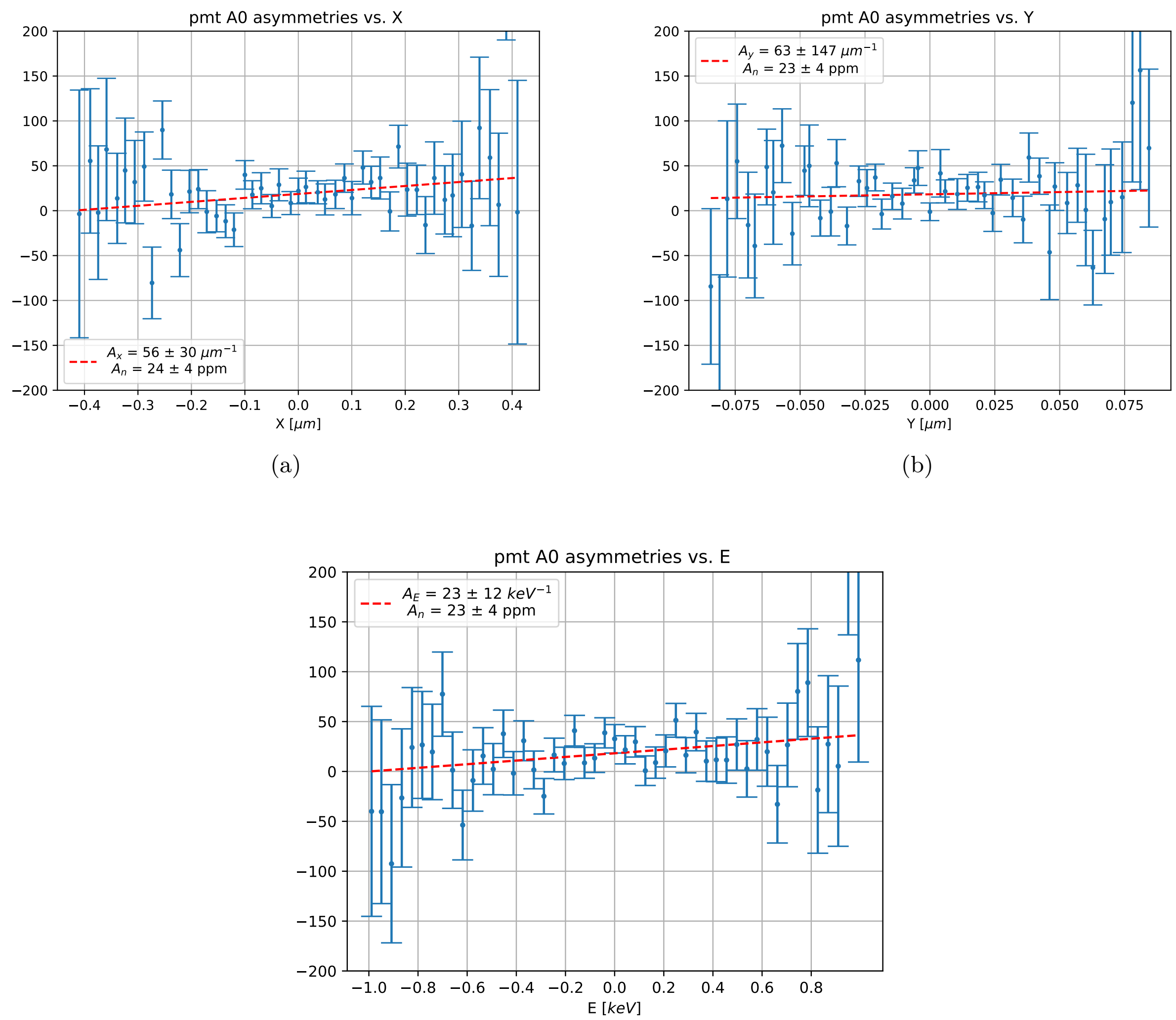

(a) (b)

(c)

Figure 5.9: A versus δx, δy and δE. The plot are generated with 50 equally spaced bins. The red line is the best fit with a linear model.

procedure decrease the error of a factor $\sqrt{8}$ for detector A and $\sqrt{3}$ for detector B. However, this procedure doesn't take care of the different linear dependencies on the beam parameters for the various PMTs considered, so this last procedure is not immune from a possible bias.

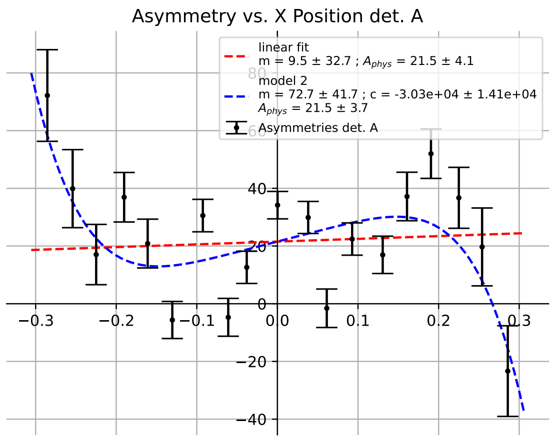

(a) *A versus δx, the linear model is the red line, the second used to fit the data is a polynomial, represented in blue.*

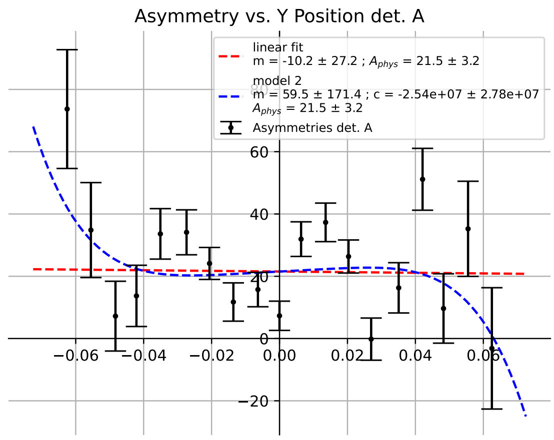

(b)

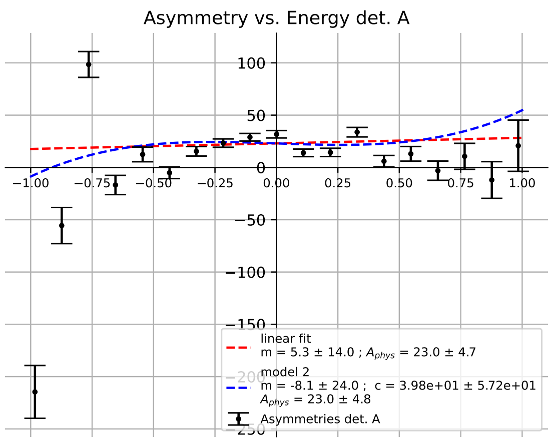

(c)

For the X and Y positions, Two models are used to fit the data. The first one is the linear model:

$$A = m\,\delta x + A_{phys} \tag{5.7}$$

For the second model, we decided to use the following polynomial:

$$A = c\,\delta x^5 + m\,\delta x + A_{phys} \tag{5.8}$$

For the energy monitor, we have:

$$A = c\,\delta E^3 + m\,\delta E + A_{phys} \tag{5.9}$$

This choice is due to the fact that we observe that A increases near the tails of the plot, the odd exponent is due to the fact that A has a different sign, positive for left and negative for right.

The values of the fit are reported in the plots. The χ^2 of the fit are reported here

detector A	X	Y	E
linear fit χ^2_{17}	99	59	94
alternative model χ^2_{16}	76	55	78

The χ^2 values are higher that the expected and we observe that the values for the model 2 are lower than the ones of linear fit. This high values can be explained with two considerations: the first one is that this procedure of averaging the data based on x interval leads to the loss of information that can influence the fit, the second consideration is that we are ignoring the possible error in the determination of δx. Despite this, we observe that using a model with more complicated dependencies doesn't change the values of A_{phys}. Because of this we don't see a strong evidence to change the linear model:

$$A_{tot} = A_{phy} \cdot P + \delta_I + A_x \delta x + A_y \delta y + A_E \delta E \tag{5.10}$$

the result of the fit are reported in 6.2, together with the final result of the asymmetry for detector A and B.

5.4 False Asymmetries

Until now the values for the false asymmetries were threated as the parameters of the fit. In this section we will investigate how we can obtain another different estimations, useful to check the validity of all the process of analysis of the data.

For $\frac{dA}{dX}$ and $\frac{dA}{dY}$, we conceptually exploit the possibility of varying the position of the beam on the target, as we did during one of the calibration phases. Using the same *wobbler 16* we asked MAMI to slowly change the beam position on the X and Y monitor. The change in position has the effect to modify the rates for the two detector, and from them it is possible to extract estimate the two false asymmetries related to the beam position. Now we will see how the two quantities are related. From the plot 5.10 we see that the counts are scaling linearly with the beam position, so we assume that the N are given by

$$N(x, ...) = N_0 + m \cdot (x - x_0)$$

it is clear that the linear model can't be always good, at some point the electron will be deflected completely out of the detector, and so the counts will fall rapidly to zero. However, the magnets used to deflect the beam are producing small variation in the position, on the order of hundredths of a millimeters. Let's suppose that the beam position for two sub-events is x_1 and x_2, we can calculate the asymmetry between the two event, taking care of the possible effects due to the different position. We write explicitly:

$$Asym = \frac{N(x_1) - N(x_2)}{N(x_1) + N(x_2)} = \frac{N_0 + m \cdot (x_1 - x_0) - N_0 - m \cdot (x_2 - x_0)}{N(x_1) + N(x_2)} = \frac{m}{2N_0 + m \cdot (x_1 + x_2) - 2mx_0}(x_1 - x_2) \tag{5.11}$$

In this equation three different parameters appear: N_0 is the offset of the linear model, m is the angular coefficient, or the slope, and x_0 is the initial position respect to we compute the position variation. The first two terms are obtained by a linear fit, while x_0 is fixed conveniently.

We can approximate the denominator deleting the term $m \cdot (x_1 + x_2)$ which should be equal, at first order, to $-2mx_0$, and should cancel out. We end with:

$$Asym = \frac{m}{2N_0}(x_1 - x_2) \tag{5.12}$$

The term in front of $(x_1 - x_2)$ can be compared to $\frac{dA}{dX}$. For N_0, the offset, we substitute the averaged value counts of each PMT for the polarized beam acquisitions (we remind that the rate are collected during each 20 ms time interval of each sub-event).

The data are reported in the table below:

PMT	Detector A	Detector B
PMT 0	63733	17609
PMT 1	67262	17514
PMT 2	59782	14055
PMT 3	51736	
PMT 4	39057	
PMT 5	39667	
PMT 6	32768	
PMT 7	23593	

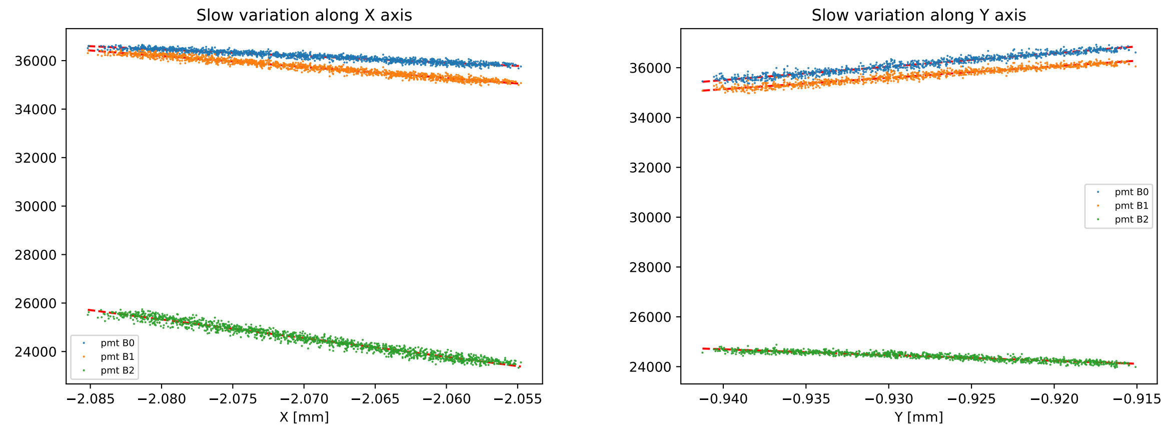

(a) *Plot for slow variation in x direction for detector B.* (b) *Plot for slow variation in x direction for detector B.*

Figure 5.10: Plot of the pmt occurrences versus the X position. The X position was slowly changed during this acquisition.

The values for the false asymmetries obtained with this method are:

'PMT'	A_x µm^{-1}	A_y µm^{-1}
B0	692	795
B1	395	682
B2	289	601
A0	233	533
A1	223	518
A2	202	493
A3	190	473
A4	211	503
A5	214	506
A6	217	510
A7	220	514

These values are not in agreement with A_x and A_y obtained from the fit (6.2). However, there is the strong suspect that the strong correlations between

5.4.1 Energy Asymmetry

For the energy asymmetry, a different method is necessary. We directly compute the Mott cross-section of the electron-carbon elastic scattering, and from that we can derive the false asymmetry due to energy variation. We start from the formula of the expected rates:

$$\frac{events}{time} = n_e N_t v_e \frac{\partial \sigma}{\partial \Omega} (\partial \Omega_a) \epsilon \tag{5.13}$$

Where:

- n_e electron density of the beam.
- N_t Number of scattering centers of the carbon target.
- v_e electron speed.
- $\partial \Omega_a$ solid angle acceptance of the spectrometers.
- ϵ detector efficiency.

We do not need to compute directly the expected rate for the two detectors, because some terms cancel out when substituted in the formula for the asymmetry, the only relevant term is the cross section:

$$A = A_n + \frac{\sigma(E_1) - \sigma(E_2)}{\sigma(E_1) + \sigma(E_2)}$$

Because $\partial\Omega_a$ is a common term in the numerator and in the denominator, we can simplify the expression and substitute σ with $\frac{\partial\sigma}{\partial\Omega}$. The Mott cross section is given by the formula below:

$$\frac{\partial\sigma}{\partial\Omega} = \frac{Z^2\alpha(\hbar c)^2}{E^2 sin^4(\frac{\theta}{2})} \cdot \frac{E'}{E} \cdot cos(\frac{\theta}{2}) \cdot F^2(\vec{q}) \tag{5.14}$$

Where the first term is the Rutherford cross-section, the second term represent the recoil of the nucleus, the third terms is the $cos(\frac{\theta}{2})$, and the last term is the nucleus form factor. The Recoil term can be written:

$$\frac{E'}{E} = \frac{1}{1 + \frac{E}{Mc^2}(1 - cos(\theta))}$$

With this final substitution we can rewrite the Mott cross section as:

$$\frac{\partial\sigma}{\partial\Omega} = \frac{D}{AE^2} \cdot \frac{1}{1 + EC} \cdot B \cdot F^2(\vec{q})$$

To compute the false asymmetry related to energy, we always assume that for small energy variation, a first order approximation is valid:

$$\sigma(E_1) \simeq \sigma(E_0) + \frac{\partial\sigma}{\partial E}(E_1 - E_0)$$

The approximations is done for small variations around the beam energy, which is 570 MeV. Now it is possible to compute the false asymmetry, the searched expression is:

$$A_E = \frac{\partial\sigma}{\partial E\partial\Omega} \cdot (2\frac{\partial\sigma}{\partial\Omega})^{-1} \tag{5.15}$$

We compute the above formula withe the constant A,B,C,D defined in 5.14.

$$A_E = -\frac{1}{2}\frac{2 + CE_0}{E_0 + E_0^2 C} \tag{5.16}$$

The result, applying the above formula is $A_e = -1.75\,\frac{ppm}{\mathrm{keV}}$. We can compare this result with the values obtained from the fit. The results are in agreement with the sign, if fact we expect a negative effect related to the beam variation. However, the false asymmetries from the fit are 1 order higher than the values computed here. A possible reason could be that we are underestimating other contributions that seems to be important with the energy variation.

Chapter 6

Result

In this chapter we report the result obtained for the data-analysis. First we report the averaged asymmetries with and without subtracting the pmt offset. The sign of the asymmetry is given by the sign of the cross product between $\vec{k}$ incident electron and $\vec{k'}$ scattered electron. So we expect to see a positive sign for detector A and negative sign for detector B. From the asymmetry results, we can compute the factor c as the ratio between the final asymmetries with and without subtracting the offset. The values can be directly confronted with the ones defined in 4.3.5. All the values are in reported in ppm.

PMT	Average	σ
B0	-19.92	7.7
B1	-19	7.8
B2	-23.42	8.7
A0	18.8	3.7
A1	16.05	3.4
A2	18.45	3.7
A3	19	4.2
A4	20.84	5
A5	22.83	4.9
A6	17.49	5.5
A7	19.24	6.6

(a) *Asimmetries, with offset not subtracted.*

PMT	Average	σ
B0	-20.61	8
B1	-19.69	8
B2	-24.13	9
A0	24.55	4.2
A1	22.54	4.1
A2	24.37	4.3
A3	23.49	4.7
A4	24.21	5.4
A5	26.39	5.3
A6	19.82	5.9
A7	20.97	6.9

(b) *Asymmetries with offsets subtracted*

PMT	c
B0	0.97
B1	0.96
B2	0.97
A0	0.77
A1	0.71
A2	0.76
A3	0.81
A4	0.86
A5	0.87
A6	0.88
A7	0.92

(c) *c factor, as defined in 4.9*

Table 6.1: Averaged asymmetries over all the events. The values are corrected subtracting $\overline{A}_I$ and considering the effective polarization p of the beam

The asymmetries are shown with the corresponding errors in the following plot. To Obtain a final asymmetry for detector A and B, the asymmetries for each plot are averaged using the formula:

$$\overline{A_n} = \sum_{i=0}^{n_{PMT}} \frac{w_i A_i}{\sum_{i=0}^{n_{PMT}} w_i} \tag{6.1}$$

This is a weighted mean, and $w_i = \frac{1}{\sigma_i^2}$. This formula must be used to take care of the different statistical error of the PMTs.

The overall results for the two detectors, without applying further cuts, are:

- Asymmetry for detector A, $A_A = 23.6 \pm 1.7$ ppm.
- Asymmetry for detector B, $A_B = -21 \pm 5$ ppm.

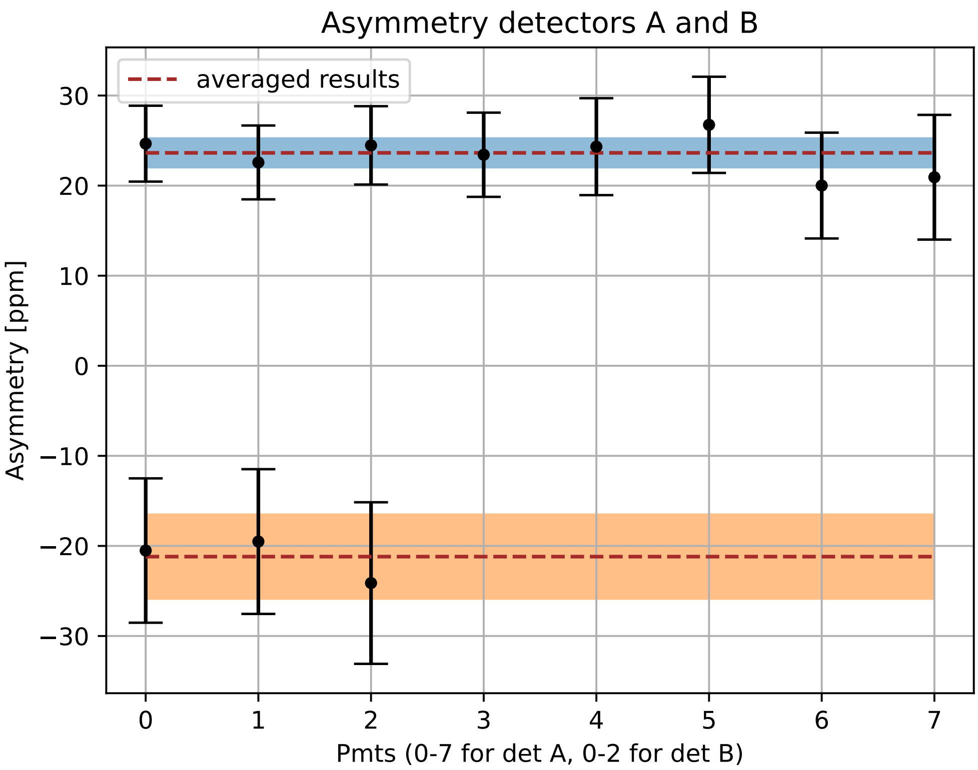

Figure 6.1: Plot of the PMTs asymmetries. The result are the average event per event, corrected by the beam asymmetry current $\overline{\delta I}$.

6.1 Data Without Polarization

For the data without polarization, we report the result obtained from the fit:

PMT	An	Ax	Ay	Ae	$\chi_{reduced}$
A0	-12 +/- 5	88 +/- 30	38 +/- 154	-25 +/- 13	1.0 +/- 0.002
A1	-9 +/- 5	44 +/- 29	57 +/- 149	-23 +/- 13	1.0 +/- 0.002
A2	-5 +/- 5	17 +/- 30	111 +/- 154	-38 +/- 13	1.0 +/- 0.002
A3	-7 +/- 6	47 +/- 32	85 +/- 163	-51 +/- 14	1.0 +/- 0.002
A4	-5 +/- 6	38 +/- 33	192 +/- 171	-46 +/- 15	1.0 +/- 0.002
A5	-4 +/- 6	67 +/- 34	177 +/- 173	-52 +/- 15	1.0 +/- 0.002
A6	-1 +/- 7	70 +/- 36	-101 +/- 186	-54 +/- 16	1.0 +/- 0.002
A7	-1 +/- 7	25 +/- 41	-494 +/- 209	-41 +/- 18	1.0 +/- 0.002
B0	-13 +/- 11	48 +/- 58	-48 +/- 294	14 +/- 26	1.0 +/- 0.002
B1	-11 +/- 11	51 +/- 58	44 +/- 295	-3 +/- 26	1.0 +/- 0.002
B2	-7 +/- 12	90 +/- 65	-166 +/- 333	-9 +/- 30	1.0 +/- 0.002

The overall values are -5 ± 2 for detector A and -8 ± 5 for detector B.

6.2 Linear Model Result

The result obtained from the linear fit of the asymmetries versus the beam parameters are reported here, together with the false asymmetry values. In this case the model is quite simple: only X, Y, E are the beam parameters:

The result for detector A:

PMT	A_n	A_x	A_y	A_e	$\chi^2_{reduced}$
A0	24 ± 4	67 ± 27	-8 ± 135	-22 ± 12	1.000 ± 0.002
A1	23 ± 4	9 ± 26	-85 ± 130	-10 ± 11	1.001 ± 0.002
A2	23 ± 4	-12 ± 27	-24 ± 134	-21 ± 12	1.000 ± 0.002
A3	23 ± 5	14 ± 29	-180 ± 142	-31 ± 12	0.999 ± 0.002
A4	25 ± 5	50 ± 31	-85 ± 151	-26 ± 13	1.000 ± 0.002
A5	27 ± 5	31 ± 31	198 ± 152	-37 ± 13	1.001 ± 0.002
A6	20 ± 5	7 ± 33	142 ± 164	-31 ± 14	1.000 ± 0.002
A7	20 ± 6	6 ± 38	78 ± 184	-14 ± 16	1.001 ± 0.002

Table 6.2: fit result with the linear model, for detector A.

the result for detector B:

PMT	An	Bx	By	Be	$\chi^2_{reduced}$
B0	-20 ± 8	-59 ± 40	-25 ± 187	-14 ± 17	1.000 ± 0.002
B1	-20 ± 8	-64 ± 40	47 ± 188	-22 ± 18	1.000 ± 0.002
B2	-24 ± 9	-65 ± 46	-170 ± 211	-61 ± 20	1.000 ± 0.002

Table 6.3: fit result with the linear model, for detector B.

The final results of the transverse asymmetryfor the two detectors, for a $Q^2 = 0{,}04\,\mathrm{GeV}^2$, computed with the weighted mean is:

DETECTOR	An
A	23.1 ± 1.7
B	-21 ± 5

Table 6.4: Overall result for detector A and B.

Chapter 7

Conclusion and Outlook

Appendices

.1 Abbreviations

.2 Transverse asymmetry

.3 Data Tree

Bibliography

[1] Single and multichannel, synchronous voltage-to-frequency converters, ad7741. *Analog Devices*.

[2] B. P. Abbott et al. GW170817: Observation of Gravitational Waves from a Binary Neutron Star Inspiral. *Phys. Rev. Lett.*, 119(16):161101, 2017.

[3] S. Abrahamyan et al. Measurement of the Neutron Radius of 208Pb Through Parity-Violation in Electron Scattering. *Phys. Rev. Lett.*, 108:112502, 2012.

[4] S. Abrahamyan et al. New Measurements of the Transverse Beam Asymmetry for Elastic Electron Scattering from Selected Nuclei. *Phys. Rev. Lett.*, 109:192501, 2012.

[5] H. A. Bethe and R. F. Bacher. Nuclear Physics A. Stationary States of Nuclei. *Rev. Mod. Phys.*, 8:82–229, 1936.

[6] Taylor Binnington and Eric Poisson. Relativistic theory of tidal Love numbers. *Phys. Rev. D*, 80:084018, 2009.

[7] M. Dehn. Strahldiagnostik und analyse der optischen eigenschaften des strahlführungssystems von mami. *Diplomarbeit*, 2004.

[8] A. Esser et al. First Measurement of the Q^2 Dependence of the Beam-Normal Single Spin Asymmetry for Elastic Scattering off Carbon. *Phys. Rev. Lett.*, 121(2):022503, 2018.

[9] F. J. Fattoyev and J. Piekarewicz. Accurate calibration of relativistic mean-field models: Correlating observables and providing meaningful theoretical uncertainties. *Physical Review C*, 84(6), dec 2011.

[10] Timothy Gay and F. Dunning. Mott electron polarimetry. *Review of Scientific Instruments*, 63:1635 – 1651, 03 1992.

[11] M. Gorchtein and C. J. Horowitz. Analyzing power in elastic scattering of electrons off a spin-0 target. *Physical Review C*, 77(4), apr 2008.

[12] Mikhail Gorchtein. Doubly virtual compton scattering and the beam normal spin asymmetry. *Physical Review C*, 73(3), mar 2006.

[13] Oleksandr Koshchii, Mikhail Gorchtein, Xavier Roca-Maza, and Hubert Spiesberger. Beam-normal single-spin asymmetry in elastic scattering of electrons from a spin-0 nucleus. *Physical Review C*, 103(6), jun 2021.

[14] J LATTIMER and M PRAKASH. Neutron star observations: Prognosis for equation of state constraints. *Physics Reports*, 442(1-6):109–165, apr 2007.

[15] J. Piekarewicz and M. Centelles. Incompressibility of neutron-rich matter. *Physical Review C*, 79(5), may 2009.

[16] B. S. Schlimme et al. Vertical Beam Polarization at MAMI. *Nucl. Instrum. Meth. A*, 850:54–60, 2017.

[17] B. G. Todd-Rutel and J. Piekarewicz. Neutron-rich nuclei and neutron stars: A new accurately calibrated interaction for the study of neutron-rich matter. *Phys. Rev. Lett.*, 95:122501, Sep 2005.